

Feature Article

# Electrospinning jets and polymer nanofibers

Darrell H. Reneker<sup>a,\*</sup>, Alexander L. Yarin<sup>b</sup>

<sup>a</sup> *Department of Polymer Science, The University of Akron, Akron, OH 44325-3909, United States*

<sup>b</sup> *Department of Mechanical and Industrial Engineering, University of Illinois at Chicago, Chicago, IL 60607-7022, United States*

Received 19 November 2007; received in revised form 4 February 2008; accepted 4 February 2008

Available online 7 February 2008

## Abstract

In electrospinning, polymer nanofibers are formed by the creation and elongation of an electrified fluid jet. The path of the jet is from a fluid surface that is often, but not necessarily constrained by an orifice, through a straight segment of a tapering cone, then through a series of successively smaller electrically driven bending coils, with each bending coil having turns of increasing radius, and finally solidifying into a continuous thin fiber. Control of the process produces fibers with nanometer scale diameters, along with various cross-sectional shapes, beads, branches and buckling coils or zigzags. Additions to the fluid being spun, such as chemical reagents, other polymers, dispersed particles, proteins, and viable cells, resulted in the inclusion of the added material along the nanofibers. Post-treatments of nanofibers, by conglutination, by vapor coating, by chemical treatment of the surfaces, and by thermal processing, broaden the usefulness of nanofibers.

© 2008 Elsevier Ltd. All rights reserved.

**Keywords:** Drop; Droplet shape; Jet; Taylor cone; Envelope cone; Beads; Buckling; Interference colors; Doppler velocimeter; Meniscus; Straight segment; Tapered segment; Electrical bending instability; Instabilities of jets; Branching; Solidification; Collection; Conglutination; Ribbons; Glints; Encapsulation; Hierarchical structures; Spider silk; Silk nanofibers; Carbon nanofibers; Ceramic; Metal; Coated nanofibers; Polymer solutions; Polymer melts; Molten polymers; Polymer fluids; Non-Newtonian fluids; Viscosity; Charge transport; Electrodes; Fuel cells; Carbon nanotubes; Protein preservation; Metal nanofibers; Structures in inter-planetary space; Exfoliated clay; Thermophotovoltaic device

## 1. Introduction

The major theme of this paper is the interaction of surface tension and electrical forces on the change of the shape of viscoelastic fluids into jets that solidify into nanofibers. Electrospinning is described from an observational point of view, emphasized by Reneker, but guided and constrained by the comprehensive and detailed theoretical insights provided by Yarin.

The electrohydrodynamical phenomena called electrospinning launched polymer nanofibers into the broader realms of nanotechnology and materials science during the decades starting in 1990 and 2000. Electrospinning has rapidly changed fiber making from a capital intensive, large scale process to a low cost, broadly applicable method that manufactures fibers on

a laboratory bench, to serve diverse needs ranging from materials science and technology to life sciences and clinical medicine. The high ratio of surface area to mass is a primary characteristic of nanofibers.

Electrospun polymer fibers span more than four orders of magnitude of diameter, with nanofibers that have cross-sections containing fewer than 10 elongated polymer molecules at one end of the range, and conventional textile fibers at the other. Polymer nanofiber technology continues to evolve rapidly as the usefulness of nanofibers becomes apparent to a growing number of scientists, engineers, and businesses. Concepts that are presently used in electrospinning are described, along with the electrified fluid jets and the fibers that are produced.

Electrospinning depends on the complex interplay of surfaces, shapes, rheology, and electrical charge. These phenomena interact in different ways to create electrified jets of polymer solutions and molten polymers. The charges are usually carried by ions, which may move through the fluid faster, commensurate with, or slower than the shape of the fluid

\* Corresponding author. Tel.: +1 330 972 6949; fax +1 330 972 5461.

E-mail address: [renerk@uakron.edu](mailto:renerk@uakron.edu) (D.H. Reneker).

changes. For a fixed quantity of fluid, the Coulomb repulsion between the charged ions favors the creation of shapes such as a jet, while the surface tension of the fluid favors sphere-like shapes with smaller surface area per unit mass. When the electrical potential of the surface is increased to a sufficiently high value, the electrical forces act in opposition to, and dominate the surface tension of the fluid. A charged jet of fluid is then ejected.

The dynamic effects of the surface tension of the fluid and of the distribution of the charge on the surface are described by similar partial differential equations. When the shape changes are relatively slow and the charge redistribution over the surface of the fluid body is relatively fast, simultaneous analytic solutions for these partial differential equations often exist. Numerical solutions may be calculated for specified boundary conditions in cases where analytic solutions are not available. The models which underlie this paper, along with references to the other theoretical papers, are presented in a comprehensive review by Reneker et al. [1]. The theoretical framework treats many features of an electrically charged, elongating fluid jet which creates a coiled path, but does not flow along the path. Paradigms for the electrospinning process, useful concepts, experimental observations, images, diagrams, graphs, models, and language are provided. This list of reviews [2–10] provides access to important contributions of many others.

The phenomena described in this paper are general. Many of the examples utilize polymeric fluids that resemble solutions of polyethylene oxide in water. Typically, molecular weights are in the range from 100,000 to several million, concentrations are from around 5% to 15%, and zero-shear viscosities are similar to that of honey, which is about  $3 \text{ N s/m}^2$ , sometimes written in Pascal seconds.

The electrical charge that is important in electrospinning is excess or uncompensated charge, usually in the form of positive or negative ions. Although all ionic solutions contain charged molecules or ions, the solution is electrically neutral because the number of positive and negative ions is exactly equal. The essential excess ions are usually created near the interface between a metallic conductor and the molecules in the solution. Electrons moving into the solution from the metal create excess negative ions in the solution. Electrons moving from the solution into the metal leave excess positive ions in the solution. Once created, the ions move by diffusive and convective processes [11] to reduce the repulsive interactions between the similarly charged excess ions and to maintain the same electrical potential everywhere on the surface of the fluid body.

Addition of a salt to the uncharged solution preserves the electrical neutrality, although the salt molecules may dissociate into positive and negative ions which move independently and thereby increase the electrical conductivity of a solution. The motion of molecular dipoles caused by application of an electric field that then remains constant, causes short-lived transient effects when the field changes. Such transient effects are not considered in this paper.

The convenience of making fibers by electrospinning many kinds of polymers, on a laboratory bench, with inexpensive machinery makes nanofibers of many polymers available for

a wide variety of possible applications. Dramatic improvements in filtration technology, based on the use of nanofibers, have occurred. Nanofibers with small diameters have a large surface area per unit mass. Many molecules, particles, and biological structures can be sequestered and protected inside nanofibers, while remaining accessible for use when needed. Nanofibers can be used as convenient packages and supports for reagents and catalysts. Novel fabrics and structures can be made.

The formation of stable cones on electrified fluid surfaces, the creation of fluid jets, the bending instability of electrified jets, branching, and capillary instabilities are described. The process of collecting fluid jets involved coils formed by electrical bending, branching, conglutinated networks of fibers, and garlands. Distinctive patterns associated with buckling as the jet was stopped on a solid surface are described. Several videographic and laser light scattering methods for observing the three-dimensional path of jets in flight, and for observing the diameter and velocity of segments were developed. Solidification of the thin jets produced nanofibers. Phase separation of both polymer blends and block copolymers was observed. Nucleation and crystallization occurred inside nanofibers. The growth of multiwall carbon nanotubes on carbon nanofibers created hierarchical structures which can lead to the design and construction of electrodes, on a much smaller scale than that heretofore possible, for fuel cells, batteries, electrochemistry, and the control of bioelectric potentials at the cellular level.

Hydrocarbon nanofibers such as polyacrylonitrile were converted to carbon nanofibers by low temperature oxidation followed by heating in an inert atmosphere. Ceramic nanofibers were made from electrospun organometallic nanofibers by heating in an oxidizing atmosphere. Metal nanofibers or nanowires were made by heating a nanofiber that contained metal atoms in a reducing atmosphere [12,13]. Core-shell nanofibers [14] and carbon nanotubes [15] were described. Nanotubes of polyparaxylylene were made by coating polymeric nanofibers which were then removed, leaving the nanotubes [16].

Section 2 describes stable, electrified drops attached to an orifice, the tapered straight segment of the jet that emanates from the electrically charged surface of the drop, and the electrically driven bending instability which generates a coiled jet path. Section 3 describes the branching and bead-forming instabilities which occur under some circumstances. Section 4 introduces measurements of the jet velocity and diameter. The origin of the moving glints which often dominate the visual image of electrospinning experiments is described. Observations of multiple jets flowing from the same drop are presented. Section 5 introduces conglutinated jet paths that cross and stick together, and shows how nanofiber garlands form. Examples of the formation of a solid skin on a jet are shown. Section 6 presents examples of crystal nucleation by nanofibers. Fibers with aligned but locally disordered chains that crystallize when annealed are described. Examples of the encapsulation of many substances in polymer nanofibers are described. In Section 7, approaches to the thinnest possible fiber (one molecule) by electrospinning are explained. Nanofibers coated with carbon, metals, and ceramics, are described. Hierarchical structures of

carbon nanofibers which support the growth of carbon nanotubes and the electrospinning of polymer melts in a vacuum or in air are reviewed. Early work on electrically conducting polyaniline molecules is presented. The electrospinning of nanofibers from both spider silk and caterpillar silk is summarized.

## 2. Jet paths

Taylor described early experiments on the effects of electrification of a flowing jet [17,18] that did not contain polymer molecules. In a prototypical electrospinning experiment, a characteristic jet path was created when a fluid polymer solution, supplied to a drop attached to an orifice by surface tension and viscoelastic stresses, was electrified by a sufficiently large electrical potential applied between the drop and a collector some distance away. The shape of the drop approached a cone and an electrically charged jet of fluid emanated from the tip of the cone. The jet followed a path that began with a straight segment. The diameter of the jet, in the straight segment, decreased monotonically with distance from the tip. Each segment of the jet retained most of its downward velocity, but surprisingly, moved radially outward at a comparable velocity as the electrical bending instability developed. Electrical forces from the charge carried with the jet caused the jet to continue to elongate as it coiled. The thin fluid jet finally solidified into a nanofiber.

Interactions of polymer molecules in the fluid and the electrical forces from excess ions carried with the jet generally prevented the onset of the capillary instability. Sometimes the capillary instability occurred, and converted the cylindrical jet to a series of droplets which solidified into beads supported on a nanofiber.

### 2.1. Stable drop anchored to an orifice

A droplet of polymeric fluid, polyethylene oxide in water, was suspended by surface tension and viscoelastic stresses at an orifice in the form of a hole, smaller than the base of the droplet, in the bowl of a small aluminum spoon [6], as shown in Fig. 1. An electrical potential difference, measured in volts, was applied between the fluid and a flat, electrically conducting plate. The distance, perpendicular to the plate, between the drop and the plate is called the gap distance. The average electric field in the absence of a jet is sometimes reported as the electrical potential difference divided by the gap distance, which is a good approximation near the collector, but the electric field within a distance commensurate with the radius of curvature of the tip of a Taylor cone before the jet appeared, was much higher as discussed below. After a jet was established, the electric field at the location of any typical segment was modified, by the electrical charge carried by all parts of the jet, in a time varying way that depended on the complicated instantaneous path of the entire jet.

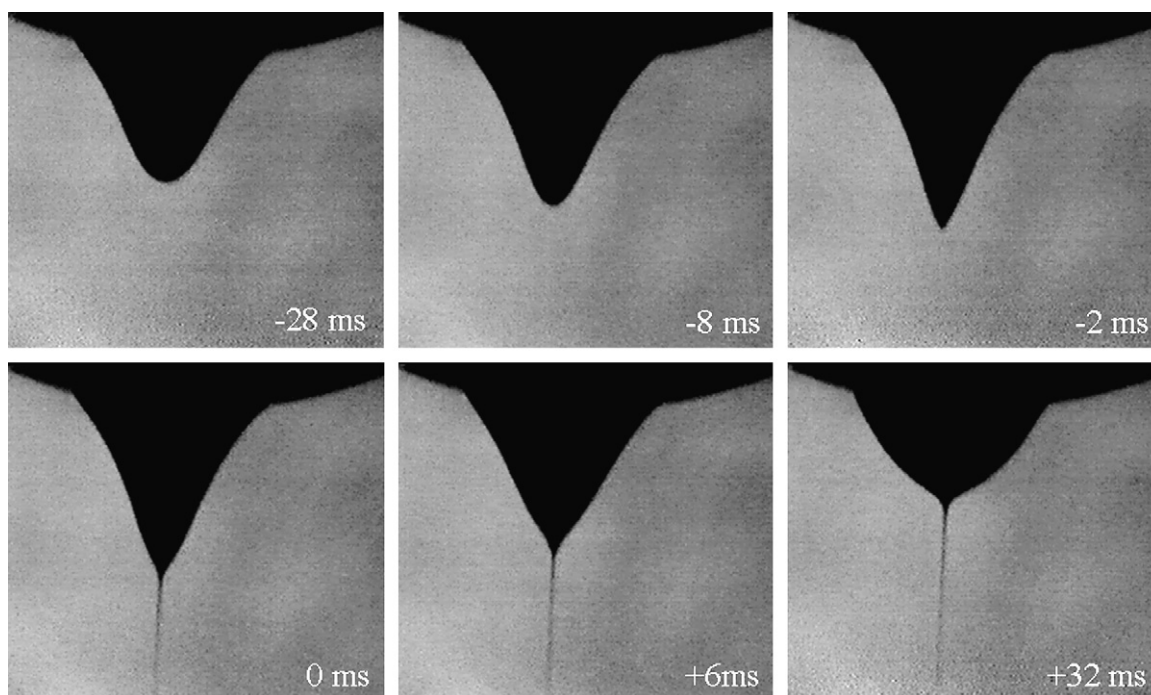


Fig. 1. The evolution of the shape of a fluid drop in selected images from a video in which a new image was recorded every 2 ms. The time zero was taken to be the frame in which the jet first appeared. The electrical potential was applied for a little more than 28 ms earlier. The droplet of polyethylene oxide solution in frame  $-28$  ms was already transformed part of the way toward a conical shape by the applied electric potential. The rounded tip became sharper and a jet emanated from the tip of the cone. Six milliseconds later, the shape of the cone was changed and after about 20 ms the droplet had a rounded shape. A rapidly elongating and thinning jet, carrying electrical charge, flowed from the droplet. This shape was stable, and persisted as long as the solution carried away by the jet was replaced by fluid flowing into the droplet through the hole in the spoon to which the droplet was attached by surface tension. In this experiment, the hydrostatic pressure in the fluid was created by the few millimeter height of the solution in the bowl of the spoon. The shape and size of the steady state droplet may change if either the hydrostatic pressure or the applied electrical potential changes. The length of the horizontal edge of each of the images is 1 mm. Reprinted with permission. [6, Fig. 6.1].

The development of a jet in a more viscoelastic fluid [19], such as molten polycaprolactone, proceeded much more slowly after the electric potential was applied, but followed patterns similar to those discussed above. When an average electric field of 100 V/mm was applied to a droplet of molten polycaprolactone, the jet began after about 90 s. The similar process in the polyethylene oxide solution occurred in less than a second. The molten drop never developed the rounded shape seen in the last panel of Fig. 1, but instead retained the elongated shape shown in the time zero panel.

The formulation that Taylor [17] used to explain the conical shape of the droplet before the jet issued has a mathematical singularity at the tip of the cone where the jet begins. The singularity was avoided by Spivak and Dzenis [20] who assumed a parabolic shape for the tip and found that the stable jet existed in the radius range less than a critical value defined by the dielectric permeability, the surface tension and the charge density of the jet. Yarin et al. [21] represented the shape as a hyperboloid, which removed the singularity and also allowed calculations to be made of the equipotential lines very close to tips with very high curvature. The hyperboloid asymptotically approached a cone. The hyperboloidal shape led to a smaller value for the half angle of the cone than Taylor's formulation produced. A computational analysis [22] of the conditions under which a droplet was pulled from a flat surface included the effects of both ohmic and convective mechanisms for redistribution of charge during shape changes. Below a critical field, the droplet acquired a steady state shape with no jet, but in fields well above the critical field a jet was initiated or the entire droplet was pulled off the surface in a very short time. This calculation also showed that the diameter of the region, near the tip, involved in the early stages of the formation of a jet, was of the order of 1  $\mu\text{m}$  in lateral extent, and therefore too small to be seen in the optical micrograph shown in Fig. 2.

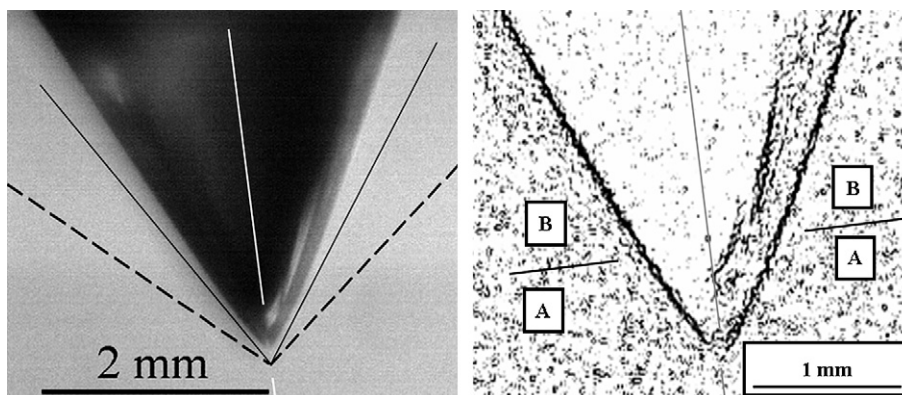


Fig. 2. An optical image of the cone on a pendant drop as the tip of the cone approached the critical shape at which a jet was ejected. Although the optical images can be approximated by a cone, it is clear that the shape is slightly rounded. The important details at the tip described in Fig. 3 are too small to be seen at all. The entire area described in Fig. 3 is only a tiny dot, lost in the noise in the optical image. The images at the right and left are the same, except that in the rightmost image an edge-finding algorithm was used to define the shape of the cone, and the magnification is somewhat larger. The radius of curvature at the tip of the cone was predicted to be smaller than 1  $\mu\text{m}$  when the jet was ejected. The observed half angle depended on the distance from the tip, since this droplet is only approximately conical. The half angle in region A was 31° and in region B was 26°. Both are smaller than the value 49.3° predicted by Taylor's [17] formulation and shown by the dashed line in this Figure. The observed half angle at the intersection of the thin solid lines is 35°. Insulators in the support structure of the orifice may become electrically charged by uncontrolled processes and cause effects such as the tilting of the symmetry axis of the cone shown in this figure. Reprinted with permission from Yarin et al. [21]. Copyright 2001. American Institute of Physics.

Calculations [21], for conditions similar to those used to create the cone shown in Fig. 2, indicated that the potential difference between the tip and the straight equipotential line at a distance  $a_0 = 2.6 \mu\text{m}$  in front of a tip with a critical radius of 0.5  $\mu\text{m}$  was only about 170 V. The calculated average electric field in that small region was much higher than the average electric field of 100 V/mm.

The initial diameter of the jet is a parameter in mathematical models but experimental measurement is difficult since the diameter may vary rapidly near the beginning, as shown in the photograph, labeled as -2 ms in Fig. 1. The diameter of the hole which feeds the droplet has little significance if the hole is large enough so that viscosity does not restrict the flow. The shape of the droplet is affected more by the location of the line where surface tension holds the droplet to the surface of the container, in this case, the outside of the bowl of the spoon.

Fig. 3 shows the hyperbolic coordinates used by Yarin et al. [21] to describe the electric field lines and the equipotential

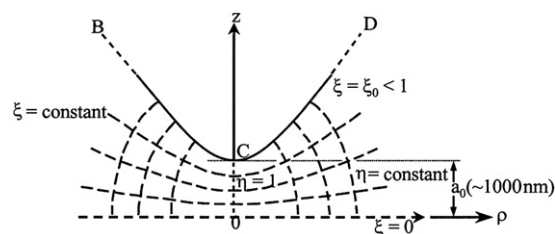


Fig. 3. Hyperbolic coordinates used to describe the electric field and equipotential lines near the tip of a fluid cone an instant before the cone became unstable and a jet issued from the tip. The dimension labeled  $a_0$ , which is 1  $\mu\text{m}$ , shows the scale of this drawing. The shape of the tip is a hyperboloid of revolution traced by the line BCD. The enhancements of the electric field that occurred on the scale of the radius of curvature of the tip of the cone are dramatically important in the transformation of the tip of the fluid cone into a flowing jet. Reprinted with permission from Yarin et al. [21]. Copyright 2001. American Institute of Physics.

lines near the tip. Note that the field of view drawn in the diagram in Fig. 3 extends only a few microns from the origin of the hyperbolic coordinate system. In Fig. 2, the fluid cone extends for several millimeters, a much greater distance than can be shown at the scale of Fig. 3.

Possible shapes for the surfaces surrounding and above the tip include an extension of the hyperboloid BCD, a plane perpendicular to the Z axis and passing through points B and D, and a cylinder coaxial with the Z axis and extending upwards from points B and D. The different shapes of these extensions, and the electrical potentials on the surfaces have a relatively weak influence on the field and potential in the tiny region that extends a few microns from the origin of the hyperbolic coordinates and includes the tip. The practical influence of such surfaces and their potentials is likely to be on the path of the jet in the region at a greater distance below the tip, for example on the coils that follow the onset of electrical bending.

In this paper most of the examples are based on experiments in which the hydrostatic pressure head (typically up to about 1000 Pa) commensurate with the pressure in the drop caused by surface tension. The pressure head changed negligibly as the fluid level in the reservoir changed during most experiments. The experiment shown in Fig. 4 is an exception. The volumetric flow rate was kept constant at selected values by a syringe pump. The average rate at which the fluid was forced into the drop by the feed system and the average rate at which the fluid was carried away by the jet must be equal in a stable system. However, the shape and size of the drop may vary with time so that the flow into the drop and the flow out of the drop are not necessarily equal at every instant. The electrical potential

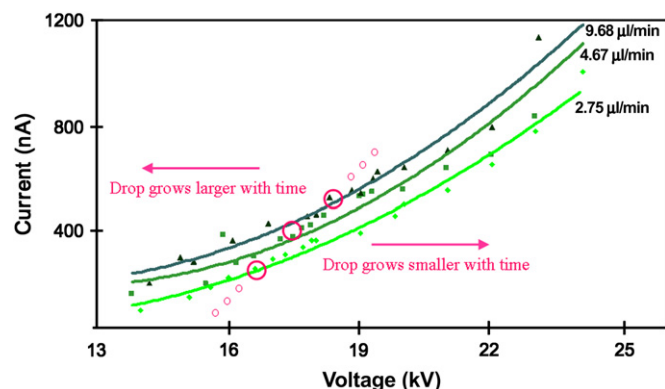


Fig. 4. Plots of the electrical current versus the applied voltage for electrically charged jets of polyethylene oxide solution flowing from a sessile drop. Solution (PEO,  $M_w = 400,000$ , 6% in water, gap distance 12.5 cm) was fed into the bottom of the drop at three different rates by an adjustable syringe pump. The volumetric flow rate, carried out of the drop by the jet, increased as the voltage increased. A voltage at which the flow out of the drop was equal to the set flow rate into the drop could be found experimentally by adjusting the voltage to make the size of the drop constant in time. These quasi-stable points are marked with a red circle on each flow rate curve, and the resulting line, with a voltage over current slope of about  $5 \text{ G}\Omega$ , is extrapolated as small red circles. The curve formed by these quasi-stable points separated the graph of current versus voltage into a region in which, with time, the drop volume grew larger and a region in which the drop grew smaller. Oscillations in drop size and flow rate out were observed for operating conditions near the line of red circles.

was changed and the electrical current was measured quickly, before the size of the drop changed much. For a constant feed rate, if the voltage was too high, the drop became smaller and the beginning of the jet often moved to the edge of the orifice before the jet finally stopped. If the voltage was a little too small, the size and the shape of the drop and the diameter of the jet tended to oscillate in time. If the voltage was much too low, the drop grew large, and changed shape as gravitational forces became important. Ultimately a sessile drop flowed over its support, and a pendent drop dripped.

The length of a short, essentially straight segment, measured along its own axis, increased in response to the Coulomb repulsion between the excess charge distributed along and carried with the segment. This increased length was accommodated by motion of the ends of the segment by nearly equal amounts, but in opposite directions, and by the radially outward motion of the entire segment. The center of mass of the segment did not move along the local direction of the path of the jet. In other words, the volume of fluid in the segment did not flow along the path, but radially outward from the path. As all the segments of the coil elongated, the perimeter and diameter of all the turns grew larger. The jet grew longer and thinner. The Coulomb forces from the applied electric field moved all the segments, independently of the direction of the segment axis, in the direction of the electric field. Stereographic videos of segments identified, for example, by small branches of the sort discussed in Section 3.1, support the above description of the trajectory of a typical segment of the jet path after the onset of the first bending instability, as does the calculated path described in Section 2.3.3.

In many familiar jets, created by the flow of water from a pipe or hose, the trajectory of the fluid is along the path of the jet, but there are also common jets in which the trajectory of a fluid element is not along the instantaneous path of the jet. An orifice, constrained to move in a circle, and discharging fluid, in a direction tangential to the circle, produces a jet in which the trajectory of fluid flow is nearly perpendicular to the circular path. The behavior of such a jet is dominated by the momentum of the fluid, while the behavior of an electrospinning jet is dominated by electrical forces. Machines, which use centrifugal force to spin molten sugar into cotton candy, provide examples of a momentum dominated jet that generally produces fibers with diameters larger than a micron. Viscoelastic jets moving rapidly in air are subject to a similar instability that is driven aerodynamically [23].

## 2.2. The tapered jet

The straight, tapered segment of the jet that issued from the droplet, seen for example in the time zero panel of Fig. 1, has been mathematically modeled from many points of view [1]. The elongation, thinning and bending into coils that the electrospinning jets underwent are described here.

The segment of the jet leaving the tip was accelerated as the Coulomb forces, acting on the charges carried with the leading segments, pulled the jet toward the collector. The velocity of a typical segment of the fluid jet was parallel to the axis of the jet, although in real jets small lateral perturbations to the

velocity were also present. For some time after leaving the drop, the leading segments of the jet pulled the following segments, that is, the Coulomb forces on the charges on the jet pulled against the surface tension and viscoelastic forces in the jet.

After the jet was established, electrical charges in the form of uncompensated ions were carried away from the orifice by the flowing jet. The radial components of the Coulomb forces caused the excess ions to move toward the surface to satisfy the condition that, in equilibrium, the electric field inside a conducting fluid must be zero. The time required for the excess charge to move to equilibrium positions on the surface is of the order of the product of the dielectric constant and the electrical resistivity of the material. This time is often called the characteristic charge relaxation time for the substance.

Characteristic times associated with hydrodynamical shape changes are of interest in electrospinning. During some of these hydrodynamical shape changes the charge can redistribute itself to minimize the Coulomb interactions. In distant parts of the jet, simplification results from the contrary assumption, which can be justified by parameter based calculations, that a charge is carried only by movement of the fluid element in which the charge is embedded. The time required for the first coil of a bending instability to form, the time required for a jet of a certain diameter to dry, and the time required for a branch to form on an electrified jet are examples of other characteristic times associated with the electrospinning process. In electrohydrodynamics, “leaky dielectric” refers to a range of parameters in which simplifying assumptions, that the fluid is either a perfect insulator or a perfect conductor, are not appropriate. A better description of the fluid system can then result from explicit consideration of the flow of charge through the fluid as the shape changes, for example, from a thick column of solution near the orifice to a rapidly elongating thin jet. In practice, free charges rapidly accumulate at the interfaces of leaky dielectrics and the electrical forces are applied there.

As the jet became very long and thin, the characteristic time required for excess charge to redistribute itself along the full length of the jet became longer. The location of excess charge, within or on the fluid, then tended to change with the elongation, bending and other deformations of the jet. Any forces from electric fields acting on the charge were communicated to the fluid immediately. It became appropriate to say that the repulsive Coulomb forces between the charges of like sign on adjacent segments of the jet worked against the axial component of the viscoelastic stress and elongated the jet in the direction of its axis.

Polymer solutions, which support the motion of free electrons as in a metallic conductor, are not commonly encountered. Polyaniline [24] provides an interesting exception in which electrons move through dry polyaniline nanofibers. The electrical conductivity of the polyaniline fibers became evident, during the collection of the dry nanofibers, from the tendency of the network of nanofibers to extend in the direction of the applied electric field rather than forming a flat non-woven mat as is typical of insulating polymers. This extension happened because the characteristic redistribution time for the electrons along the length of the electronically conducting polyaniline nanofiber was short. Electronic charge quickly accumulated

at favorably oriented ends or bends in the fibers and stretched the dry fiber network in the direction of the applied field.

### 2.3. Electrical bending instability

The very clear stop-motion pictures made by Baumgarten [25] in 1971 are images of the electrically driven bending instability of an electrospinning jet, although the meaning of the images was not understood until attention was focused [21,26,27] on the electrically driven bending instability that Taylor [18] had recognized and commented on.

High frame rate video sequences [26] of the evolution in time of the coiled path were described by Reneker et al. [26]. In the same paper, Yarin provided a theory based calculational model for these observations. This paper was followed by two others [21,27] which detailed the theoretical basis for the electrically driven bending instability and the coiled paths that were observed. This set of phenomena and theory was collected [1] and is referred to as electrical bending in what follows.

#### 2.3.1. First electrical bending instability

It is important to distinguish between the instantaneous path of the jet and the trajectory in space of a short segment of the jet. In the straight segment, the flow direction (the trajectory of a segment of the jet) was parallel to the axis of the jet, and along the instantaneous path of the jet. The bending perturbations [21,26,27] began, see Fig. 5, and then grew rapidly into a coil, under the influence of the charge carried with the jet. The bent part of the path was elongated, and reduced in diameter. After the electrical bending caused the path to coil, the trajectory of each short segment of the coil became almost perpendicular to its own axis.

The growing perturbed path of the charged jet was quickly bent into a three-dimensional coil, which was carried downstream and increased in diameter as both the elongation and the bending continued. Typically, the electrical bending coil began at a particular distance from the orifice, and the diameter of the turns of the coil grew larger and moved toward the collector. In some cases, initial bending and coiling disappeared and recurred a few times before a steady pattern of coiling was established. Similar behavior in a jet of molten polymer is described in Section 5.3. The growing bend developed into the first turn of a growing coil shown in the second panel of Fig. 5.

The continuing electrical bending generated a coil with many turns which expanded in diameter as the jet continued to elongate in response to the Coulomb repulsion of the charge. The formation of the coiled path allowed the jet to elongate by large factors (10,000 times was commonplace), in a small region of space. The elongation rate of the jet was so high that if the jet did not coil, much kinetic energy would be required to keep the leading part ahead of the following parts of the jet. By coiling, the electrical energy supplied to the jet was instead used efficiently to elongate the jet, decrease its diameter, and thereby produce more surface area per unit mass of fluid. The highest velocities were in the direction of the axis of the straight segment and were observed near the onset of the first

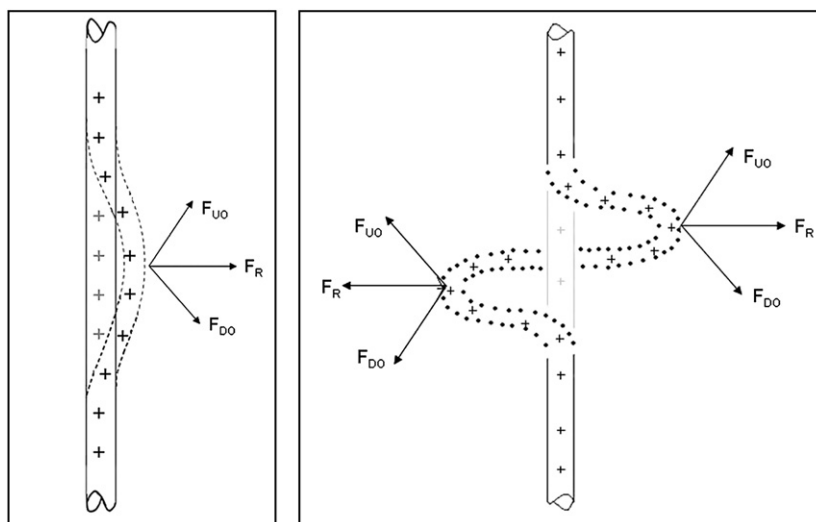


Fig. 5. A segment of an electrospinning jet at the place where a perturbed segment (shown in dotted lines) began to grow in response to the repulsive electric forces between the uniformly distributed charges carried with the jet. The charge carried by the perturbed segment was forced ( $F_{D0}$ ) downward and outward by the charges above the perturbed region, at the same time this perturbed segment was forced ( $F_{U0}$ ) upward and outward by the charge below the perturbation. The resultant of these forces  $F_R$  was in a radial direction with respect to the straight jet and grew exponentially in time as the radial displacement of the segment increased. At the same time the repulsion of adjacent charges moving with the jet caused all the bent and straight segments of the jet to continue to elongate along their local axes. The elongation increased more rapidly in the bending segment.

electrically driven instability. These velocities were typically around 1–5 m/s.

The elongation of each segment by the electrical forces caused by the charge carried with the jet continued. As the diameter of the jet decreased the path of the jet again became unstable and a new, smaller diameter electrical bending instability developed. A succession of three or more smaller diameter bending instabilities was often observed before the jet solidified. As a result, such jets acquired fractal-like configurations, and their length increased enormously as their cross-sectional diameter decreased to a fraction of a micron.

To summarize, the typical path of the jet was a straight segment followed by a coil of increasing diameter. After several turns were formed, a new electrical bending instability formed a smaller coil on a turn of the larger coil. The turns of the smaller coil transformed into an even smaller coil, and so forth until the elongation stopped, usually by solidification of the thin jet. In Fig. 6, the straight segment is shown red, the first bending coil in yellow, and the third bending coil in blue. There are three turns (which, when observed singly are sometimes referred to as loops) in the yellow coil. The perimeter of each turn of the coils associated with each bending instability grew monotonically.

After the onset of the first electrical bending instability and the development of the coiled path, the trajectory of the center of mass of a typical segment of the jet had a downward and outward component, but no component along the jet path. Motion along the downward component of the trajectory was driven by the electric field applied between the tip and the collector. Motion along the outward component of the trajectory was driven first by the lateral electric force  $F_R$  shown in Fig. 5, and then, as the bending turned the jet axis perpendicular to the external field, by the repulsion of charge carried by the segments of each coil.

### 2.3.2. Higher order bending instabilities in jets

Images of the second, third and higher bending instabilities of the jet path are shown in Fig. 7.

The diffuse cone of light near the apex of the first bending instability is the integrated intensity, from the continuous light, that scattered or reflected from the many successive loops that passed through this field of view during the exposure time. The pastel colors are interference colors that indicate that the diameters of the jet in the successive loops were in the 2–10  $\mu\text{m}$  range. Only the diffuse cone of light reflected or scattered from the jet was recorded in the frames which did not capture a flash. The other parts of the path were recorded in the frames in which the intense flash occurred. The second bending instability is shown as small coils on the fifth and sixth turns of the first bending instability. The irregular and apparently broken lines near the bottom of the image were glints from the multitude of smaller coils produced by the second and higher bending instabilities. The segments at the apex of the conical helix typically had a downward velocity of around 3 m/s. The stereographic images provided reliable information about the handedness of the coils. The coil shown was left handed, with the thumb in the direction of the flow. Right handed coils were also observed.

Jets, from this solution of polyethylene oxide, solidified into continuous nanofibers with a diameter of around 300 nm in the region near the bottom of Fig. 7. Observations of the shape of the conical envelope surrounding the coils suggested that the repulsive forces between the electrical charges on such a jet caused the loops to continue to expand, by straightening the multitude of small coils into the larger coils. The variability in the onset and behavior of the series of bending instabilities can account for a significant part of the variation in diameter that is often observed in electrospun nanofibers.

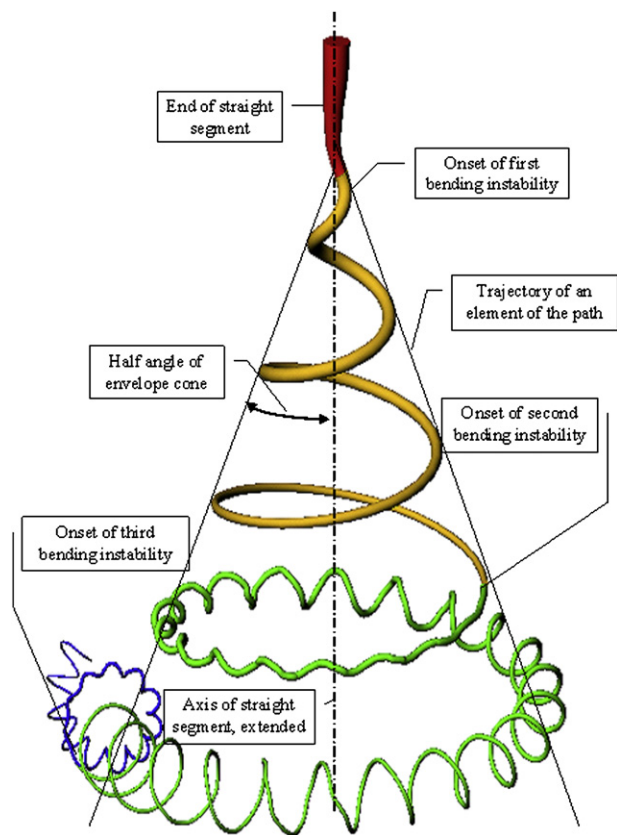


Fig. 6. A diagram that shows the prototypical instantaneous position of the path of an electrospinning jet that contained three successive electrical bending instabilities. The straight segment transformed into a three-dimensional coil. The jet path continued and transformed to a smaller three-dimensional coil, with an axis that followed the curved path extrapolated from the first coil. The second spiral eventually transformed to an even smaller spiral and so forth until the jet solidified, by evaporation of the solvent. At least four successive bending instabilities were observed in some experiments [26]. After the onset of the electrically driven bending instability in electrospinning, every segment of the resulting coil moved outward and downward in a complicated, but not random way. Reprinted with permission from Reneker and Fong [2]. Copyright 2005. American Chemical Society.

Electrospinning a solution of polyisobutylene in a mixture of acetone and paraffin oil produced a slow moving jet which allowed stop-motion images to be obtained with a digital video camera. Fig. 8 shows eight successive frames, in which the evolution of the first, second, third and higher electrical bending instabilities was observed.

The straight segment of this jet was short so that the first turn of the path is near the right margin. One turn was generated in the first four frames, and a second turn followed in the next four frames. The white spots on the jet, seen most clearly in the small turn below the tip, are glints, which occurred on segments oriented so that a light beam arriving from the direction of the upper left corner was specularly reflected into the camera.

The image of the largest smooth turn in frame 1 is projected onto the image of a vertical line in the background at a point indicated by an arrow. The change in the location of this turn can be followed by observing this intersection in the subsequent frames. The coiled path in frame 1 contains five turns. Taking

the largest smooth turn as number 1, and counting toward the beginning, the image of the 4th turn is faint in frame 1, but becomes clearer in the subsequent frames. A faint glint is present at the leftmost extremity of the 1st turn, and brighter glints are present at corresponding points on the smaller turns. In a faster moving jet, the successive positions of these glints give rise to the broad white lines seen by eye or in video images of the sort discussed in Section 4.2.

The first turn was followed through the eight frames:

- In frame 2, turn 1 expanded in diameter and remained smooth.
- In frame 3, the second bending instability began to develop on turn 1.
- In frame 4, the amplitude of the second bending instability increased.
- In frame 5, the increase in amplitude continued.
- In frame 6, the path of the second bending instability displayed the characteristic shapes seen in a perspective view of a stretched coil. Some small irregularities appeared on the following turn.
- In frame 7, the coil-like features noted in frame 6 became more apparent, by the appearance of small loops consistent with a perspective view of a coil stretched along the path of the first turn. The development of a bending instability on the path of the following turn became apparent.
- In frame 8, coil-like features of the small loops on turn 1 began to develop complicated patterns of glints, indicating that the third order bending instability had developed. The coils of the second bending instability on the 2nd turn developed to the amplitude seen, in frame 5, on the first turn. In the original images, five turns could be counted in frame 1 and seven in frame 2.

A sample of the jet was collected by inserting a glass slide into the region occupied by the white dots that are apparent in each frame. The acetone in the solvent was volatile, but the paraffin oil did not evaporate, so the collected jet was still fluid. The collected segments of the jet were continuous. In times of around a minute, the collected segments of the jet separated into droplets on the slide. The white dots in these images were predominantly glints off the small coils of higher order bending instabilities, and perhaps from beads (see Section 3.3) that formed on the jet, but were still connected by the jet.

### 2.3.3. Computational model based on fluid electrohydrodynamics

Many material parameters and process parameters have important effects on the electrospinning process. There are often known relationships between parameters which are helpful, for example the dependence of zero shear viscosity on polymer concentration may be measured or determined from established models. There are empirical relationships between process parameters which may be easy to establish. For example the current carried by the jet depends on the electrical

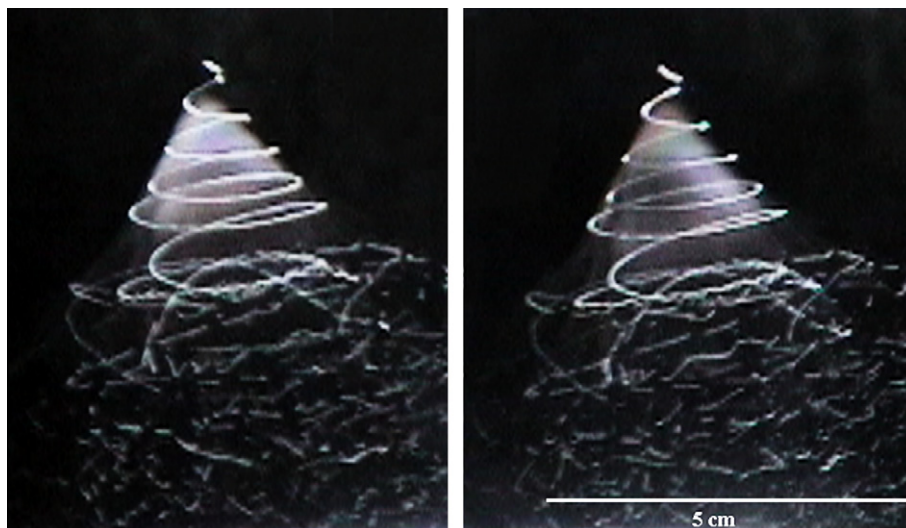


Fig. 7. Stereographic, stroboscopic picture, of a jet of polyethylene oxide, molecular weight 400,000, dissolved at a concentration of 6% in a mixture of 75% water and 25% ethanol, recorded during electrospinning. The stereographic pair of images was recorded with a digital video camera observing a single jet through a pair of prisms placed between the camera lens and the jet. The jet was illuminated simultaneously with two lights; a relatively weak continuous light and an intense strobe light that flashed periodically at a frequency around one-tenth the frame rate of the camera. The strobe was not synchronized with the camera, but often provided a short (less than 100  $\mu$ s) and intense flash of light that illuminated the path of the jet at an instant during the longer exposure, so that a stereo stopped-motion image was recorded along with the continuous light scattered from the moving jet path during an exposure time of around 16 ms. Neither light was placed in a position that showed the straight segment that extended downward to the small loop (the first turn) at the top of the coil. Reprinted with permission from Reneker and Fong [2]. Copyright 2005. American Chemical Society.

potential and the flow rate of fluid into the jet if other parameters are set, or kept within an experimentally determined range. Different choices of parameters and combinations of parameters are used in the various theoretical models that are cited in the references listed in the introduction.

Representative examples include:

- Electrical potential applied to the fluid;
- Amount of excess electrical charge carried with the fluid;
- \*Gap distance from the tip to the collector;
- \*Diameter of the flowing jet near its origin;
- \*Relaxation time;
- \*Elongational viscosity;
- \*Polymer concentration;
- Partial pressure of solvent vapor surrounding the jet;
- Flow rate of fluid into the jet.

The development of an electrohydrodynamical theory [1,21,26,27] for the electrospinning process was led by Yarin. This theory provided a basis for the development of a computational model that successfully modeled the path described in Sections 2.3.1 and 2.3.2. The list of process, material, and computational parameters contained about 25 items, including in some way, all those in the list above. This computational model was used by Thompson et al. [28] to calculate the change in the diameter of the electrospinning jet as each of 13 material and operating parameters were varied. The features of several published theoretical models were compared in that paper. Thompson et al. calculated that variation of the starred parameters in the above list produced larger effects on the diameter of the jet than did the variation of the eight other parameters tested.

Fig. 9 shows a diagram of the computational model. The jet was considered to be a series of electrically charged beads, with each bead carrying the same mass of fluid and excess charge. Each bead can be considered to represent the center of mass of a “typical segment” referred to in Section 2.3.1. This is a discrete form of the quasi-one-dimensional partial differential equations that describe the dynamics of thin electrified jets. As the distance between adjacent beads increases, the diameter of the connecting segment decreases. The lines connecting the beads are only an approximate representation of the axis of the path, which is a smooth curve that passes through the beads. The use of the word “beads” in this section refers to “computational beads” and must be distinguished from the “physical beads” described in Section 3 and used in many published descriptions of electrospun nanofibers.

The forces acting on each bead in the model are listed in Fig. 9. The first bead was pulled downward by the applied electric field. When the second bead was added, a repulsive Coulomb force appeared between the first two beads, caused them to move apart, and gave rise to a viscoelastic force represented, in the model, by a spring and a dashpot, which is a viscoelastic Maxwell element. The forces acting on a jet include the electric bending force, counteracting viscoelastic stresses, and surface tension. The surface tension forces are typically negligibly small. These three forces each involved three or more adjacent beads.

The sum of the forces accelerated each bead. When bead 2 moved away from the tip by the same short distance as was used above for bead 1, a new spring, dashpot and bead 3 were inserted near the orifice. At the same time a small perturbation was added to the lateral position of each new bead. The new position of all the beads was calculated. Then the forces acting on

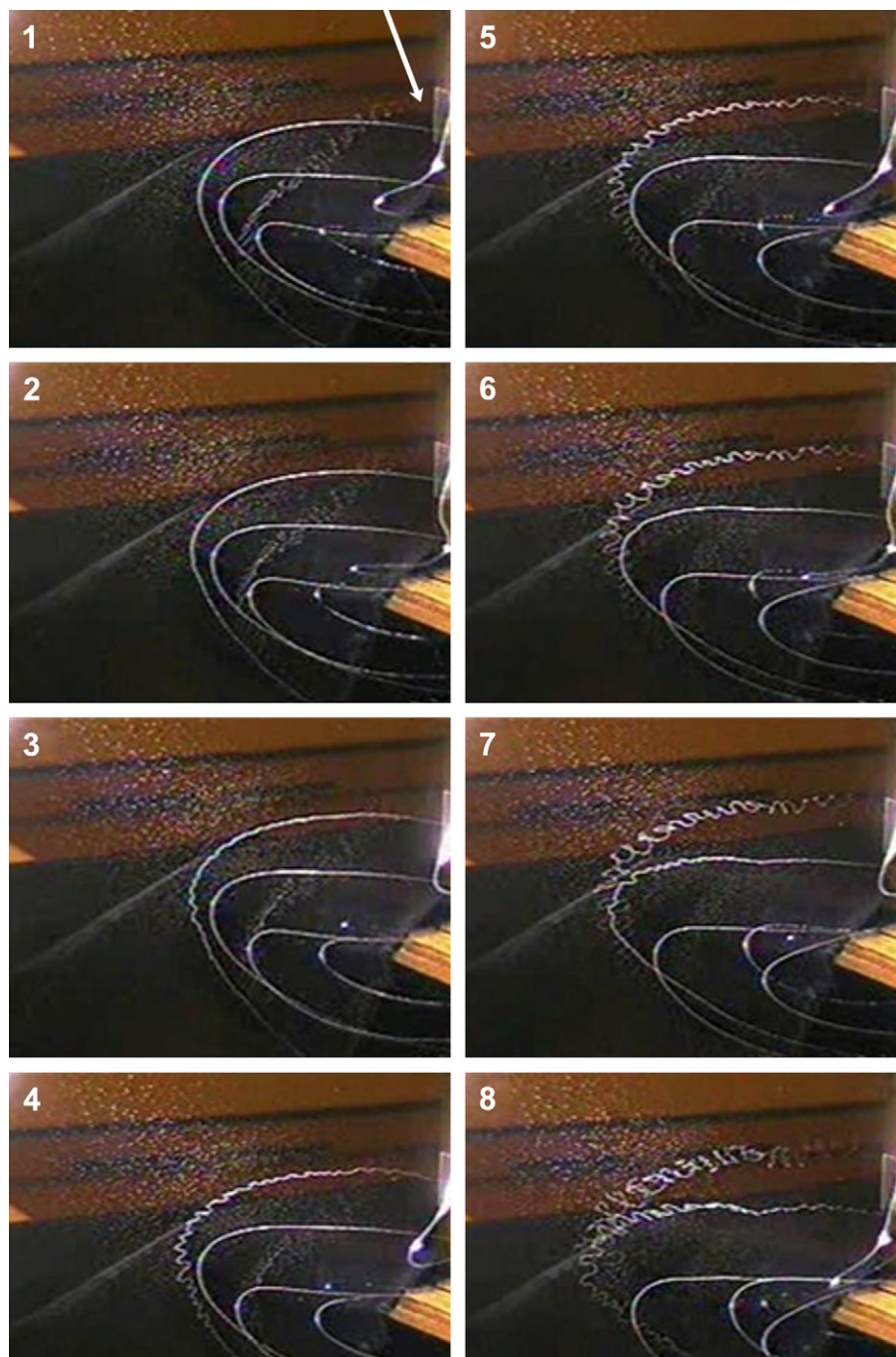


Fig. 8. A jet of polyisobutylene dissolved in a mixture of acetone and paraffin oil was observed with a digital video camera at 30 frames per second. The high viscosity of the fluid and the large diameter of the jet resulted in a slowly moving jet so that a stop-motion image was captured in each frame. The illumination was provided by an incandescent bulb about a meter away in the direction of the upper left corner. The camera looked downward and sidewise, providing an oblique view of the helical path. The largest coils spanned a distance of about 20 cm. The downward velocities of the turns of the large coils were around 0.5 m/s. The light object near the right margin and the stationary white line in the left part of the images are both part of the structure which supported the tip, and both are far below the coiled jet. Frame numbers are shown in the upper left corner of each frame.

all the beads were updated, and the new positions calculated, interactively, until a chain of many beads was created. The lateral electric component of the force on a displaced bead was the sum of the lateral components of the Coulomb forces from all the other beads in the chain. The axial components, of the Coulomb forces from the beads above and below the  $i$ th bead, almost canceled. When the radial excursion  $\delta$  of the  $i$ th bead became about the same as the diameter of the jet, the lateral

force on the  $i$ th bead began to grow exponentially with increasing  $\delta$ . The first coil of the bending instability began to develop, leading to the coil that is a characteristic feature of the path shown in Fig. 9. The calculated jet path, shown in the right panel, was compared with stop-motion stereographic images of the jet path such as shown in Fig. 7. The straight lines between the beads in the last panel of Fig. 9 suggest a polygonal path for the jet, but in fact, are only an approximation to the

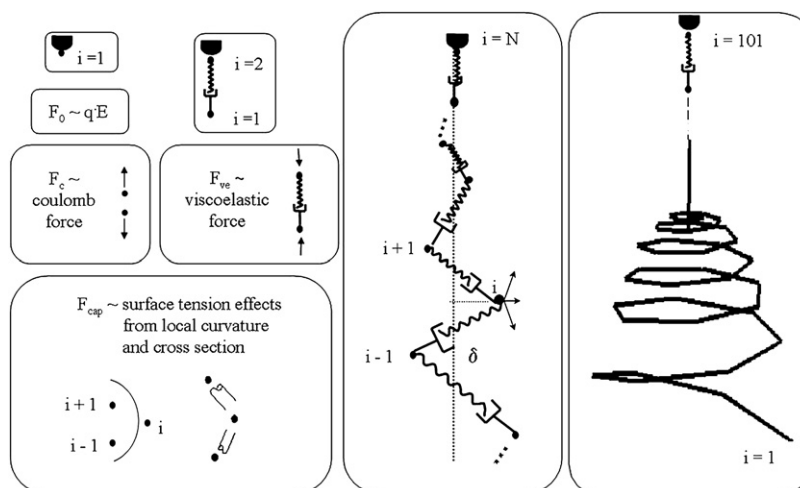


Fig. 9. The forces used in the calculation of the path of the jet, the onset of bending, and the coiled path that developed are shown. The radial distance of bead  $i$  is called  $\delta$ . The snapshot shown in the rightmost panel corresponds to 101 beads only. As time increases, values of  $N$  reached in the calculations can be of the order of 50,000.

curved path that was observed in experiments. The addition of enough computational beads to accurately represent the actual curvature quantitatively would make the calculation grow too large to be practical. For the same reason, this calculation did not show the onset of the second bending instability, even though many more beads were involved in the calculations [26,27] than are shown in the figure.

The position of two adjacent beads, at 10 successive time intervals, was calculated and is plotted in Fig. 10. The projections of the bead positions, onto the  $XY$  plane, formed essentially straight, radial lines after the onset of the electrical bending. The trajectory of each of the beads was radially outward from the axis and in the downstream direction of the straight segment of the jet. The bead positions did not “flow” along the path of the jet, which was approximately along the line connecting the beads.

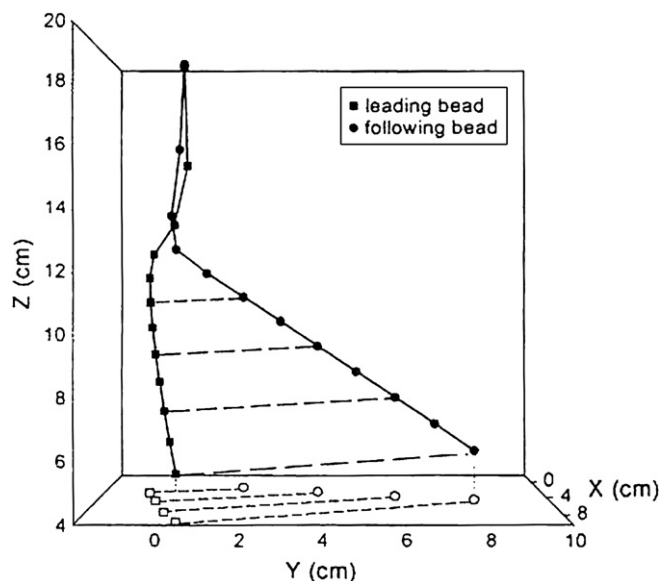


Fig. 10. The calculated [27] trajectory of an elongating segment between two adjacent beads of a loop in the first bending instability coil. The open circles and squares are the projections of the bead positions into the  $XY$  plane. Reprinted with permission from Yarin et al. [27]. Copyright 2001, American Institute of Physics.

This prediction of the theory was confirmed by observations of high frame rate stereographic videos of the positions of branches or of small loops in a garland (see Sections 3.1 and 5.2.2).

The effect of gravity and the viscosity of air on the development of the path was estimated and shown to be small. The increase in viscosity of the jet as the solvent evaporates is important. Evaporation, which caused an increase in the elongational viscosity of the fluid, was added to the model [27] to improve the prediction of the diameter of the polymer nanofiber. The decrease of the nanofiber diameter was measured as the partial pressure of the solvent in the surrounding gas increased, for the case of polyethylene oxide dissolved in water [29].

### 3. Other instabilities

In addition to the electrical bending instability described in Section 2, other characteristic instabilities were observed. Two are described in this section: branching and formation of physical beads (that are distinguished from the computational beads introduced in the previous section for calculational convenience). A third, the buckling as the jet was collected is described in Section 5.3.

If the excess charge density on the surface of the jet was high, undulations were predicted to form on the surface of a cylindrical jet. These undulations grew large enough to become unstable, and initiated branches which grew outward from the primary jet as described in Section 3.1.

The familiar capillary instability that causes a cylindrical jet of liquid to collapse into separated droplets occurred when the excess electrical charge carried by the jet was reduced. This structure solidified to form beaded nanofibers. It is not unusual for either beads or branches to occur on the coils produced by the bending instability, but it is rare for beads and branches to occur at the same time on the same segment of the jet, since beads occur when the charge per unit area is small and the branches occur when the charge per unit area is large.

Empirical observation showed that adjustment of a single process parameter sometimes produced predictable changes in

the onset of particular instabilities. When an experimental apparatus was producing a polymer nanofiber, it was often possible to adjust a single process parameter, the potential difference, and to observe changes in some feature of the jet, such as the length of the straight segment at which the electrical bending began. The conditions that must be met for a particular characteristic instability to grow are described in the framework of electrohydrodynamics. Comprehensive mathematical models all emphasize that such simple relationships depend on particular values of other parameters, and that a better description of the process results from identification of and attention to the simultaneous behavior of several process and control parameters.

### 3.1. Branching during electrospinning

A thin branch that was nearly perpendicular to the thicker primary jet was shown in Fig. 6 of an early paper [26]. The formation of branches was observed more frequently in more concentrated and more viscous solutions, and at electric fields higher than the minimum field required for producing a single jet.

Many branches [30] were observed to form where the diameter of the jet was relatively large, during the electrospinning

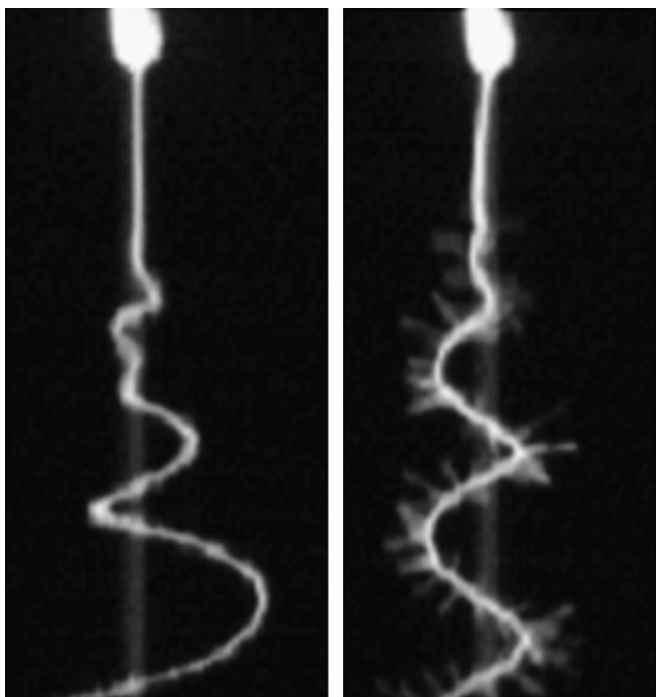


Fig. 11. Branches on the electrical bending coils of a jet of polycaprolactone dissolved in acetone. The width of each image is 6 mm. The separation between the branches, measured along the path of the jet, was around 0.5 mm. The visible branches in the left panel are less than 100  $\mu\text{m}$  long while the branches in the right panel are several times longer. The two images are separated in time by 32 ms. During the intervening time many turns of the coil passed through this field of view, so the branches in the two images occurred independently. The branches grew in a generally radial direction with respect to the axis of the segment of the primary jet to which a branch was attached, both on the straight segment and on the coils. The gray line extending from the straight segment is an artifact caused by stray light from the brightly illuminated tip. Reused with permission from Yarin et al. [30]. Copyright 2005, American Institute of Physics.

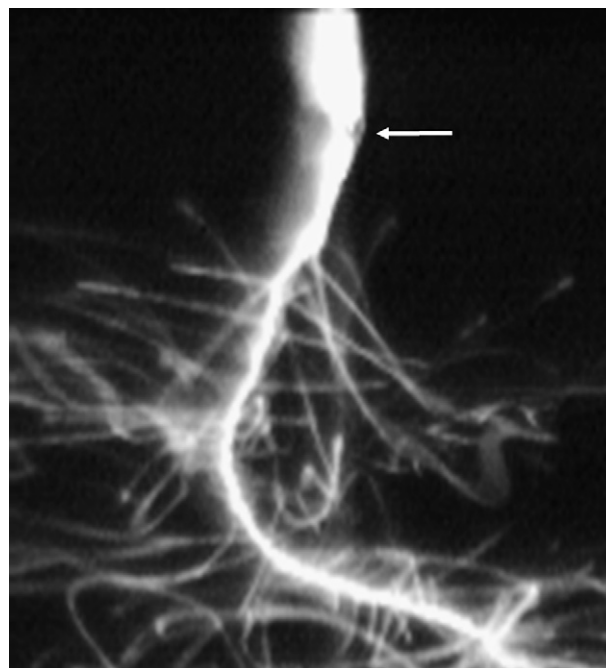


Fig. 12. A thick jet with many closely spaced branches and a high taper rate. The stop-motion image was taken at a frame rate of 2000 frames per second and an exposure time of 0.1 ms. The width of this field of view is about 12 mm. The diameter of the primary jet was about 200  $\mu\text{m}$ . The location of the orifice at the end of a glass pipette is indicated by an arrow. Reused with permission from Yarin et al. [30]. Copyright 2005, American Institute of Physics.

of solutions of polycaprolactone at a concentration of 15% in acetone, in the straight segment of the jet, or in the first coils of the electrical bending instability (see Fig. 11).

Fig. 12 shows a thick jet with many closely spaced branches and a high taper rate. Bending and branching began after only a short distance from the tip. The 15% polycaprolactone solution in acetone was electrospun at an electrical potential of 10 kV. The gap distance from pipette to the collector was 70 mm. The location of the orifice of a pipette is indicated by an arrow on the image. This image shows that the branches that grow from a jet with a large diameter can become very long and entangled.

Small branches were observed on fibers electrospun from molten polycaprolactone [19] and on small jets of polyimide electrospun in a vacuum. Branches, on small jets of polyimide electrospun from a melt in a vacuum, are discussed in Section 7.4.

Interesting branches were observed [31] on jets of poly(etherimide) in a volatile solvent which tended to form a skin on the jet as it dried. The skin collapsed into a ribbon, as described in Section 5.2.3. Fig. 13 shows that branching occurred even in jets that formed skins. A theoretical description for the formation of a skin on a jet was developed by Guenther et al. [32].

### 3.2. Undulations lead to branching

A theoretical model [30] for the evolution of an electrically charged fluid jet into a branched jet was developed. A smooth circular cylinder is the only quasi-stable shape for the surface

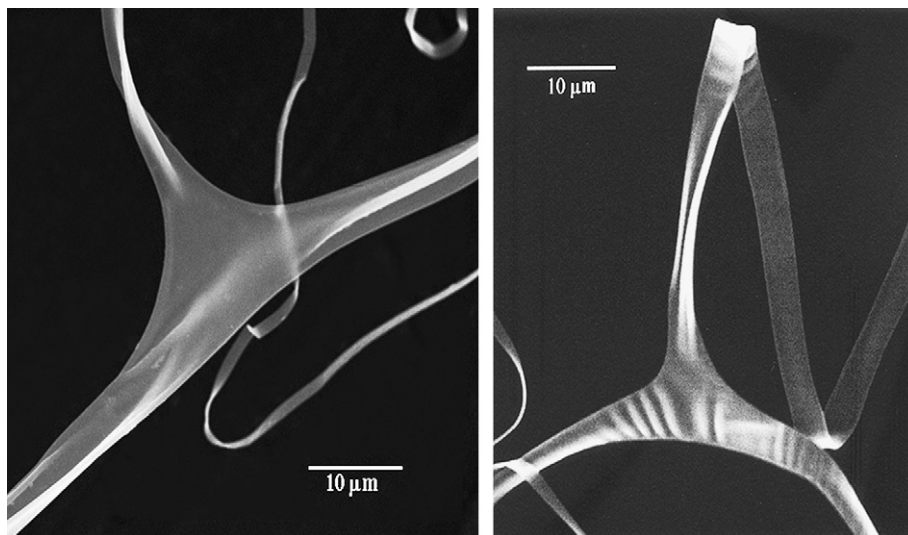


Fig. 13. Points at which a branch grew on a jet of 10% poly(etherimide) dissolved in hexafluoro-2-propanol. The primary jet, the branch, and the region where they are connected all collapsed as nearly flat ribbons or characteristically wrinkled ribbons. Reproduced with permission from Koombhongse et al. [46]. Copyright 2001. John Wiley & Sons, Inc.

of an uncharged fluid jet on time scales shorter than those corresponding to the capillary instability. As the jet is charged by increasing its electrical potential with respect to a coaxial electrode with a diameter much larger than the diameter of the jet, many quasi-stable undulating shapes may occur on the same time scales. An undulation, which moved an element of area on the surface of the jet in an outward direction, carried the electrical charge on that element to a lower potential, and thereby acquired enough energy to create the additional surface area required to form the quasi-stable undulation. The calculated undulations receded if the surface potential was decreased, much as a Taylor cone receded when the electrical potential that formed the cone was reduced.

The undulating surface of the electrified jet was described mathematically as a two-dimensional Fourier series in terms of the azimuthal angle and the distance along the axis of the jet. A trial solution in the form of a Fourier series was substituted into the partial differential equation for the shape of the jet, and the boundary conditions were used to evaluate the coefficients of the various terms in the series. The small diameter of the jet limited the number of non-zero components of the undulation. The wavelength, along the axis, of non-zero components of the undulation was also limited. This procedure led to the identification of terms of the series that were in equilibrium, quasi-static, and non-zero. The sum of these terms described the quasi-static shape of the undulated surface of the jet. An instability of the undulated surface was predicted, which should result in branching at the jet surface. Since only a subset of the Fourier components was quasi-static, there was a finite wavelength associated with the quasi-static component that had the longest wavelength along the axis. It was postulated that the Fourier component with the longest wavelength along the axis was primarily responsible for the quasi-regular spacing of the branches that was observed. The presence of shorter wavelength components with high curvature, added to the tops of the long wavelength peaks, introduced some variability in the

distribution of distances between branches and the time at which a branch appeared.

Fig. 14 shows a stereographic pair image of a straight segment of a jet with multiple branches. The position, along the jet, at which each branch was attached to a jet, was determined. The distances between the branches were compared with a theoretical model of quasi-static undulations leading to branches. That comparison, described in detail elsewhere [30] suggests that the model is useful, but the present level of agreement with experiment is not conclusive.

### 3.3. Beaded fibers

The capillary instability of a fluid jet, which causes a cylindrical fluid jet to break up into droplets, has been understood since the times of Lord Rayleigh, who recognized that the surface energy of a particular volume of fluid in the form of a cylindrical jet is higher than that of the same volume divided into droplets. The excess electrical charges carried with the jet create a strong elongational flow, and may either stabilize or destabilize the capillary instability, depending on the wavelength of the bead-forming instability [33]. The stretching of the entangled molecules in the strong elongational flow between the growing droplets produced a fluid, beads-on-string structure [27] that solidified, leaving a beaded nanofiber. The beads were often spaced at recurring distances along the fiber, and sometimes in repeating patterns of large and small beads.

Fig. 15 shows the effect of reducing the excess electrical charge on the jet by supplying counter ions [34] from a corona discharge in air. When the concentration of the neutralizing counter ions from the corona was small, the electrospun nanofibers were smooth. As the concentration of neutralizing ions increased, more of the charge on the jet was neutralized by the airborne ions. As the charge density on the surface of the jet decreased, the number of beads per unit length increased. The volume of polymer in the form of nanofibers, relative to

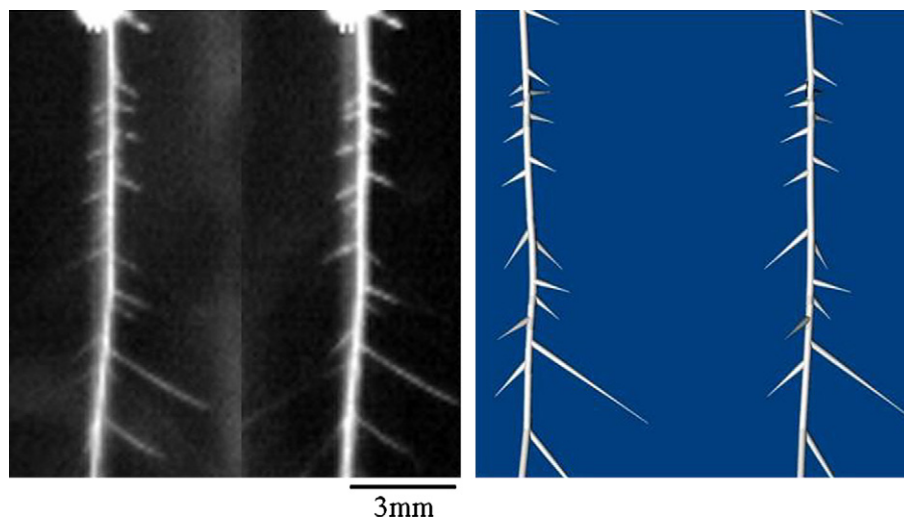


Fig. 14. Stereo view of branches that grew along the straight segment of a jet of polycaprolactone dissolved in acetone. The direction in which the branches grew was dominated by the radial electric field, but still influenced by the electric field created by the potential between the tip and the collector, which in this case, gave the direction of the branches a downward component. Growth in the radial direction was driven by the electric field from excess charge carried on the primary jet. The  $x, y$  locations of points of intersection with the primary jet and locations of tips of branches were measured on the pair of images at the left, and then used to create the simplified stereographic diagram of the branched jet, shown at the right. Reused with permission from Yarin et al. [30]. Copyright 2005, American Institute of Physics.

the volume of polymer in beads, decreased. Increasing the viscoelasticity of the electrospinning solution or increasing the concentration of dissolved salt in the polyethylene oxide solution tended to stabilize the jet against the formation of beads [34]. Beads also formed as the partial pressure of the solvent in the surrounding gas approached saturation [29].

A solution of polycaprolactone and polyethylene oxazoline in acetone produced cylindrical fibers when electrospun. The polymers solidified into two phases. The electrospinning

conditions were such that beads formed. The phase separated mixture of fluid polycaprolactone and polyethylene oxazoline was squeezed, by surface tension, into the beads. Polyethylene oxazoline is soluble in water and polycaprolactone is not, so that washing the blend fibers in water left a structure that contained only polycaprolactone. The structure of the remaining polycaprolactone phase is shown in Fig. 16. Twisted and buckled lamellae of polycaprolactone remained when the interleaved polyethylene oxazoline was washed away. The morphology of

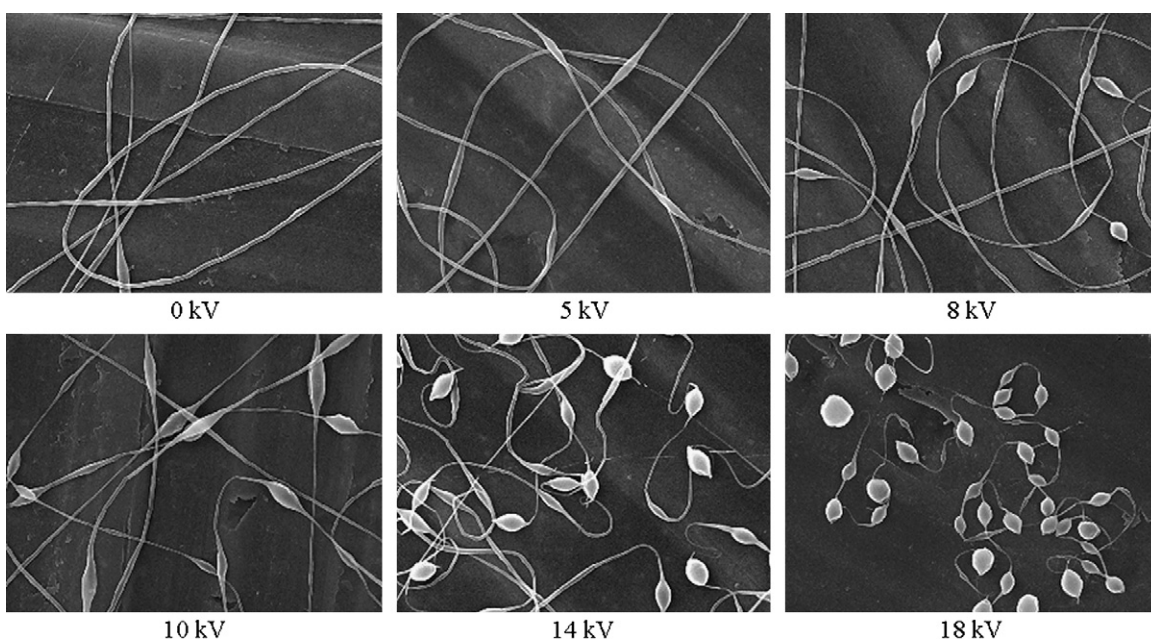


Fig. 15. Neutralization of the excess charge on the jet by airborne ions of the opposite sign leads to development of beads. The image labeled 0 kV shows smooth fibers of polyethylene oxide electrospun from a solution of 3.85% polymer in water. The electric field used for electrospinning was 40 kV/m. The horizontal edge of each of the six images is 30  $\mu\text{m}$  long. The kV values shown below each image are the potential that was applied to an array of metal needles to create ions, opposite in polarity to the charge on the jet, in a gentle stream of air that was directed toward the electrospinning jet. The relative concentration of neutralizing ions in the air increased as the kV values shown increased, but the absolute concentration is unknown. Reprinted with permission from Elsevier, Ref. [34]. Copyright 1999.

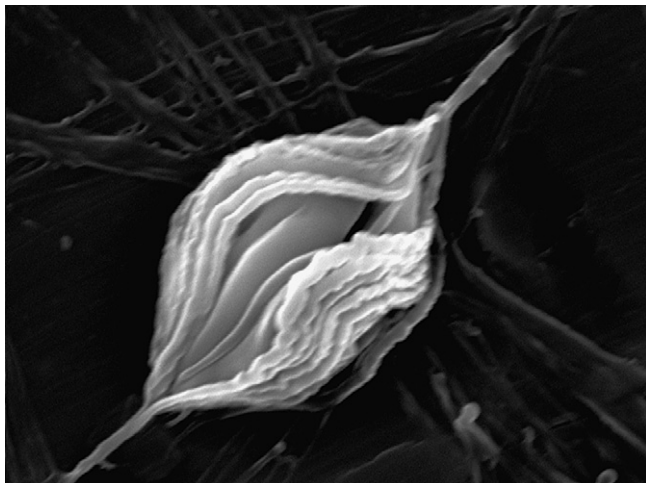


Fig. 16. The morphology of the phase separated polycaprolactone inside a bead made by electrospinning a solution of polycaprolactone and polyethylene oxazoline in acetone and then dissolving the polyethylene oxazoline with water. The width of the figure is about 3  $\mu\text{m}$ .

the polycaprolactone phase left in the bead suggested that phase separation into lamellae occurred in the jet before the fluid was extruded into the bead. The formation of a bead is the result of a surface tension driven instability which caused a cylindrical jet of polymeric fluid to divide into thinner fibers and larger beads by a nanoscale extrusion process.

#### 4. Optical measurements on a jet

The jet path is complicated, and the positions of typical segments involved in the first bending instability change at a velocity of a few meters per second. Video measurements, on a millisecond time scale, of millimeter scale motions of the jet are reported in this section. It is convenient to remember that velocities measured in millimeter per millisecond are the same as meter per second. A camera with a frame rate of 1000 frames per second can record the trajectory of every part of the jet path if proper illumination is provided. Prisms that create two images of the same area from different viewing angles provide stereographic information. Imaging times of 16–30 ms, which are commonly used in videography, record the average position of the jet much as the human eye does. It is evident in videographic images that the path of the jet, after the onset of the bending instability, exists within a region of space called the envelope cone, which is defined by the maximum excursions of the jet path from the centerline of the straight segment.

Moving glints of light are often the most striking visual feature in images of the envelope cone. Glints are incident light from one or several sources specularly reflected by the segments of the jet that are oriented so that the reflected light enters the eye or the camera. Since the orientation of the axis of a short segment of the jet path was preserved for some time, as each segment moved toward the collector, in a direction nearly perpendicular to the axis of the segment, the glints often appeared as continuous bright streaks. Images of the moving glint, observed for a known exposure time, provided information about the local direction of the axis and the magnitude of

the velocity of the segment. Since the location of the glint may move along the jet path, such a “glint derived” velocity combines effects due to translation of segments of the path of the jet with changes in the orientation of the axis of the segment.

Illumination in the form of a combination of steady light and a short flash produced images of both the relatively slowly moving glint and the instantaneous position of the moving segment from which the glint reflected. Stereographic images using this illumination method contain a wealth of information about the position and velocity of a set of segments, which can be selected by the position of the lights and the camera [35].

Interference colors, described in Section 4.3, were produced when a jet or fiber with a diameter in the range from about 1 to 10  $\mu\text{m}$  was illuminated with a beam of white light and viewed against a dark background. The spectral intensity distribution of the source and the spectral sensitivity of the eye or color camera lead to a complex, but useful relationship between a particular distinctive color and the diameter of the jet.

##### 4.1. Measuring jet velocity and jet diameter

The velocity of a particular segment of the jet was often measured from video images. The most incisive measurements, of branches or of segments that experienced the bending instability and were part of a coil, utilized stereographic video images, since the velocities of different segments varied in both magnitude and direction. Stereographic video images of a feature, such as an embedded particle or a branch that was carried with a particular segment of the jet, and identified in both images of a stereographic pair, provided the information needed to measure the direction and magnitude of the velocity.

In the straight segment, a solid particle, a few microns in diameter, dispersed in the polymer solution, and carried in the straight segment jet, was photographed with a high frame rate video camera. Fig. 17 shows the position of such a particle in 10 successive images separated in time by 0.5 ms. The successive positions of the particle are all plotted on the otherwise unchanging 10th image. The distance, in millimeters, that the particle moved in the interval between each of the successive frames is shown beside the image. The increasing separation between the particle positions in this composite image shows the acceleration of the segment of the elongating jet in which the particle was embedded. Velocities in the range from 0.5 to 5 m/s were measured. The velocity at a given position was lower when the voltage at the tip was increased.

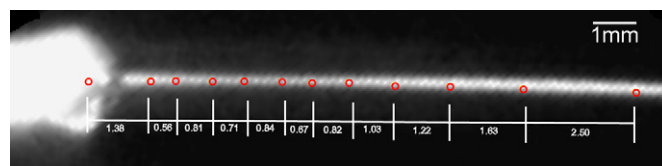


Fig. 17. The velocity of a jet of a solution of 6% polyethylene oxide in water was measured, by observing the successive positions of a particle carried inside the jet, with a 2000 frames per second video camera. The distances, in millimeters, between the observed positions of the particle are shown beside the image of the jet.

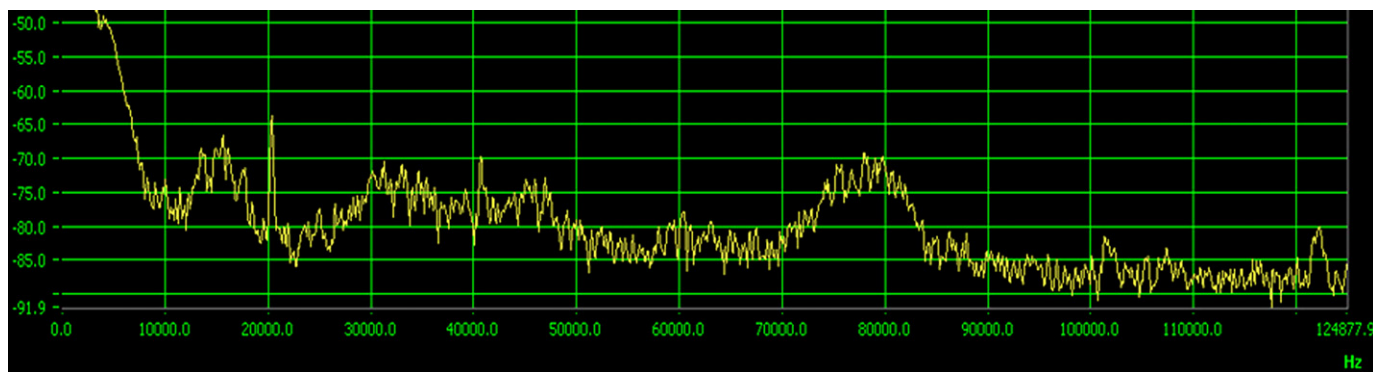


Fig. 18. The Fourier transform of the time varying intensity of light scattered from the straight segment of the jet flowing through the intersection of the coherent laser beams. The frequency at which the rightmost peak occurs ( $\sim 78,000$  Hz) is a measure of the velocity at which the jet is flowing through the region in which laser beams intersect. The frequencies of the other peaks shown in Fig. 19 are ascribed to phenomena occurring in the laser, since their position does not change when the jet velocity is changed.

A laser Doppler velocimeter measures the component of the velocity of a segment of the jet in a direction that is perpendicular to the bisectrix of the angle between two coherent beams from a laser and lying in the plane of the intersecting beams. Velocity components in other directions can, in principle, be measured with the velocimeter by reorienting the plane of the intersecting beams in relation to the jet path. The component of the velocity along the direction of the straight segment of a representative jet ranged from a few tenths to about 5 m/s, under the usual conditions of electrospinning. The length, in the axial direction, of the segment in the intersecting region of the laser beams at any instant, was in the range of 5–50  $\mu\text{m}$ .

Fig. 18 shows the Fourier transform of the time varying intensity of light scattered from the straight segment of a jet of polyethylene oxide in water, as the jet flowed through the interference pattern created at the intersection of the coherent laser beams. The peak observed at a frequency of 78,000 Hz indicated that the velocity was 0.62 m/s. The numerical relationship between the frequency of the Doppler peak and the velocity of the jet is set by the angle between the intersecting laser beams.

The volumetric flow rate is an important parameter that affects downstream phenomena, and is often a boundary condition or parameter in the theoretical description of a jet. An adjustable pressure was applied to the fluid to control the pressure at the orifice, and the flow rate was allowed to adjust to the electrospinning conditions in most of the experiments described in this paper. Multiplying the velocity and the cross-sectional area together, at the same place along the jet, provided an instantaneous value for the volumetric flow rate.

The measurement of the diameter of an electrospinning jet by diffraction of a beam of light from a laser was pioneered by Doshi et al. [36,37]. Each of the Doppler shifted laser beams in the velocimeter was also diffracted as it passed the jet, and the two diffraction patterns shown in Fig. 19 were observed.

The location of the central spots and the scattering along the horizontal direction of each beam are shown in Fig. 19. Measurements, on the single slit diffraction pattern, of the positions of the first and second intensity maxima and the

intensity minima between them were used to calculate the diameter of the jet at exactly the same region at which the velocity was measured. If the jet was moved laterally, by a measured distance, from the intersection point of the beams, but kept in the plane defined by the beams, differences in the two diffraction patterns shown in Fig. 19 contained information about the taper rate of the jet diameter.

The shape of a jet near the orifice and its velocity were measured [38] as a function of distance from the orifice and are shown in Fig. 20. The volumetric flow rate shown at the top of Fig. 20 was calculated from the measured diameter and the measured velocity at five points in the range from 1 to 2.5 mm. The

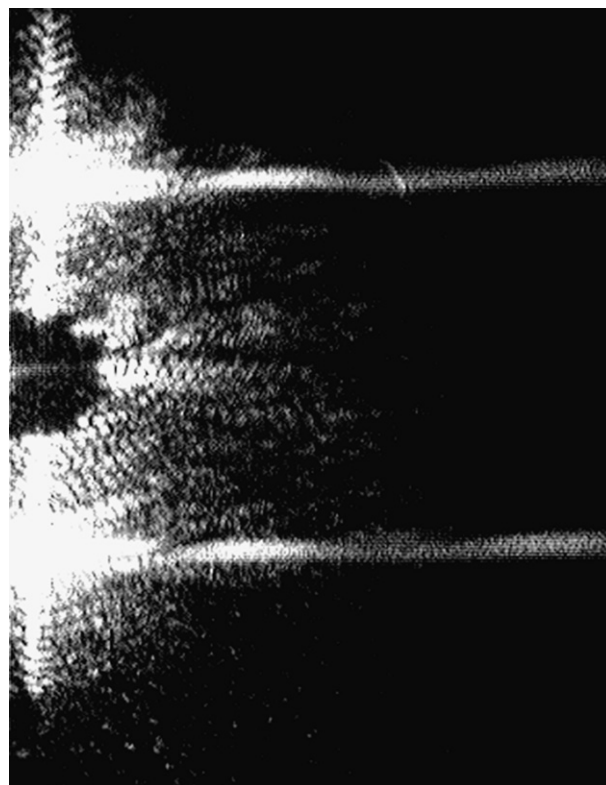


Fig. 19. The right half of the two diffraction patterns created by the two beams of the velocimeter.

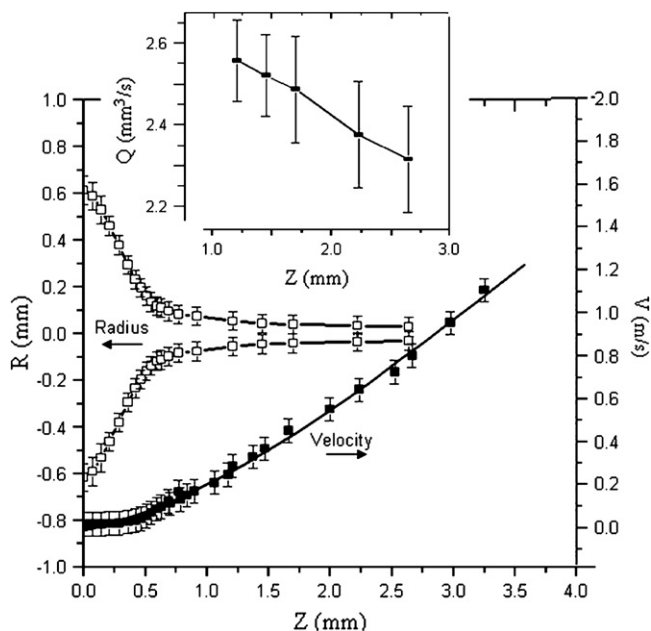


Fig. 20. The radius of a jet,  $R$ , the velocity of the fluid,  $V$ , and (inset) the volumetric flow rate,  $Q$ , as a function of distance,  $Z$ , from the orifice. The jet radius was plotted with open squares. For  $Z$  less than 0.75 mm, the radius was measured from an image. A jet of polyethylene oxide dissolved in water was used.

volumetric flow rate decreased by about 6.4% per millimeter in this range, due to loss of solvent by evaporation.

The volumetric flow rate, averaged over a longer time, was also determined by observing the decrease in the volume of fluid in the supply reservoir. The flow rate was also checked by weighing the dry nanofibers collected in a known time interval from a solution of known concentration. In many reported experiments the flow rate was set and the diameter and shape of the jet could change, as discussed in Section 2.1 near Fig. 4.

#### 4.2. Glint traces

Broad, curved, bifurcating lines, called glint traces, that sometimes showed interference colors (See Section 4.3) were often seen inside the envelope cone of an electrospinning jet. Fig. 21, one frame from a video camera, shows traces of moving glints of light, reflected into the camera from properly oriented segments of the moving coils of the jet paths. Visual and video images of the jet paths of the sort shown clearly in Fig. 7 and diagrammed in Fig. 6 were dominated by glint traces, but important aspects of the complicated relationships between the coiled jet path and the glints remain to be established. The traces of glints were sometimes taken as evidence for various kinds of jet paths which are now known to be uncommon, if they occur at all. For example, the bifurcations of the glint traces at the level of the arrow in Fig. 21 are not evidence for the bifurcation of a jet, but usually were seen when the path of a large bending coil became unstable and was transformed by the development of a smaller, higher order bending coil. A circular ring, approximating one turn of a bending coil, and

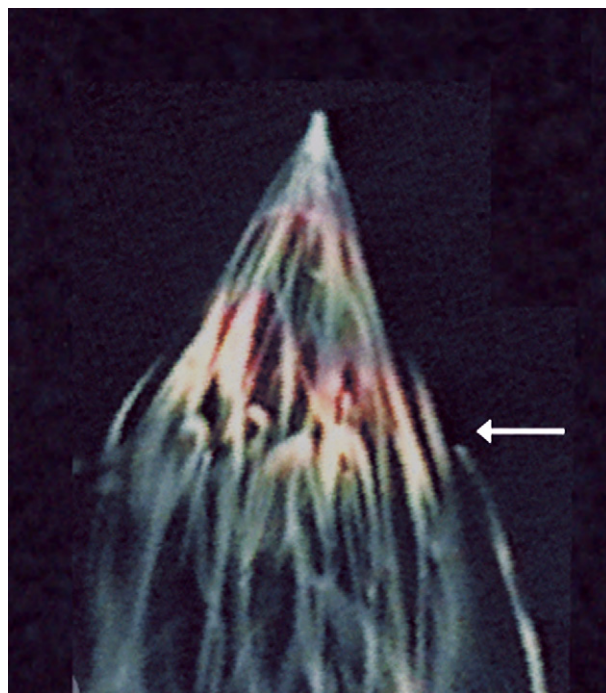


Fig. 21. Colored glints from an electrospinning jet illuminated with a beam of light from a single incandescent light at a distance from the jet of one or two meters. The width of the field of view is about 3 cm. The bifurcating lines at the level of the white arrow are due to the change of the direction of segments of the jet upon the occurrence of the second bending instability. Below this level, the coils produced by the second bending instability are present and many turns of the new coils create their own glints.

oriented like the spiraling turns of the first bending coil, showed two glints from each light source, and this was also true for the spiraling turns of the first bending coil.

The jet in Fig. 21 was viewed in a direction about  $15^\circ$  off the direction of the light so that only light reflected or scattered from the jet entered the camera, which was pointed at and focused on the jet. The exposure time was 16 ms. The straight segment of the jet, which extended for about 1 cm above the top of the envelope cone, was not visible because it was not illuminated. The first bending coils begin at the tip of the envelope cone. The interference colors indicate that the diameter of the jet in the first bending instability region ranged from around 10 to about  $1 \mu\text{m}$ . The glint traces were continuous throughout the region of the first bending coil. At the onset of the second bending coils, the number of glint traces increased because each of the new, second bending coils created additional glints. The light blue color of the lower parts of the traces indicated that the diameter of the jet there was commensurate with the wavelength of blue light.

Fig. 22 shows the motion of the glints during an exposure time of 1 ms. Both the motion of the jet path and the orientation of the reflecting segment contributed to the appearance and motion of a glint. The turns of the second bending instability in this jet were close together. The curved centerline of the many turns of the second bending coil followed the path that would have been taken by the last turn of the first bending coil if the second bending instability did not occur. The

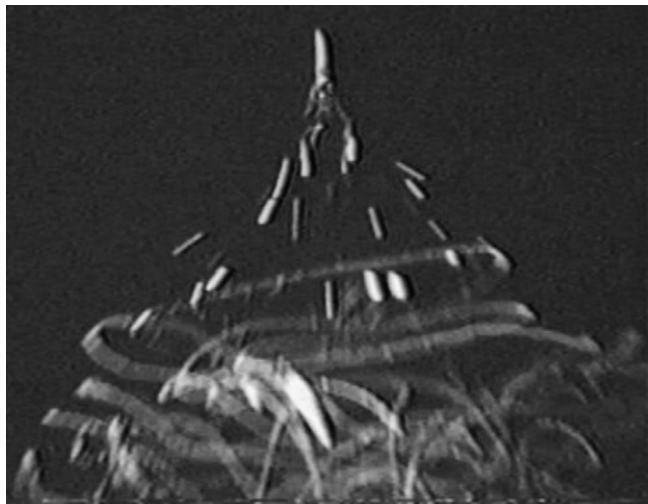


Fig. 22. This 1-ms exposure of a jet similar to the jet shown in Fig. 21 shows short segments of the downward motion of glints from the turns of the first bending coil followed by segments of the downward motion of the many smaller turns of the second bending instability coil. Two illumination sources, to the right and left, behind the jet usually produced up to four glints on each turn. The width of the field of view is about 2 cm.

downward motion of the closely spaced glints of the second bending coil created the ribbon-like features in the lower part of the image.

Fig. 23 shows a jet that was illuminated with one steady light beam, which came from the left and behind the jet. The first bending instability occurred at the end of a short straight segment, and the two glint traces on each of the turns of the first bending coil were superimposed, by proper choice of the viewing direction, to create the inverted “V” shape. The glint traces in the lower part of Fig. 23 all began at the level at which a new bending instability began.

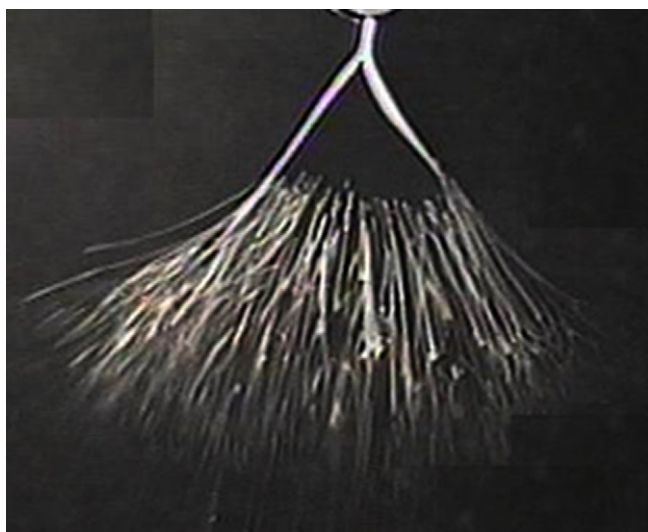


Fig. 23. A longer exposure, around 16 ms, of a jet similar to that shown in Fig. 22. The glint traces have the same origin as the traces shown in Fig. 22, but are longer because of the increased exposure time of the camera. In this figure, a single illumination source, to the left and behind, produced two glints on each of the turns of the first bending instability coil. The width of the field of view is about 5 cm. Pale interference colors were present in this image.

The jet shown stereographically in Fig. 7 is similar to the jets shown in this section. Fig. 7 is illuminated with an intense short flash that occurred during the exposure, thereby superimposing a long record of the glint traces and an image of one instantaneous jet path. Essentially the entire length of the coiled path was recorded stereographically during the intense flash. The images of many glints from the many turns that passed through the region near the apex of the envelope cone during the exposure time generated the diffuse cone of light shown in Fig. 7.

Although the interpretation of glint traces was not complete, the images and visual observations provided information about the jet that was useful for the control of the electrospinning process.

#### 4.3. Optical observation of diameter dependent colors along the jet path

If the direction, in a plane perpendicular to the axis of a segment of the jet, of the light incident on the jet was about  $10^\circ$  from the direction of the line between the jet and the camera lens, and if the background was sufficiently dark, interference colors were observed. The entire straight segment of a jet and many shorter segments of the electrical bending coils can produce interference colors.

The colors observed in a jet illuminated with white light were similar to those observed [39] in films that form soap bubbles. These colors provide a way to observe changes in the diameter of a jet during actual electrospinning, using only proper white light illumination and a human eye or camera placed at a fixed location. The colors in soap films are known to be caused by subtraction of light of certain wavelengths that depend upon the thickness of the film, from the incident white light, causing the transmitted light to show a range of pastel colors that include some distinctive pink, green, yellow and blue colors, for the incandescent or arc light sources used in our laboratories. The wavelength of the light subtracted by the fibers and not transmitted to the eye or the camera is related to the diameter of the jets. The colors were most easily observed for fibers with diameters ranging from about 0.5 to 15  $\mu\text{m}$ . As the diameter and taper of a straight segment was changed by changing the electrical potential at the tip, the characteristic colors moved along the jet, in both the straight and coiled segments.

The actual diameter of the jet associated with a particular color is best determined separately, since the eye is not a readily quantifiable spectrometer and light sources with widely different spectral intensity distributions may be used. A beam of monochromatic laser light directed onto a segment of a jet that showed a characteristic color band produced a single slit diffraction pattern on a suitably positioned screen. As discussed in Section 4.1, the separation of the spots in such a diffraction pattern was directly related to the diameter of the jet and provided a measure of the diameter associated with each characteristic color. The jet diameter that was associated with each distinctive color was determined in this way. The brighter characteristic colors were seen, independently of the exact position of the jet in a converging cone of white light, since each turn of a coil is likely to

have at least one segment oriented and illuminated in the proper way. The location of a particular yellow, pink, or other characteristic color revealed the position in space at which the diameter of the fluid jet was equal to the diameter associated with the particular color. A bright blue color, usually so relatively intense that a video camera with automatic exposure control presented it as a white spot, was associated with a jet diameter that was near the wavelength of blue light, about 400 nm. As the jet diameter became smaller, the characteristic colors were no longer produced, and the white jet became fainter as its diameter decreased.

These interference colors are very useful as a tool, for monitoring the performance of a jet, requiring only a beam of white light, a dark background and human eyes. Xu [1,40,41] provided a firm basis for the use of interference colors to characterize the diameter of a jet. Some interesting examples are provided in the following.

Fig. 24 shows the characteristic colors observed in the tapered straight segment of a jet of polyethylene oxide dissolved in water. The illuminating light was produced by a xenon arc lamp and the image was recorded with a digital video camera. A laser beam was moved along the jet to a segment with a distinctive color to create a single slit diffraction pattern from which the diameter of the jet associated with that color was determined. In the following series of pictures, the same colors are shown in jets following different paths.

#### 4.3.1. Multiple jets from a single drop

More than one jet can flow from a drop at the same time. Two jets are shown in Fig. 25. The flow divided almost

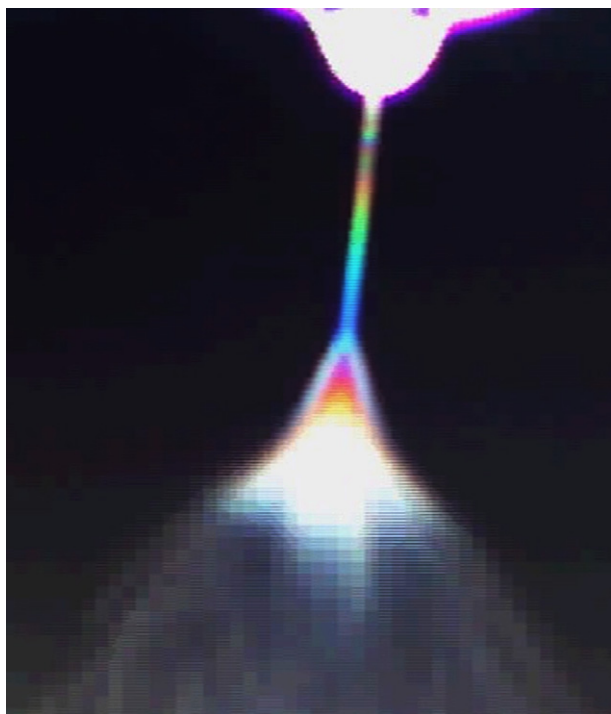


Fig. 24. Interference colors in the straight segment of a jet illuminated with white light. The image is slightly defocused to spread the intensity in the focused image of the jet over several pixels in the camera, and thereby avoid over-exposure which produces a white image in many contemporary video cameras because of the software controlled exposures used.

equally. Small variations in the vertical positions of a distinctive color band with time revealed that a particular color band in one jet moved downward at the same time as the same color band in the other jet moved upward, which tended to keep the total flow rate constant.

The effects of increasing voltage on the taper and diameter of jets are shown in Fig. 25. As the voltage increased, in two steps of about 5% of the initial voltage, the blue band moved downward, as did all the other color bands, indicating that the diameter of both jets, measured where they left the droplet, increased. The increased width of each band, clearly evident for the blue band, and the simultaneous increase in the separation of the different colors indicate that the taper rate of the jet became smaller as the voltage increased. The white region, where the diameter is commensurate with the wavelength of blue light, moved from the straight segment into the envelope cone defined by the electrical bending coils. The length of the straight segment, which is the distance from the droplet to the point at which the electrically driven bending instability began, increased. The increase or decrease in the length of the straight segment often provided a clear and visible indication of changes in the applied voltage.

The evolution in time of three jets flowing from a single drop of polyethylene oxide solution is shown in Fig. 26. This process shown was initiated by a small decrease in voltage. Fig. 26 contains selected frames from a video sequence that was several seconds long. The interference colors show that the three jets were initially similar in size. In the first 34 ms after the observations began, the leftmost jet grew larger. The color bands of the middle and rightmost jets moved upwards as these jets became smaller. Both became blue over most of their length as their diameters became commensurate with the wavelength of blue light. Within a few milliseconds more, both these jets vanished. The color bands in the jet at the left moved downward and became longer, while the taper rate decreased and the jet diameter at a given level increased.

Multiple jets from one drop were stabilized for arbitrarily long times by introducing azimuthal asymmetry in the radial component of the electric field, by asymmetric placement of one or more charged electrodes. An example with four jets originating from the same droplet is shown in Fig. 27. The straight segments of the jets, all of which had about the same diameter, appeared with different intensities because some segments had directions that did not reflect much light from the flash into the digital video camera used. The straight segments and their associated electrical bending coils were pushed apart by the Coulomb repulsion of the electrical charge carried by the jets, much as the separation of the leaves occurs in gold leaf electrometers described in many elementary physics books. The coils did not interpenetrate, although their images overlapped.

Notice that the relationships between the glints and the paths of the jets depended on the position and the angle of the straight segment of the jet path. Rows of glints, seen most clearly on the coiled path of the third jet from the left in Fig. 27, marked the trajectory that an element of the jet in the first coil traveled to reach, successively, the positions of the glints in the lower coils.

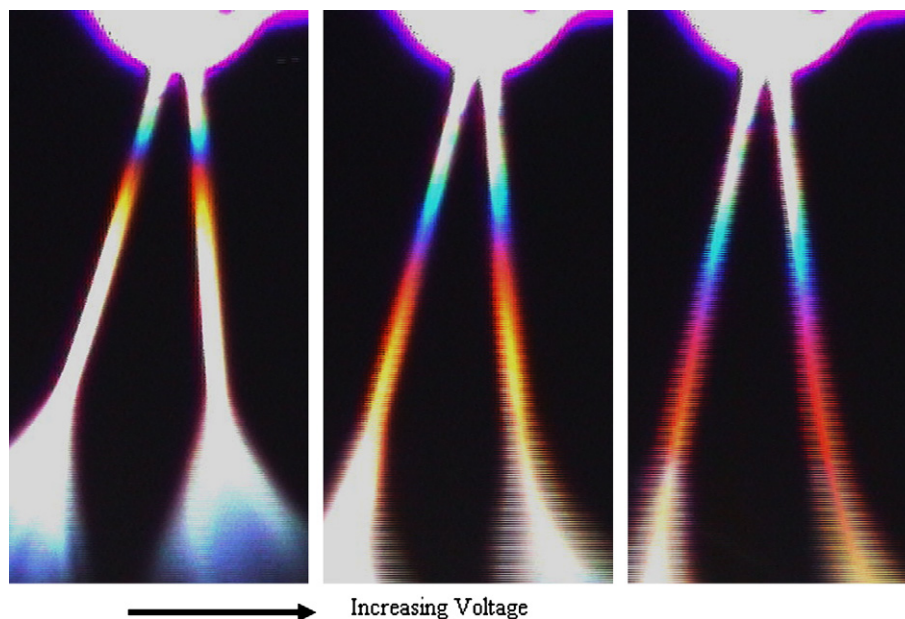


Fig. 25. The interference colors of two stable and nearly identical jets from one droplet moved downward at the same rate when the potential difference between the drop and the collector was increased by a small amount. Reprinted with permission from Reneker and H. Fong [2]. Horizontal striations are artifacts of the image reproduction process. Copyright 2005. American Chemical Society.

The interference colors on the glints from the electrical bending coils indicated that the jet diameter in this region was in the 2–10  $\mu\text{m}$  range. The colors are most clearly evident in the first five turns of the coil generated by the leftmost jet in Fig. 27. Fig. 28 is an enlargement of this region, with the intensity and contrast of the image adjusted to emphasize these colors. The light streaks near these glints indicate the sidewise direction of motion of the segment. With bright and steady illumination, and a longer exposure time, the motion of these glints would have created one of the streaks shown in Fig. 21.

## 5. Collection of the nanofibers

Evidence for tapering, electrical bending, coiling, for “pulling out” of coils into a straighter fiber, and buckling of soft jets as they are stopped on a solid collector may be deduced from jets collected at different points along their paths. Solidified coils of various fiber diameter and coil diameter are commonly observed.

If a larger loop of the sort shown in Fig. 7, which may include small loops created by successive bending instabilities,

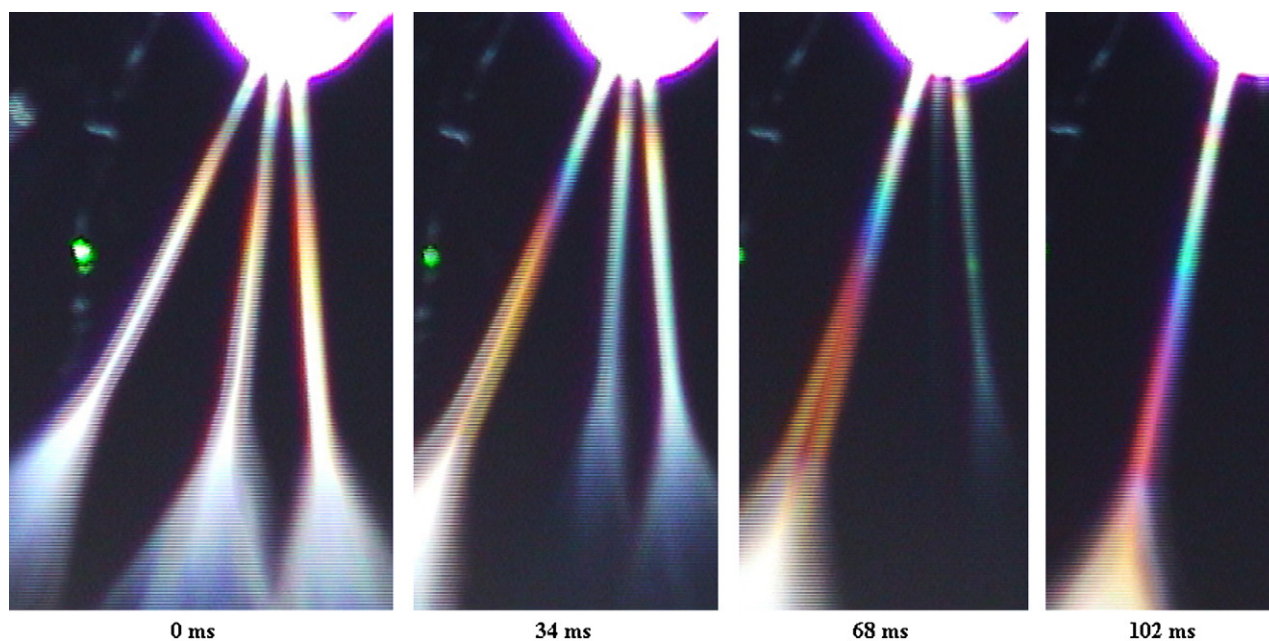


Fig. 26. Changes with time of three jets flowing from the same drop. The elapsed time after the three jets were first observed. Reprinted with permission from Reneker and Fong [2]. Copyright 2005. American Chemical Society.

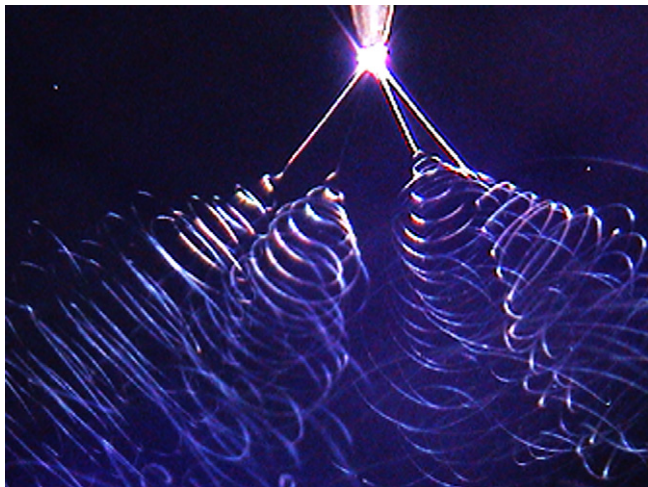


Fig. 27. Four jets from one drop, each with a well developed electrical bending coil.

is caught on a rotating drum winder with a surface velocity of a few meters per second, the loop is pulled into straight, parallel segments aligned with the circumferential direction of the winder [42]. These straight parallel segments must be connected by bends at their ends, but the inability to follow a single fiber as it emerges at and plunges beneath the surface of the sample makes it very difficult to observe such bends in scanning electron microscope images of the sort shown in Fig. 29. Winders of this sort are commonly used to produce sheets of nanofibers with reasonably large fractions of the material in fibers that are aligned along the direction of motion of the surface of the winder. Even higher alignment, with fewer of the u-shaped bends necessarily associated with pulling a fiber loop into parallel segments, was demonstrated [43,44] with a winder moving at a higher velocity, utilizing a sharp edge to

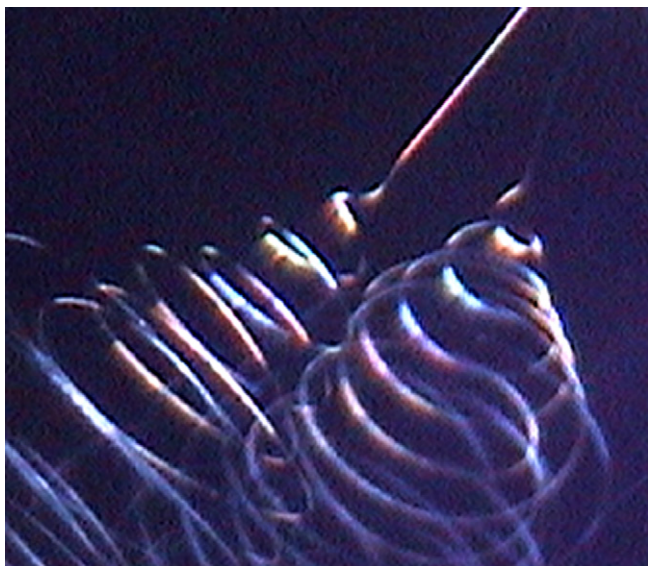


Fig. 28. An enlargement of a section of Fig. 27, enhanced to emphasize the colors and streaks associated with the glints on the leftmost electrical bending coil.

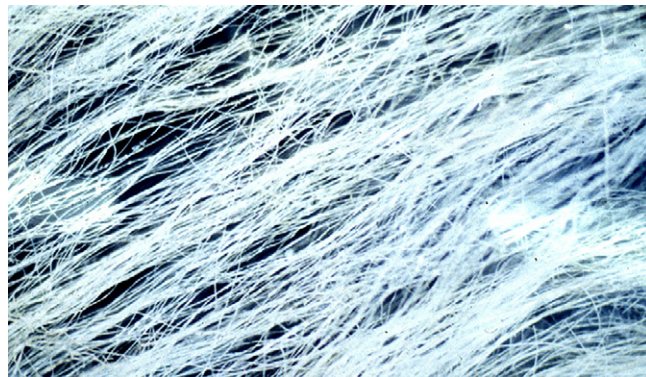


Fig. 29. Scanning electron micrograph of 300 nm diameter polybenzimidazole nanofibers. The orientation of the fibers was relaxed by the cuts made to prepare this sample for the scanning electron microscope, but a predominant orientation of the fibers along one diagonal of the image is clearly evident.

concentrate the electric field, and optimization of the electrospinning conditions.

If a fluid jet is stopped on a surface, either solid or liquid, the compressive forces along the axis often result in buckling instabilities similar to those observed with a slender column compressed along its axis. There are many interesting possibilities for buckling of an electrified, coiled, solidifying fluid jet, some of which are described in Sections 5.1 and 5.3.

### 5.1. Optical images of collected fibers

Interference colors of the sort described in Section 4.3 are also useful for observing the diameter of solid fibers in the range from about 0.5 to 15  $\mu\text{m}$ , see Fig. 30. The nearly straight

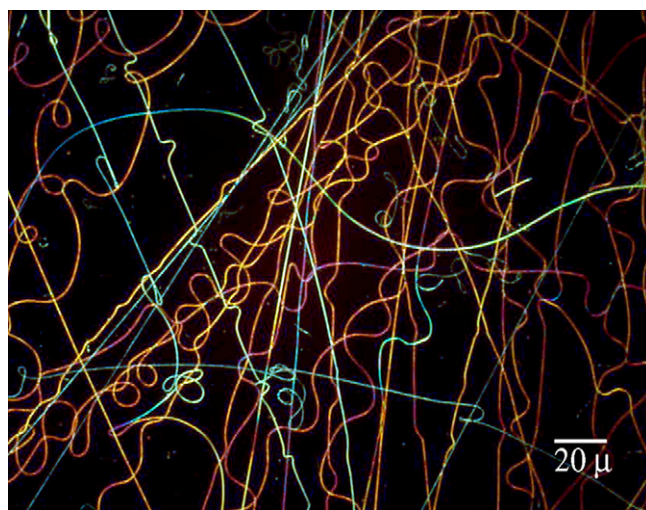


Fig. 30. An optical micrograph of a collection of segments of nanofibers of poly(etherimide) fibers electrospun from a 20% solution in 1-methyl-2-pyrrolidone with diameters ranging from more than 0.5 to less than 5  $\mu\text{m}$ . The illumination came from the viewing direction in the form of a cone of white light produced by an “epi” lens in which the objective is surrounded by an annular condenser lens. A cone of illumination from behind the sample also produced these colors. The “epi” condenser lens provides white light at the directions needed to make the interference colors visible in every segment of a fiber lying in the object plane of the microscope objective lens, independently of the azimuthal orientation of the segment.

fibers that cross the image are typical of the electrically driven bending instability. The repeated bends, script “e”, and other features that have characteristic repeat distance of a few tens of microns are typical of the mechanical buckling features produced when a fluid jet is stopped on a surface.

It is most likely that all the fiber segments in this image were part of one long fiber that varied in diameter by a factor of 2 or 3 as it crossed and re-crossed the area shown. Most of the individual segments in the picture show small changes in color that suggest changes in the diameter of 10 or 20%, sometimes occurring abruptly and sometimes occurring gradually. A similar range of variation of the diameter was also observed in scanning electron microscope images of other areas of this sample. When needed, it is feasible to compare optical images of such colored fibers with scanning electron microscope images of the same fiber in order to provide a more accurate interpretation of the colors for a particular light source and lens combination.

## 5.2. Conglutination and garlands

Conglutination refers to the processes by which partially solidified jets can produce fibers that are attached at points of contact. Garlands are nanofiber networks formed when loops of an electrospinning jet conglutinate in flight.

### 5.2.1. Conglutination

A partially solidified segment of a jet that intersected another segment may conglutinate with the segment it contacted and thereby changes the mechanical properties of both the jet in flight and the collected mat of fibers. Strong attachments at crossing points stiffen the mat.

The details of the conglutinated region were affected by the fluid mechanical properties of the segments involved. The two conglutinating segments may have the same properties, for example, fluid segment contacting another fluid segment, or quite different properties, for example, a fluid segment contacting a solid segment. The detailed morphology of a conglutinated junction also provided an experimental way to observe changes in the fluid mechanical properties as a jet solidified.

Relatively fluid segments of a jet, crossing at a small angle, tend to be pulled together into a larger fiber, for a short distance, by the surface tension. Solid segments can cross at any angle with only minimal morphological changes at the crossing point.

Fig. 31 shows conglutinated segments of jets of poly(ethylene naphthalate) (PEN) that were electrospun in a vacuum. The vertical fibers to the right of the scale bar (2 through 10) were collected and solidified on a solid surface. The diagonal jet (0) arrived at a later time, in a molten state. The vertical fiber segments (2 through 10) merged with the diagonal segment and solidified. While fluid, the shape of each intersection changed so that the points of attachment were offset, as seen most clearly in the smaller fibers (3), (5), and (8). All these small fibers became more nearly perpendicular to the molten segment (0) where they joined it. The vertical fiber (1) that intersects the scale bar arrived later, and did not merge so completely with the diagonal fiber (0), although they were

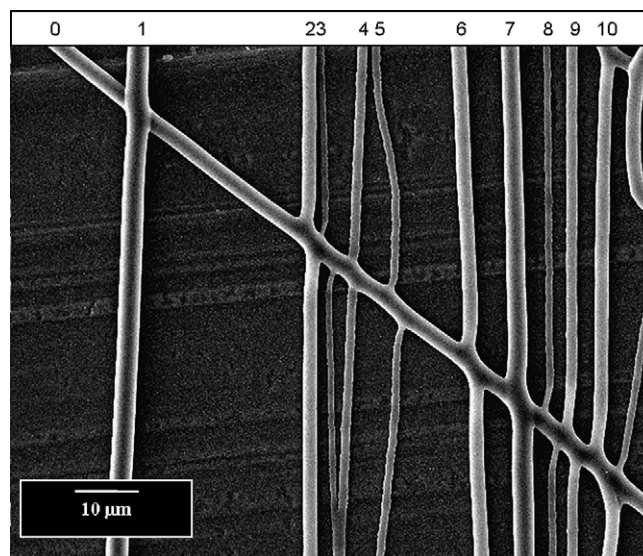


Fig. 31. Segments of polyethylene naphthalene fibers electrospun from the melt in a vacuum. Note the varied morphology of the conglutinated crossing points. The segments in this picture are numbered at the top margin.

slightly deformed at their crossing point. All these fibers, since they are stuck together at points of contact, are conglutinated in ways that depend on their angle at the point of contact, and their fluidity at the time they came into contact.

Conglutination is an important factor in the determination of the mechanical properties of non-woven sheets or of the garlands described in the next section. Biomedical applications such as the ability to be sutured into place also depend on the amount of conglutination that is present in a non-woven sheet. The formation of a skin on a jet that leads to ribbons, as described in Section 5.2.3, also affected the conglutination process. Section 6.1 shows how the conglutination of electrospun nanofibers of a crystalline polymer can control the nucleation of crystals within an uncrystallized jet.

### 5.2.2. Garlands

The expanding coils generated by the electrically driven bending instability were often quite symmetrical around the axis of the straight segment, but circumstances were encountered in practical devices for electrospinning which reduce this symmetry. The jet path then became quite complicated. While the Coulomb interactions between segments were repulsive, their combination with mechanical forces brought some segments of the same or nearby loops together so that segments crossed and touched. Since the jet was usually quite fluid near the onset of the first bending instability, the touching point conglutinated and formed a closed loop attached to the jet.

The formation of such loops happened repeatedly in the first few turns of the coil formed after the onset of the electrically driven bending instability as a solution of about 15% polycaprolactone in acetone was electrospun [45]. The closed loop sometimes involved a fraction of one turn of the electrical bending coil, and sometimes included several turns. The lengths of the segments in a closed loop continued to increase since the segments carried excess electrical charge and the jet

was fluid. The overall mechanical properties of the jet and the development of the path changed when such intersection and conglutination events occurred.

The usual consequence of intersection and conglutination of the jet path with itself, in flight, was the creation of a complicated network or chain of connected loops of different sizes. The connected loops change the jet path, from coils that could be pulled into a straight line, into a connected network of segments of different length, which is called a “garland”. When such a garland is stretched mechanically, some of the shorter segments appeared as small, closed loops attached to a fiber. Other segments were stretched taut, or even broken if the mechanical stretching was sufficient. The longer segments of a loop were sometimes slack, as shown in parts (a) and (b) of Fig. 32. Fig. 32(c) shows two ways that small loops were made.

The overall behavior of a garland during electrospinning is shown in Fig. 33 [45]. This garland began to form near the beginning of the electrically driven bending instability. The typical diameter and typical pitch of the electrical bending coil formed by the garland shown in Fig. 33 were both a few centimeters. These large coils occur because the garland, with all its complicated internal structure, is an electrically charged, mechanically weak column, and therefore is subject to the same kind of electrical bending instability as a single jet, but on a much larger scale. The much smaller coils formed by the jet path about 4 mm below the orifice are shown at higher magnification in Fig. 34. These coils are only a few millimeters in diameter.

The evolution of the region near a small loop, which formed in the first few turns of the electrical bending coil is followed through Frames 6–18. Many other examples of conglutination of the jet with itself were found by examination of this video sequence.

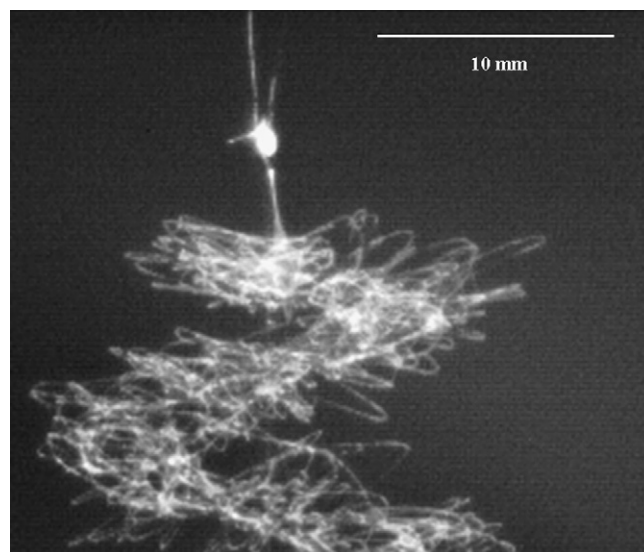


Fig. 33. A garland seen at lower magnification. The drop is bright and the straight segment is around 3.5 mm long. Evolving details of the region at the downstream end of the straight segment are shown in Fig. 34. When the coils of the fluid jet contacted each other and conglutinated, a garland of loops formed. Since the garland was flexible and carried electrical charge, it developed its own larger scale electrically driven bending instability. Slightly more than one turn of the resulting electrical bending coil of a garland is shown in this figure. Reprinted with permission from Elsevier, Ref. [45], Copyright 2002.

### 5.2.3. Skins on the jet and ribbon shaped nanofibers

Jets of polymer solutions often (but not always, as described in Section 3.1 on branching) had circular cross-sections. The cross-sectional shape of a fiber that was created by evaporation of the solvent depended on the transport of solvent molecules through the drying surface of the jet. The circular cross-section of the jet often shrank homogeneously and formed a fiber with a circular cross-section. At the other extreme, a mechanically

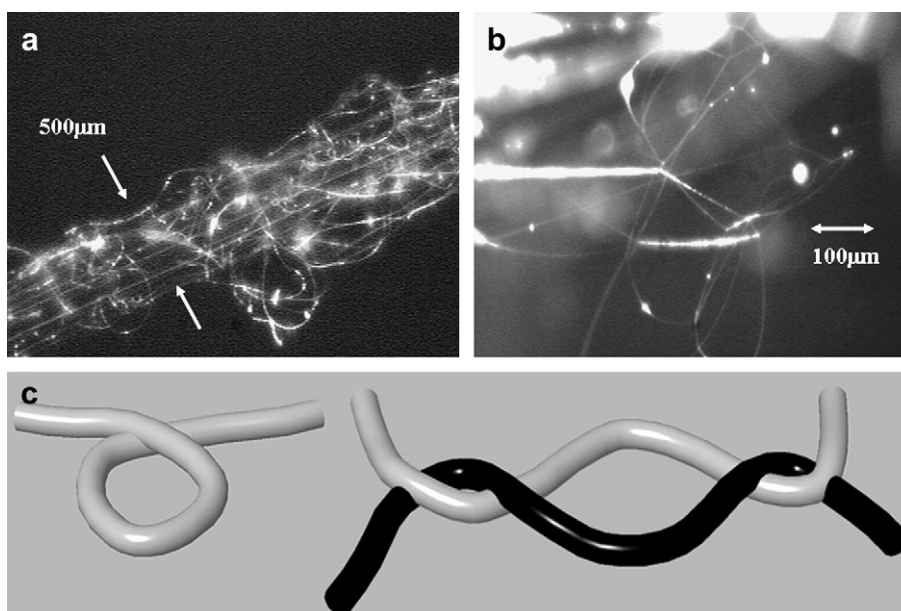


Fig. 32. (a) A short segment of a garland yarn, (b) details of the conglutinated solid fibers, and (c) a diagram of a loop in a segment of one fiber, and another loop made by short, overlapping segments of two fibers in much longer segments. Reprinted with permission from Elsevier, Ref. [45], Copyright 2002.

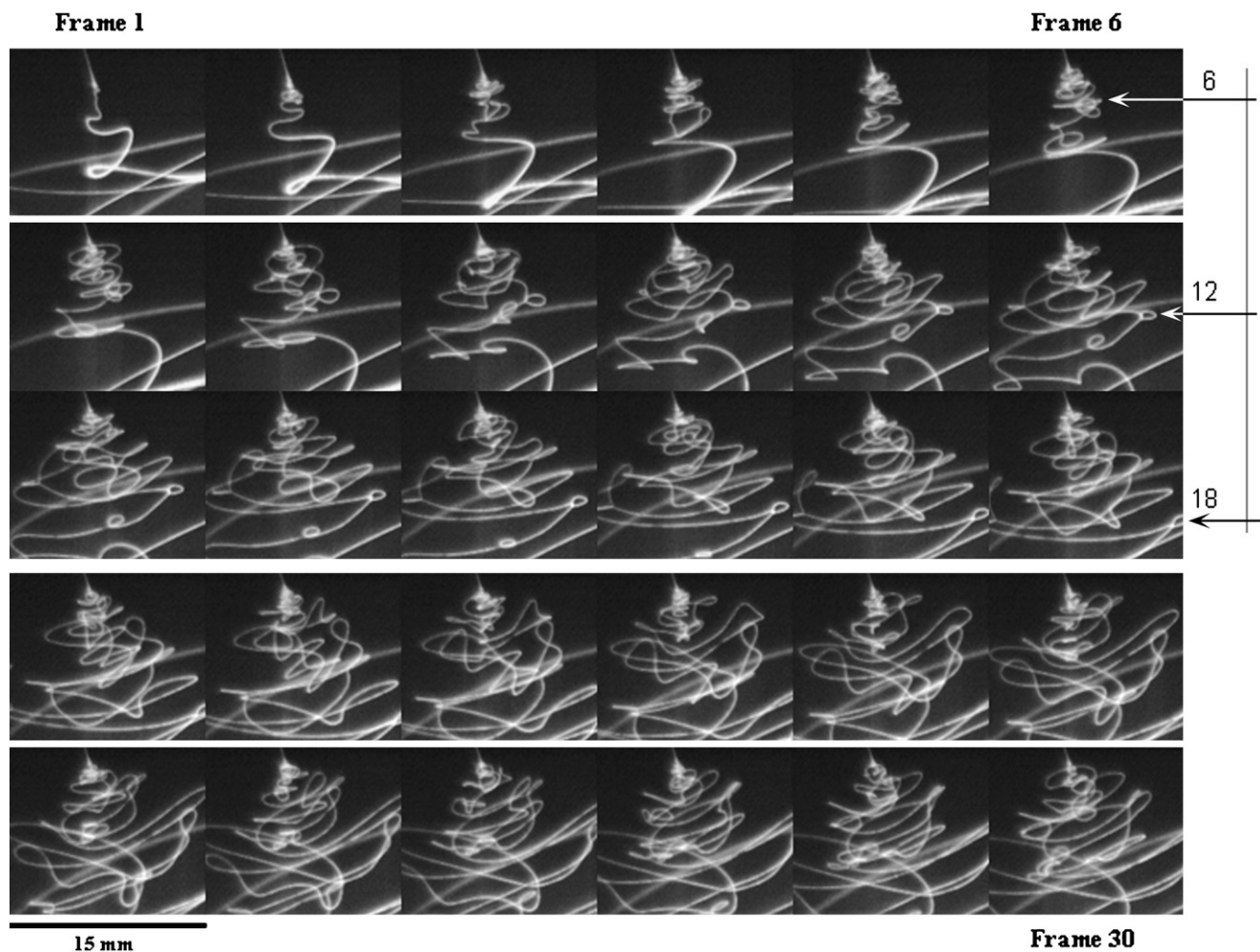


Fig. 34. Evolution of the first few turns of the first electrical bending coil, showing the positions of a small loop at successive time intervals of 0.5 ms. Three of these positions, in the rightmost column, are identified with arrows in frames 6, 12, and 18 (15% polycaprolactone in acetone, 5 kV, 240 mm gap, 2000 frames per second, 0.025 ms exposure). Reprinted with permission from Elsevier, Ref. [45], Copyright 2002.

strong skin formed on the jet, but before all the remaining solvent diffused through the skin, the skin solidified. If the concentration of the polymer in the solvent was around 10%, as was typical, the skin thickness required to contain all the polymer was only about 5% of the diameter of the fluid jet. As the evaporation progressed, the skin remained as a hollow tube, collapsed into a flat ribbon, or collapsed into other structures. The formation of fibers with wrinkled surfaces or porous interiors can occur as a consequence of different and changing combinations of solvent transport, mechanical properties, and fluid properties which affect the collapse instability modes. During drying of a jet the tensile and compressive strength of the skin increased and eventually dominated the effective surface tension and the rheological properties of the fluid.

The formation of a skin did not prevent the growth of branches during electrospinning of a poly(etherimide) solution. See Section 3.1, Fig. 13.

Fig. 35 shows a flat ribbon electrospun from a solution of 10% poly(etherimide) in hexafluoro-2-propanol [46]. The width of the ribbon was about 5  $\mu\text{m}$ , indicating that the diameter of the jet was about 3  $\mu\text{m}$  when the skin formed. The

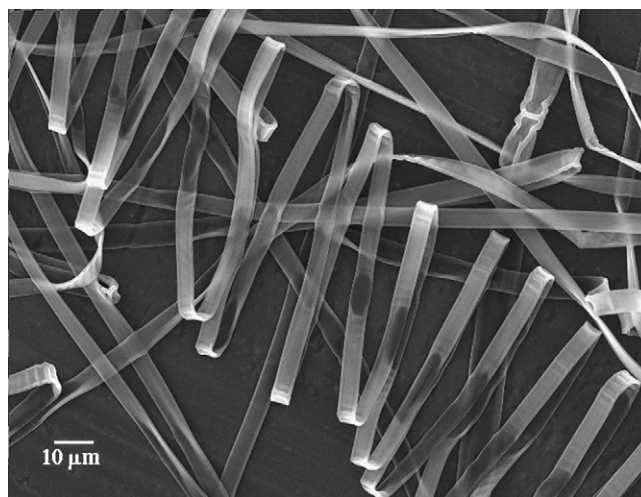


Fig. 35. Flat ribbon produced by electrospinning a solution of poly(etherimide) in hexafluoro-2-propanol [48]. Reproduced with permission from Koombhonge et al. [46]. Copyright 2001. John Wiley & Sons, Inc.

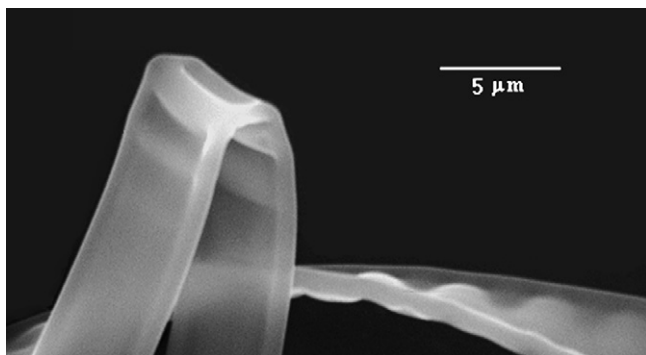


Fig. 36. A characteristic wrinkle pattern that developed at bends of a collapsed tubular fiber (a ribbon) electrospun from a 10% poly(etherimide) in hexafluoro-2-propanol.

uniformly folded ribbon, evident in the figure, indicates that the jet collapsed and folded as it was collected, as described by Yarin and Tchavdarov [47], and Cruikshank and Munson [48] for the buckling or folding of uncharged jets.

Fig. 36 shows a pattern of wrinkles that formed at the folds created when the coiled tubes collapsed into ribbons which buckled by folding as they were stopped by the collecting surface. The characteristic wrinkles are associated with the tension in the outer surface of the fold and the compression in the inner surface of the fold. Fig. 36 is an enlargement of a fold above and slightly to the right of the center of Fig. 35. More widely spaced wrinkles in a more gently curved segment are shown from a different perspective in the background.

The diagram in Fig. 37 shows ways that a thin walled tube can collapse into a ribbon with sharp folds, or if the walls were



Fig. 37. Modes of collapse of electrospun tubes of polymer into ribbons. Reproduced with permission from Koombhongse et al. [46]. Copyright 2001. John Wiley & Sons, Inc.

stiffer, collapse into a ribbon with rounded folds, which creates the dog-bone shaped cross-section. Collapse of core-shell nanotubes has also been described [10].

Evidence from birefringence patterns, of fibers with a dog-bone cross-section, showed that some of the molecules in the web between the rounded edges of the ribbon were aligned in a transverse direction with respect to the long axis of the ribbon, see Fig. 38. A full wave retardation plate in red light, used in conjunction with a polarizer and analyzer, allowed the directions of the longer and shorter axes of the index of refraction to be distinguished. Repulsive Coulomb forces, between the rounded edges of the collapsed tube where the charge concentration is highest for such a shape, and acting in the plane of the web can contribute to the development of the observed birefringence patterns [31,46]. Ribbons which were split along their axis were also observed, suggesting the possibility that when the solvent evaporated and the skin collapsed, the repulsive Coulomb forces in the plane of the ribbon grew large enough to pull a fiber ribbon apart laterally.

### 5.3. Buckling of fluid jets

Buckling of an electrospinning jet was observed when the stationary surface of the collector intercepted the wet or molten fluid jet, both before and after electrical bending of the jet occurred. Buckling coils from an electrospun jet of molten polycaprolactone were observed by Rangkupan and Reneker [49]. Nanofibers with no buckling were collected much further away from the tip than the distance at which the electrical bending instability occurred.

In subsequent experiments, an inclined collector, which was moved laterally to vary the distance from the tip to the collector continuously, was used to observe the effects of stopping and collecting the jet. Buckling coils and electrical bending coils were collected sequentially as the distance from the tip to the collector increased. The shapes of the coils varied in interesting ways that depended primarily on the distance from the tip to the point at which the jet impacted the collector. Since the diameters of the electrical bending coils increased rapidly and were larger than the nearly constant diameter of the buckling coils, electrical bending and buckling were clearly distinguished.

Observations [50] of a fluid jet of nylon 6 dissolved at a 10% concentration in an 8/2 weight ratio mixture of

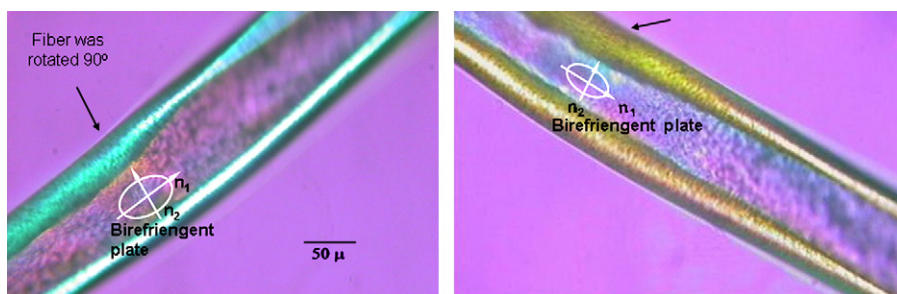


Fig. 38. A relatively large poly(etherimide) ribbon, which has a dog-bone cross-section, photographed between crossed polarizers. The yellow areas of the web in the left figure just above the  $n_2$  axis of the ellipse and the blue or blue-green areas in the same location in the right figure indicate that the polymer chains in the web are oriented in the transverse direction, while the molecules in the rounded folds at either side of the ribbon were oriented parallel to the long axis of the ribbon.



Fig. 39. The coils produced by buckling were about 15 μm in diameter. The buckling coils were superimposed on electrically driven bending instability coils with diameters of around 200 μm at the left and with much larger diameters at the right. Variations from the circular coils observed in buckling patterns include repeated script “e”, repeated script “8” and repeated semi-circular bends. Buckling coils maintained nearly the same diameter and can thereby be distinguished from the electrically driven bending instability coils, the turns of which typically increase in diameter at a high rate. The collector was moved laterally at a rate of about 1 m/s. Reprinted with permission from Han and Reneker [50].

hexafluoroisopropanol and formic acid, collected near the point at which the electrical bending instability occurred, showed both kinds of coiling, see Fig. 39. The buckling frequencies in a particular jet of this sort were in the megahertz range, while the frequencies of the first order electrical bending coils were 10–100 times lower.

Buckling produced coils of nearly constant diameter, or more complicated periodic features on a similar scale. Sometimes the buckling produced a folded zigzag of short straight segments and at other times produced curved segments connected by sharp folds. Complicated transitions sometimes occurred near the onset of the electrical bending coils as the tip to collector distance increased, see Fig. 40.

A viscous jet may have either tensile or compressive forces along its axis. The periodic buckling was attributed to the occurrence of compressive forces as the jet decelerated at the collector. The fluid mechanical analogue to buckling of a compressively loaded slender solid column occurred [47] when the axial compressive stresses along the jet reached a sufficiently high value. Jets with circular cross-sections first buckled by formation of sharp folds and then by coiling, as the compressive forces along the axis increased. Jets that formed ribbons [48] generally buckled in the sharp folding mode. See Section 5.2.3. for examples of a buckled ribbon.

## 6. Inside electrospun nanofibers

Although polymer nanofibers are thin, they may contain many polymer molecules in various morphological forms. Mixtures of molecules often phase separate. Particles of many substances are sequestered. Several interesting examples are described in this section.

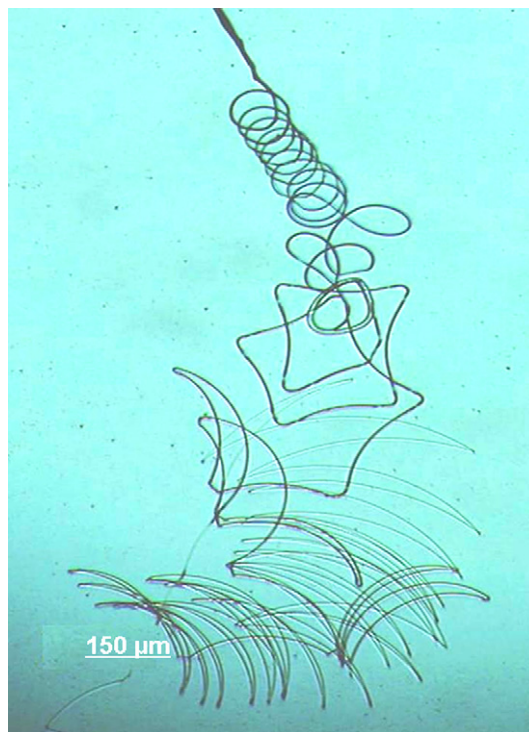


Fig. 40. The distance from the tip to the collector changed at a steady rate from the top to the bottom of this figure. From the top, a straight segment developed buckling coils which transformed, as the distance changed, into zigzags of gently curved segments connected by sharp folds, “squares” with sharply curved corners, and finally into zigzags of curved segments which suggest a pendulum like motion of the straight segment. Reprinted with permission from Han and Reneker [50].

Many nanofibers are thin enough to be transparent in the beam of a transmission electron microscope. The fibers, and particles contained in the fibers, were imaged and their diffraction patterns obtained with low radiation dose techniques that extracted information from a large fraction of the electrons that passed through the polymer fiber. Electrospun nanofibers provide a new and convenient way to investigate fine details of the morphology of polymer fibers.

### 6.1. Nanofibers and the morphology of crystalline polymers

Nanofibers provide interesting examples of crystallization development and crystalline morphology for examination by electron microscopy, electron diffraction, optical microscopy, X-ray diffraction, and other techniques.

Fig. 41 shows the nucleation of crystallites with a preferred orientation by an electrospun nanofiber. A thin nanofiber of polyethylene oxide made by electrospinning was deposited on a glass microscope slide along the line indicated by the white arrows in the figure. Then a much larger diameter segment of the jet, in the fluid state, was collected from near the tip of the electrospinning apparatus. As the solvent, water, evaporated, the polyethylene oxide crystallized into spherulitic and other arrays of folded chain lamellar crystals which appear as tiny elongated white bars in part (a) of the figure. Two views

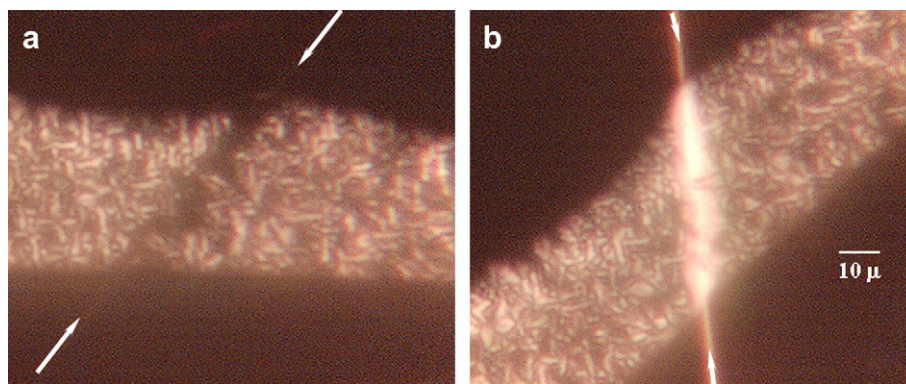


Fig. 41. A wet jet of polyethylene oxide that landed on a nanofiber electrospun from the same solution. This is a particularly detailed example of conglutination between a dry nanofiber and a very fluid jet. Reprinted with permission from Elsevier, Ref. [45]. Copyright 2002.

are shown of the region where the wet jet covered the dry nanofiber, as observed between crossed polarizers in an optical microscope. In part (a) the birefringent nanofiber was oriented so that it was dark and in part (b) the same nanofiber was rotated  $45^\circ$  so that it was bright. The crystalline arrays that grew within a few microns of the nanofiber show a similar behavior, appearing dark in (a) and bright in (b). This behavior of the birefringence showed that the polymer molecules that were oriented along the nanofiber axis nucleated many crystals in which the polymer chains in the polyethylene oxide crystals were parallel to molecules in the nanofiber.

The nanofiber shown in Fig. 41 was guided by mechanical and electrical forces. This experiment demonstrates a way in which novel structures of crystalline polymers can be designed, engineered and produced with polymer nanofibers. The diameter of the column of crystalline polymer affected by the crystal nucleation is about 10 times larger than the diameter of the nanofiber. The volume of the affected region is about 100 times larger than the volume of the controlling nanofiber.

### 6.2. Crystallization of rapidly solidified poly(*meta*-phenylene isophthalamide) nanofibers in an oriented yarn

Electrospinning generally resulted in birefringent fibers, indicating that the molecular chain axis was aligned parallel to the fiber axis, which agrees with the predicted occurrence of the transformation of the macromolecules from a coiled to an elongated conformation during electrospinning [26]. However, the local crystalline perfection that produces sharp diffraction spots was not completely developed in rapidly dried or coagulated fibers. The crystallographic precision of the molecular positions and conformations, for poly(*meta*-phenylene isophthalamide), poly(vinylidene fluoride), and polyaniline, was improved by annealing at a temperature lower than the crystallographic melting temperature. Some crystalline polymers that do not have hydrogen bonds showed sharp diffraction peaks immediately after solidification, with no necessity for annealing.

Nanofibers of poly(*meta*-phenylene isophthalamide), a high performance, temperature resistant polyamide, were

electrospun at room temperature from a solution of the polymer in *N,N*-dimethylacetamide [51]. The molecular weight of the polymer was around 90,000 g/mol. Optical microscopy with polarized light showed that each nanofiber was strongly birefringent, indicating that the spun polymer chains were aligned parallel to the axis of the nanofiber.

A wide angle X-ray diffraction pattern from a loosely twisted yarn of as-spun nanofibers is shown in Fig. 42. The very diffuse equatorial diffraction spots, shown in red, indicate that the polymer crystallites were small and imperfect, but aligned in the general direction of the axis of the yarn.

Fig. 43 shows the wide angle X-ray diffraction pattern of the poly(*meta*-phenylene isophthalamide) yarn after it was annealed, for 4 min in air, at  $320^\circ\text{C}$ . Sharp diffraction spots were observed at angles that correspond to the Bragg diffraction from crystallographic planes of triclinic crystals. The thermal annealing improved the irregular packing of the as-spun fibers, presumably by allowing many cooperative picometer-scale

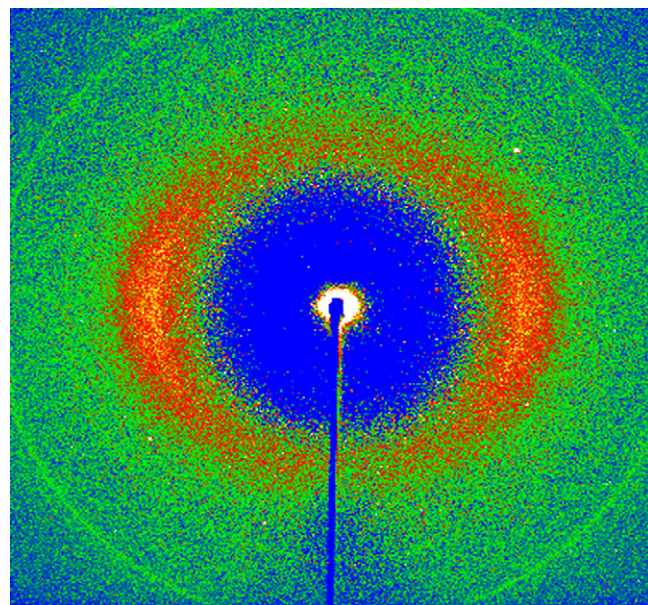


Fig. 42. A wide angle X-ray diffraction pattern from a yarn of twisted as-spun poly(*meta*-phenylene isophthalamide) nanofibers.

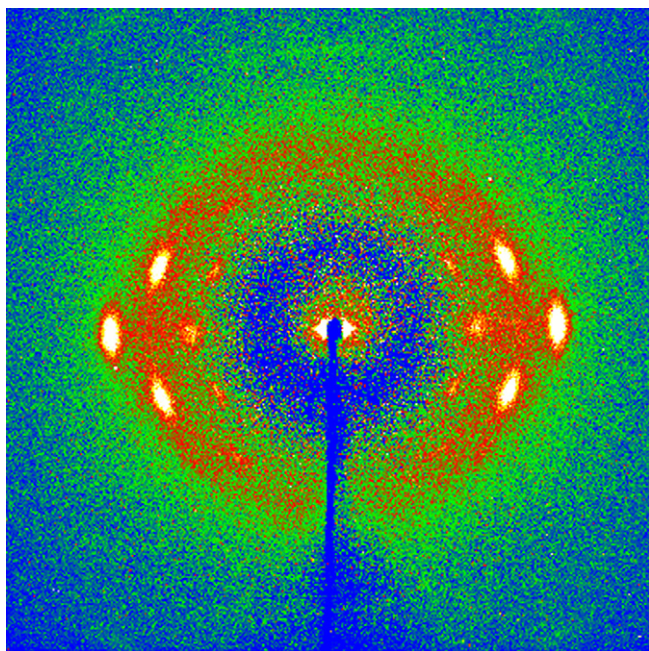


Fig. 43. X-ray diffraction pattern of an annealed sample of the same yarn used in Fig. 42.

movements of molecular segments, which eliminated small voids, established hydrogen bonds, adjusted conformations by small rotations around bonds, and thereby improved the fit of molecules into the crystals, while preserving the orientation of the polymer chains along the axis of the nanofiber. Electron diffraction patterns from single nanofibers of poly(*meta*-phenylene isophthalamide), annealed at the same temperature for the same time as the yarn, showed sharp diffraction spots, in patterns and at angles consistent with the same information derived from X-ray diffraction [31].

Similarly, Liu [31] showed that birefringent poly(vinylidene fluoride) nanofibers, 200–300 nm in diameter, as electrospun from a solution of 24% by weight in dimethyl formamide, produced electron diffraction patterns with diffuse equatorial spots corresponding to interplanar spacings of 0.44 and 0.25 nm. After the nanofibers were annealed at 80 °C for 10 min, short azimuthal arcs appeared at sharply defined interplanar spacings characteristic of the orthorhombic  $\alpha$ -form of poly(vinylidene fluoride).

### 6.3. Encapsulation of molecules, biological cells, carbon nanotubes and particles in nanofibers

Many biological colloidal particles, chemical reagents, and other particulate materials [52] were encased inside nanofibers of single polymers, blends, or copolymers. Such materials or objects, dispersed or dissolved in a polymer solution, flowed into and with the jet and necessarily remained with the nanofiber when the solvent evaporated. Electrospun polymer nanofibers provide a generally applicable method for holding and protecting particles and molecules.

Nanofibers containing green fluorescent labeled albumin molecules were electrospun from a solution of poly(ethylene

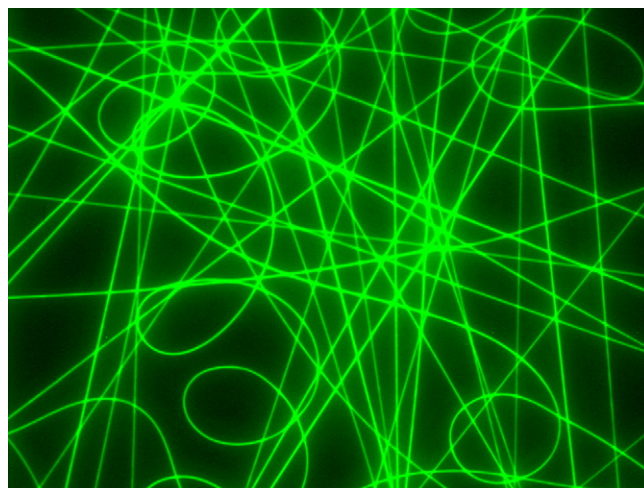


Fig. 44. A fluorescence microscope image of nanofibers of poly(ethylene oxazoline) and fluorescent labeled albumin.

oxazoline) in water. The fluorescent protein molecules were dispersed uniformly throughout the electrospun fibers as shown in Fig. 44. Other protein molecules such as trypsin were shown to be active [53] when the surrounding polymer was re-dissolved, after storage at room temperature for eight weeks. Electrospinning of proteins into a protective polymer matrix is a broadly useful way to preserve proteins and other biological substances at room temperature.

Almost anything that can be dissolved or suspended in a polymer fluid that is suitable for electrospinning can be sequestered within the nanofiber produced by electrospinning. If a particle larger than the diameter of the nanofiber flows into the jet, the jet will momentarily expand to encapsulate the particle, and then shrink back to its nanoscale diameter. Electrospinning is therefore a useful method for encapsulating, sequestering, and protecting particles, cells, organelles, molecules, viruses, colloidal particles, chemical reagents, fluid droplets, pollens, spores and many other such substances inside polymers. The encapsulated substances were released by dissolving the polymer nanofiber, or used in situ. The encapsulation of proteins in core–shell structures was recently reported [54,55].

The left hand part in Fig. 45 shows a pollen particle that was mixed into an alcohol solution of polycaprolactone and poly(ethylene oxazoline). The mixture was electrospun into a nanofiber that contained both polymers. Since the diameter of the channels for flow of the fluid through the electrospinning apparatus was much larger than the approximately 10  $\mu\text{m}$  diameter of the pollen particle, it was carried along into the beginning of the jet, which had a diameter of a few hundred microns. The jet elongated, dried, and became smaller in diameter than the pollen particle. The dried polymer blend made a smooth, thin coating on the pollen particle. Polycaprolactone is not soluble in water, but poly(ethylene oxazoline) is. After the polyethylene oxazoline was washed away with water, part of the surface of the pollen particle was revealed, but the pollen particle was still held firmly in the network of polycaprolactone fibers that remained.

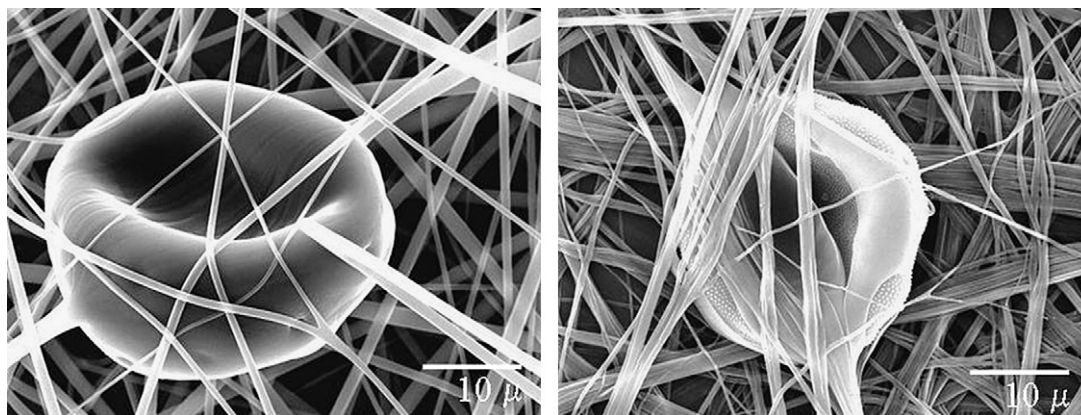


Fig. 45. A pollen particle electrospun inside a blend of polycaprolactone and water soluble poly(ethylene oxazoline). Dissolution of the poly(ethylene oxazoline) revealed the polycaprolactone nanofibers that continued to hold the pollen particle in space.

#### 6.4. Phase separation in block copolymers

Since phase separation during solidification of block copolymers often occurs on the scale of 10 nm, electrospun nanofibers provided a convenient sample for observing the phase separation process [56]. Transmission electron micrographs, of electrospun nanofibers stained with osmium, revealed interesting behavior of block copolymers. The rapid solidification rates, the high elongations, and the large surface area per unit mass, which were easily achieved by electrospinning a copolymer solution into nanofibers, add nanofibers to the repertoire of contemporary methods for investigating the phase separation and morphology of block copolymers.

Nanofibers were electrospun from a solution of a tri-block copolymer of poly(styrene-*block*-butadiene-*block*-styrene). The samples of nanofibers stained by osmium tetroxide were examined with a transmission electron microscope [56]. The osmium stain reacted selectively and made the regions that contained the poly(butadiene) blocks appear dark in the electron micrographs, while the regions that contained polystyrene remained light.

The stained areas in the as-spun nanofiber shown in Fig. 46(a) were about 5 nm wide with lengths ranging up to 20 nm in the axial direction. A nanofiber from the same preparation was stored at room temperature for 20 days before it was stained. The long range order characteristic of phase separation in bulk samples developed. The sizes of the phase separated regions grew to around 10 nm. The regions occupied by each phase elongated in a direction parallel to the axis of the nanofiber, indicating a morphologically stored memory of the large extensional flow encountered during electrospinning. More rapid growth of the two phases is evident in the nanofibers annealed at 70 °C, and is shown in Fig. 46(b) and (c). Five minutes of annealing at 70 °C had about the same effect as 20 days storage at room temperature. Annealing for 20 min and for 1 h produced further changes in the morphology of the phase separated regions.

Some beaded nanofibers (see Section 3.3), created by the capillary instability of the jet of block copolymer solution during electrospinning, were observed. Fig. 47 shows ellipsoidal beads with a length of about 100 nm parallel to the fiber axis and a diameter of about 60 nm. The diameter of the nanofiber

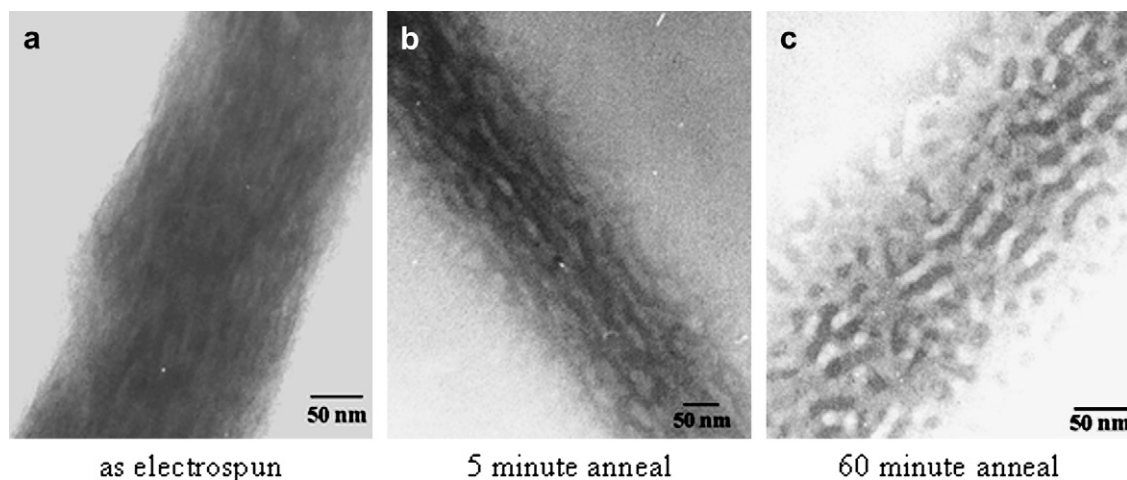


Fig. 46. Electron micrograph of an as-spun nanofiber of poly(styrene-*block*-butadiene-*block*-styrene) stained with osmium and examined by transmission electron microscopy. Transmission electron micrographs of the electrospun tri-block copolymer nanofibers, annealed for different times before staining with osmium tetroxide. Reproduced with permission from Fong and Reneker [56]. Copyright 2000. John Wiley & Sons, Inc.

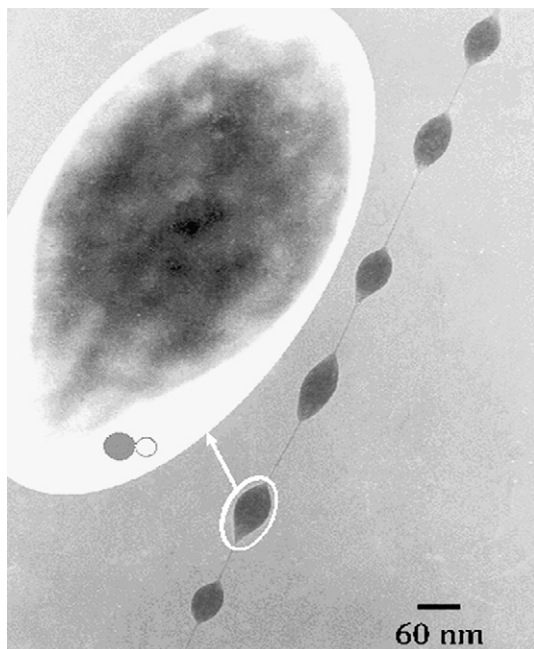


Fig. 47. Transmission electron micrograph of a poly(styrene-*block*-butadiene-*block*-styrene) nanofiber with beads stained with osmium tetroxide. The inset shows an enlargement of one of the beads. The darker circle near the bottom of the inset shows the diameter of a spherical volume that would contain the polybutadiene in a typical molecule, and the adjacent white circle represents the total volume of the two polystyrene blocks in the same way. Reproduced with permission. Cover picture, *Journal of Polymer Science Part B: Polymer Physics*, volume 38, issue 1. Copyright 2000. John Wiley & Sons, Inc.

between the beads was about 3 nm, which indicates that the fiber cross-section accommodated about 40 molecules, half of which were at the surface. A typical molecule was longer than the separation between the beads. Stained and unstained areas were observed inside the bead. These regions had dimensions commensurate with the projected areas of the styrene and butadiene blocks. There is an indication of phase separation on a 10 nm scale in the enlarged image of a bead shown in the inset, particularly in the lower part of the inset. No evidence for phase separation was found in the thin fiber between the beads. The very small scale of phase separation in this tri-block copolymer is evident in comparison with the scale of phase separation in blends of polycaprolactone and polyethylene oxazoline described in Sections 3.3 and 6.3.

## 7. Special topics

Several curious and promising observations of the behavior of electrospun nanofibers are discussed in the sections that follow. A few intriguing speculations are included.

### 7.1. Small diameter fibers

The thin beaded fiber shown in Fig. 47 was, for a time, the thinnest electrospun nanofibers reported. More recently, Huang et al. [16] obtained clear transmission electron microscope images of nylon fibers with a diameter of 1.6 nm, and good evidence for fibers with diameters of around 1 nm.

Such fibers contain only two or three molecules in a cross-section.

There are many published images of single polymer molecules, particularly of DNA, lying on a flat substrate, that were observed with scanning probe microscopy. Clearly the limit of thinness of a polymer fiber is one molecule, but most familiar polymer molecules, at room temperature, would contract into a more or less random coil unless each molecule was supported on a surface, or stabilized by pulling at its ends. As the number of molecules twisted or crystallized together is increased to three or more, the increasing stiffness would ultimately become large enough to prevent extended molecules from collapsing.

Electrostatic injectors for mass spectrometers produce individual electronically charged polymer molecules. The electronic charge tends to stretch each polymer molecule into a completely extended conformation. An experiment that observes the electron diffraction pattern of molecules launched into an electron microscope by an electrostatic injector of the sort used in mass spectrometers appears to be a feasible way to examine this possibility. This speculation remains to be proven.

### 7.2. Coated fibers

Electrospun nanofibers of poly(*meta*-phenylene isophthalamide) were coated with carbon or metals by chemical or physical vapor deposition techniques [57] and with various substances [58]. Fig. 48 shows a 30 nm diameter fiber coated with a 30 nm thick layer of carbon, to make a composite fiber

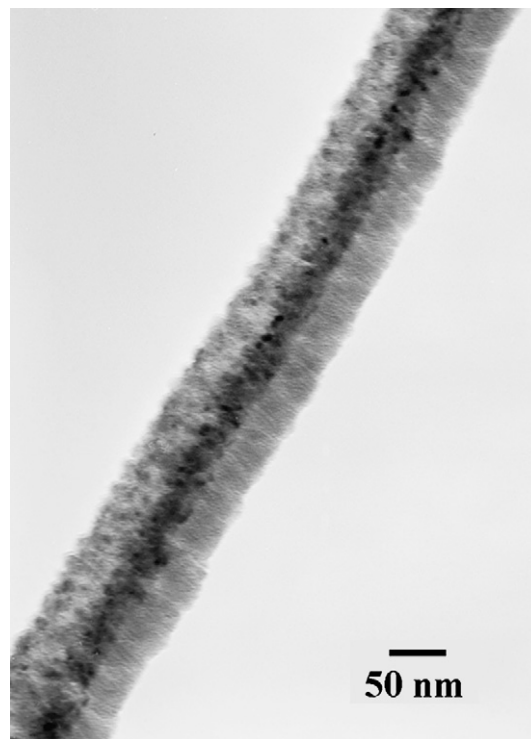


Fig. 48. Poly(*meta*-phenylene isophthalamide) fibers coated with carbon by a direct current magnetron sputtering process [57].

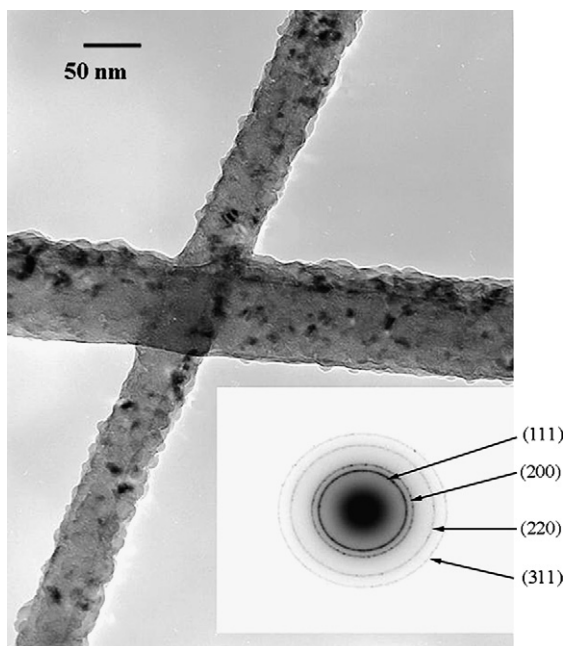


Fig. 49. Poly(*meta*-phenylene isophthalamide) fibers coated with aluminum by a high frequency electromagnetic plasma sputtering process. The inset is an electron diffraction pattern that shows rings characteristic of polycrystalline aluminum. The aluminum was converted to aluminum oxide by heating the nanofibers in air. The polymer disappeared, leaving a tube of aluminum and aluminum oxide [57].

with a diameter of 90 nm. The nanofibers were coated with carbon deposited from a plasma containing argon and carbon atoms. The plasma was created by a high frequency electromagnetic field. Poly(*meta*-phenylene isophthalamide) nanofibers were also coated with copper and with aluminum. Transmission electron microscopy and electron diffraction were used to observe the thickness, uniformity, and grain size of the coatings. The copper crystals (not shown) were less than 10 nm across, with points that protruded radially. Electron diffraction patterns obtained from single coated fibers showed rings, indexed as arising from (110), (111), (211), (220) and (311) planes of copper. The rings were of almost uniform intensity along their circumference.

The aluminum coatings shown in Fig. 49 were composed of aluminum crystals about 10 nm across. The electron diffraction patterns showed rings corresponding to diffraction from the (311), (220), (200), and (111) planes. The intensities along the circumferences of the rings indicated a random distribution in the direction of the axes of the aluminum crystallites. Upon heating in air, the aluminum was oxidized and diffraction patterns characteristic of aluminum oxide were observed. During the heating in air the polymer nanofiber disappeared leaving a thin shell of aluminum oxide.

Fig. 50 shows a network of very thin MPD-I nanofibers coated with aluminum by a sputtering process. The network was supported on larger nanofibers that formed an irregular network with holes a few microns across. The enlarged image at the right shows the roughness and other details of the

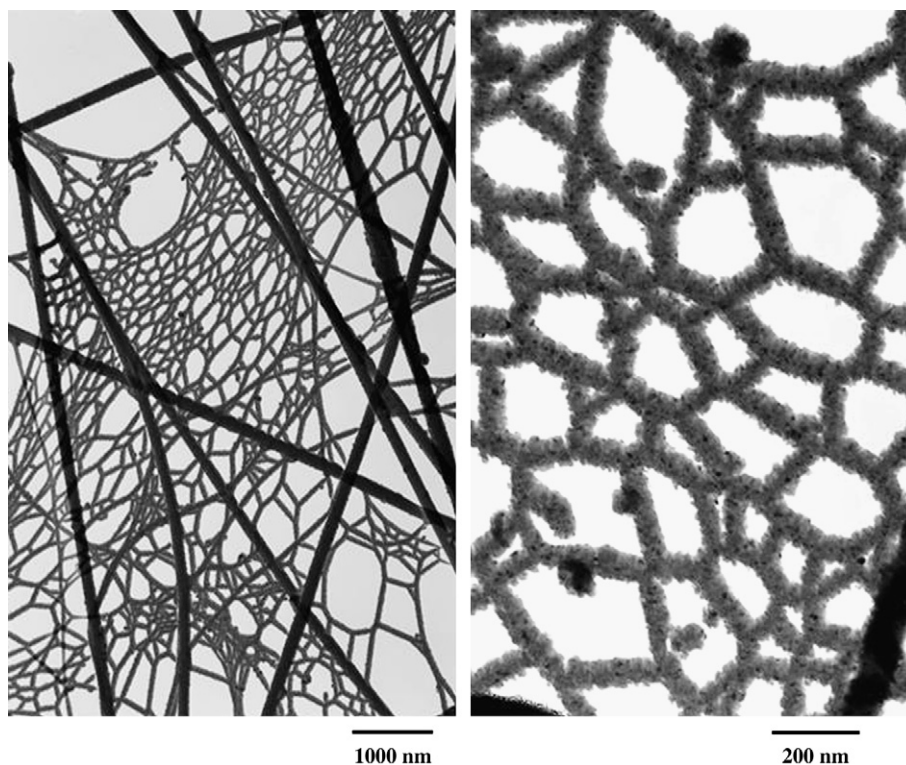


Fig. 50. Very thin nanofibers coated with aluminum. The left part shows the supporting networks of larger polymer fibers. The right part of the figure shows the size of the crystals of aluminum by diffraction contrast. The dark spots show that aluminum crystals that were favorably oriented to produce diffraction contrast [57] were around 10 nm in diameter.

coating. The coated nanofibers in the network were less than 50 nm in diameter. The uncoated fibers that formed the network were only a few tens of nanometers in diameter.

### 7.3. Hierarchical structures of graphite nanofibers and fullerene nanotubes

Carbon nanofibers can be made by electrospinning a soluble polymer, such as polyacrylonitrile, into nanofibers and then converting the polymer to carbon by a well known thermal carbonization treatment. Organic molecules containing iron atoms (other metal atoms also work) were added to a solution of polyacrylonitrile. The iron bearing molecules decomposed during the carbonization treatment of the polyacrylonitrile and formed iron-rich particles on the surface of the carbon nanofiber. These iron-rich particles, which were liquid at the growth temperature, catalyzed the growth of many multiwall carbon nanotubes that formed branches attached to the carbon nanofiber. The iron-rich liquid particles were carried on the tips of the nanotubes during the growth process.

The resulting hierarchical structure [59], shown in Fig. 51, provided an electrically conducting path from each of the metal particles, through a nanotube and through the long carbon nanofibers,

to a contact with a macroscopic metal electrode. This hierarchical structure enables the design and construction of a continuous electronically conducting path between a myriad of 10 nm diameter metal particles and the edges of a thin sheet of carbon nanofibers with lateral dimensions of 10 or more centimeters.

Organic molecules, such as iron acetylacetonate, which contained iron atoms, were added to a solution of polyacrylonitrile that was electrospun and processed to become carbon nanofibers with iron-rich particles on their surface. These nanofibers were heated to a temperature of about 750 °C in an inert gas that was bubbled through liquid hexane at room temperature. The hexane decomposed and deposited its carbon in the liquid iron-rich particle. The carbon atoms made their way to and were deposited on the carbon nanofibers. A multiwall carbon nanotube, supporting the iron-rich particle on its tip, formed on each iron-rich particle. The number of nanotubes depended on the number of iron-rich particles created during the carbonization of the polyacrylonitrile nanofiber. The diameters of the nanotubes depend on the size of each iron-rich particle. The length of the nanotubes depended on the time that the hexane was supplied at the growth temperature.

All the parameters governing the growth of the nanofibers and the multiwall nanotubes can be adjusted to create

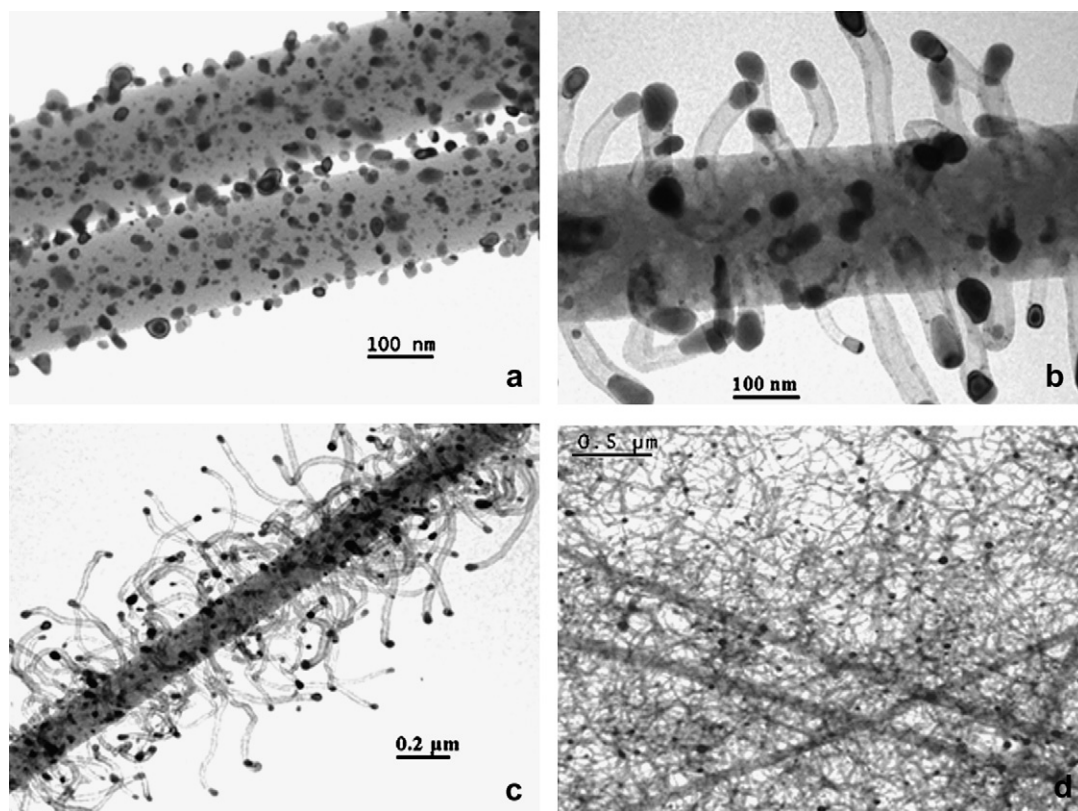


Fig. 51. (a) A carbon nanofiber produced by carbonization of nanofibers made from a solution of polyacrylonitrile that contained iron bearing molecules. After stabilization by heating in air followed by heating in hydrogen the iron, probably in the form of an iron-carbon compound such as  $\text{Fe}_3\text{C}$  (cementite), migrated to the surface of the carbon nanofiber and solidified into the small particles shown. (b) Exposure of heated fibers to hexane caused the iron to mediate the growth of multiwall carbon nanotubes, with a droplet of liquid iron and carbon at the growing tip of each nanotube. (c) Prolonged exposure to the hot hexane vapor increased the length of the multiwall carbon nanotubes. (d) The interstices between the carbon nanofibers were filled with nanotubes, and sheets that were tens of centimeters in lateral extent were prepared. The growth of sheets with much larger area is limited only by the design of the apparatus. Each iron-rich particle had a direct electrically conducting path from the particle to the periphery of the sheet. Reproduced with permission from Hou and Reneker [59]. Copyright 2004. Wiley-VCH Verlag GmbH & Co. KGaA.

a hierarchical structure with properties needed to work as an electrode for a fuel cell, battery, or for other redox reactions. The diameters of the particles and the ends of the nanotubes were so small that an electrical potential of a few hundred volts created an electrical field near the tips of the nanotubes that dissociated air molecules and produced an easily observable electrical current carried by airborne ions [60]. The interstices between the multiwall nanotubes provide channels through which water, hydrogen, oxygen, and other fuel or by-product molecules can flow, and thereby provide a basis for the design and construction of fuel cell electrodes with submicron thickness and large lateral dimensions.

The use of electrospinning to orient multiwall carbon nanotubes by electrospinning a solution of polyacrylonitrile in which the surface-oxidized nanotubes were dispersed without using any surfactants or binding agents was demonstrated [16,61]. The nanotubes were highly aligned along the axis of the nanofibers. Non-woven sheets of the composite nanofibers possessed enhanced electrical conductivity, improved tensile strength, higher thermal deformation temperature, thermal stability and dimensional stability. Optical absorption spectroscopy indicated that charge-transfer complexes formed between the surface-oxidized nanotubes and the polyacrylonitrile surrounding them.

#### 7.4. Electrospinning from a polymer melt

The vapor pressure of most molten polymers is very low so that it is feasible to observe the electrospinning behavior of jets of molten polymers in a vacuum [19,49,62]. Higher electric fields can be achieved in a vacuum than in air, since sparks occur in air at electric fields above 30 kV/cm. The higher electrical forces can overcome the higher viscosity and elasticity of a polymer melt compared to a polymer solution. The velocities observed for jets from polymer melts were an order of magnitude less than the velocities observed for jets of polymer solutions. Focused radiant heating of the molten polymer in a vacuum, to temperatures approaching the decomposition temperature, reduced the viscosity and the elasticity enough to allow electrospinning of fibers to occur at accessible values of the applied electrical potential.

The only mechanism for cooling the jet in flight that is available in a vacuum is radiation. Molten jets in a vacuum system at room temperature solidify more slowly than jets of polymer solutions or of molten polymers electrospun in air. The formation of jets from molten polymer follows the formation of a Taylor cone. The electrically driven instability, buckling of a jet as it impinges on a stationary surface, conglutination of segments that come into contact, and branching were all observed. In a laboratory vacuum, the jet is often molten when it is collected, because of the limited flight distance. Electrospinning of polymer fibers in interplanetary space may become an important tool for constructing very large, low mass structures and enclosures.

Fig. 52 shows segments of polyethylene terephthalate fibers electrospun in a vacuum. The diameters of the segments ranged from 2 to 6  $\mu\text{m}$ . The fibers were smooth, without beads or sudden changes in diameter. Cross-sectional shapes were

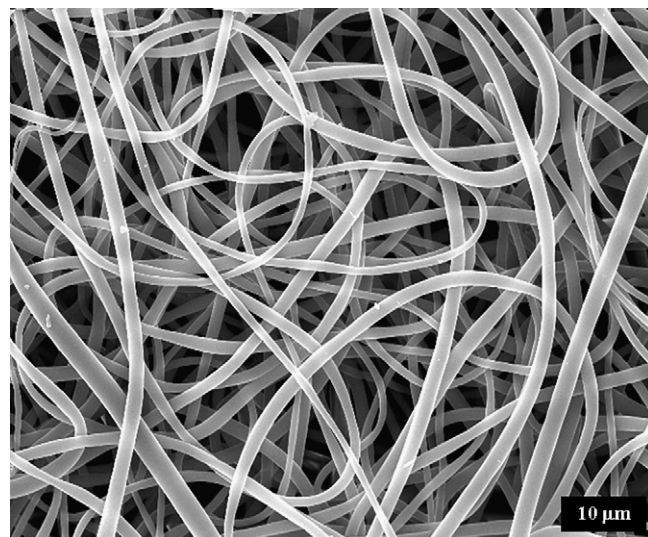


Fig. 52. A scanning electron microscope image of a non-woven sheet of fibers electrospun from molten polyethylene terephthalate in a vacuum. The fiber diameter varied from about 2 to 6  $\mu\text{m}$ . The absence, at crossing points, of morphological changes associated with conglutination indicates that at least the surfaces of these jet segments were nearly solid when collected.

circular. Many tiny branches, with lengths of around 1  $\mu\text{m}$  were present on both fibers shown in Fig. 53. The irregular loops in both fibers have perimeters around 100  $\mu\text{m}$  with patterns characteristic of buckling as a molten jet was collected. The sinuous shape in the left part of Fig. 53 with a wavelength near 5  $\mu\text{m}$  is unusual, but the uniform and short period suggests that it also was caused by buckling during collection.

Fig. 54 shows small jets that emerged slowly from an electrically charged viscous polyimide melt in a vacuum. The experimental polyimide had a molecular weight of 5000 g/mol. A series of small radial branches formed near the tips of these jets.

Polycaprolactone was electrospun from a polymer melt in air with relative ease. The straight segments were often several centimeters long, and moved slowly so stop-motion images were obtained easily. The onset of the electrically driven instabilities in the straight segment in flight was followed.

Fig. 55 shows a jet of molten polycaprolactone in air. A coil created by the bending instability, shown in the square box, grew as it moved downward through the field of view. A new bending instability, shown first in the second row, in the ellipse, then developed. The jet segment in the ellipse, the segment in the box, and the straight segment between experienced different elongations as a function of time and position. The variability in the onset of an electrical bending instability is a source for the variation in diameter that is commonly observed along nanofibers. Jets of molten polycaprolactone also displayed orderly buckling coils as the molten straight segment was stopped on a collector.

#### 7.5. Electrospinning of liquid crystals

Birefringent nanofibers of poly(*p*-phenylene terephthalamide), electrospun from a liquid crystalline solution in

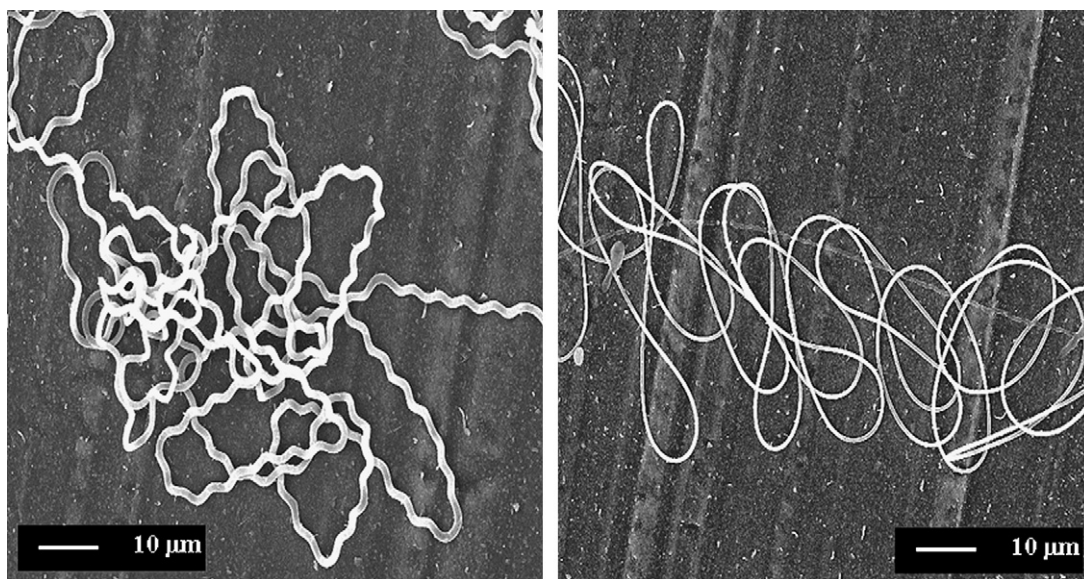


Fig. 53. Polyethylene naphthalate fibers electrospun from the melt in a vacuum. Both fibers have diameters near 1000 nm.

sulfuric acid and coagulated in water, were examined with electron diffraction, as-coagulated and after annealing at 400 °C for 15 min. Diffuse, equatorial, electron diffraction spots from the as-coagulated nanofibers indicated that the chains maintained their parallel alignment along the axis of the nanofiber during coagulation. The annealing treatment improved the local crystallographic packing so that the electron diffraction patterns from the electrospun nanofibers were similar to X-ray diffraction patterns from commercial fibers of poly(*p*-phenylene terephthalamide) [24].

#### 7.6. Electrically conducting polyaniline nanofibers

Fig. 56 shows a scanning tunneling microscope image of nanofibers of polyaniline that were electrospun from a solution in sulfuric acid [24]. The jet of solution was collected in water to coagulate the polyaniline and to wash out the sulfuric acid. Height measurements indicated that the nanofibers had diameters ranging from less than 1 to about 2 μm.

It was evident from both the scanning tunneling microscopy and from resistivity measurements made on tufts of the

fibers that the polyaniline was an electrical conductor. Polyaniline nanofibers, electrospun from sulfuric acid and coagulated in water, were only weakly birefringent. Electron diffraction patterns, from a collection of fibers lying on a flat surface, were not observed from as-spun fibers. Annealing at 150 °C for 15 min did not enhance the birefringence but did result in the appearance of ring of sharp electron diffraction spots along with a weaker ring at a larger angle. The sharpness of the spots in the rings suggested that the local order of the molecules increased during the annealing treatment, as was described in Section 6.2 for nanofibers of poly(*meta*-phenylene isophthalamide). MacDiarmid, in his Nobel Lecture, presented related work on nanofibers of electrically conducting polyaniline [63].

#### 7.7. Nanofibers of spider and caterpillar silk

Spider and caterpillar silk were electrospun into nanofibers [64], and characterized by electron microscopy. The diameter of the silk nanofibers ranged from about 6.5 to 300 nm, making them several orders of magnitudes smaller than the silk fibers

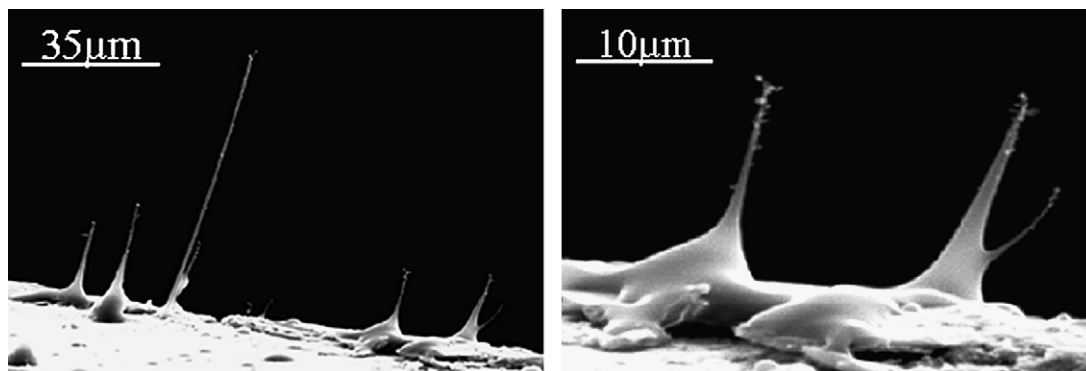


Fig. 54. Electrospun fibers that grew from molten polyimide in a vacuum in a temperature range of 300–350 °C, at a potential difference of 60 kV across a 6 cm gap. The image on the right is an enlargement of the jets also shown at the left, which shows the tiny branches that grew most frequently near the tip. Occasionally a larger branch grew from the region near the base, as seen at the right.

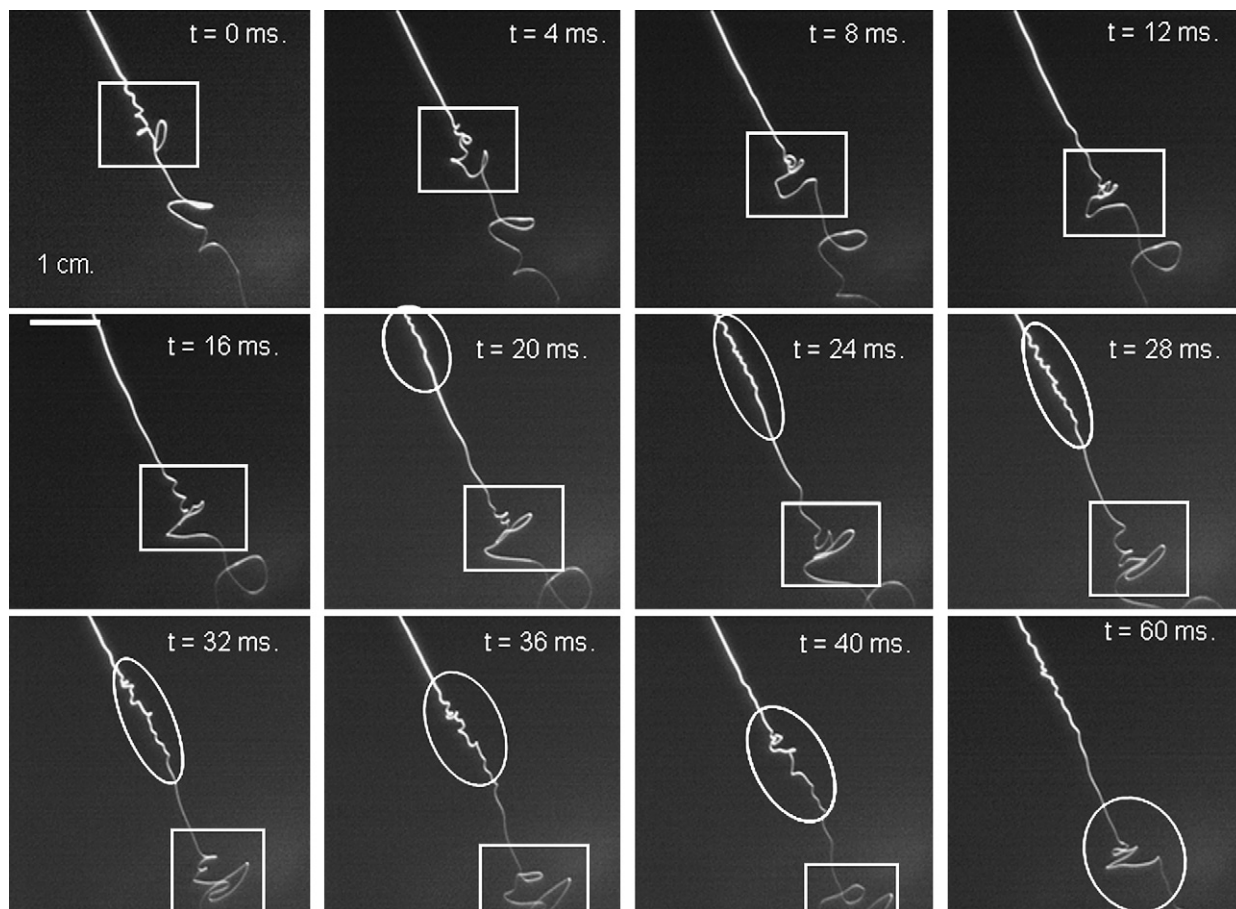


Fig. 55. Evolution, growth and downstream motion of a short segment of a jet of molten polycaprolactone that contained an electrical bending instability preceded and followed by other bending instabilities. The last frame, 20 ms later, shows a well developed expanding coil produced by the electrical bending instability followed by a straight segment which is followed by a developing bending instability that grew from a small bend visible above the ellipse in the 40 ms frame. This sequence was observed to repeat many times.

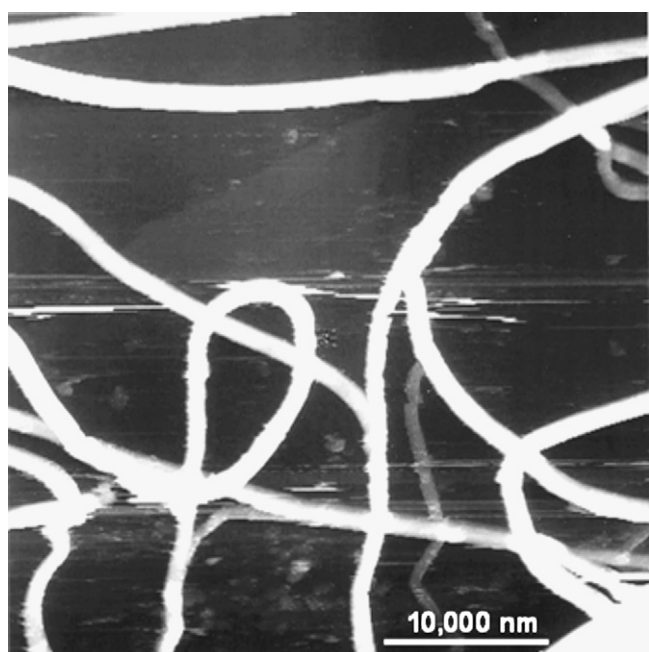


Fig. 56. Electrically conducting polyaniline nanofibers.

spun by silkworms or by many kinds of spiders. Electron diffraction patterns of annealed electrospun nanofibers exhibited diffraction peaks with the molecules aligned along the axis of the fiber. The crystalline order was comparable to that of naturally spun silks [65]. Aqueous solutions, containing three polymers, caterpillar silk taken from the silk gland of a caterpillar, polyethylene oxide, and green fluorescent protein, were electrospun into nanofibers. No large scale segregation of the polymers into separate phases was observed, probably because the large surface area to volume ratio of the fibers allowed rapid evaporation of the water and quickly reduced the mobility of the polymer molecules as the jet solidified.

#### 7.8. Ceramic nanofibers

Thermally stable nanofibers with good mechanical properties and chemical stability were made from ceramics. Some metal organic compounds form linear polymers, or networks with a very low concentration of crosslinks. Others can be dissolved or dispersed in the same solution as a spinnable hydrocarbon polymer. Nanofibers can be electrospun from many such substances. Pyrolysis in air converts the metal organic fibers to a metal oxide, while retaining the nanofiber structure.

Such ceramic nanofibers can function as high performance filters in high temperature gases or liquids, and as supports for catalysts in high temperature reactions.

Ceramic nanofibers are candidates for use in energy conversion devices. An example is the conversion of abundant low temperature waste heat into electrical energy in a thermophotovoltaic system [66,67]. Erbium was added to a solution containing tetra-isopropyl titanate and polyvinylpyrrolidone. Nanofibers were made and pyrolyzed. A mat of nanofibers that contained erbium ions was created. The nanofibers were heated with a hot gas and emitted photons in a narrow band of wavelengths. GaSb photodiodes efficiently converted these photons to electrical power. The source of the thermal energy can range from industrial waste streams and automotive exhaust gases to concentrated sunlight or radioisotope sources. The thermophotovoltaic conversion device had no moving parts and low mass. Ceramic nanofibers may lead to significant advances in thermophotovoltaic energy conversion by utilizing ubiquitous streams of waste heat at temperatures 1000 °C or higher.

### 7.9. Exfoliated clay sheets in nanofibers

Exfoliated sheets of montmorillonite clay with lateral dimensions up to 3  $\mu\text{m}$  were dispersed in a solution of polystyrene in tetrahydrofuran and electrospun into nanofibers with diameters less than 1000 nm. Most of the polystyrene matrixes were removed by using a plasma discharge in air at low pressure to gasify the polystyrene. Gasification of the polymer matrix provides an alternative to slicing the composite with a microtome to observe the dispersion and morphology of the particles of exfoliated clay, see Figs. 57 and 58. The surface tension of the polymer solution crumpled the large

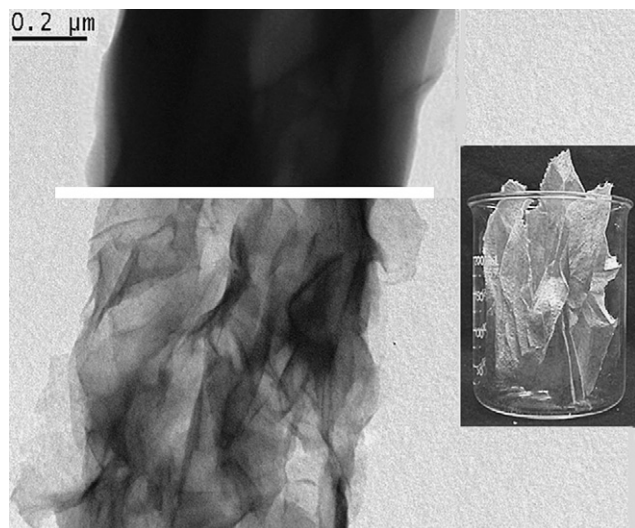


Fig. 57. Transmission electron microscopy of clay sheets crumpled in electrospun polystyrene fibers which had a diameter smaller than the width of the exfoliated clay sheets. The top left shows an as-spun fiber, which is nearly opaque, and the bottom left shows a similar fiber after the removal of most of the polystyrene by plasma etching. The inset at the right part of the figure shows a model, of clay sheets inside a fiber, that was made by crumpling a sheet of paper around a vertical axis.

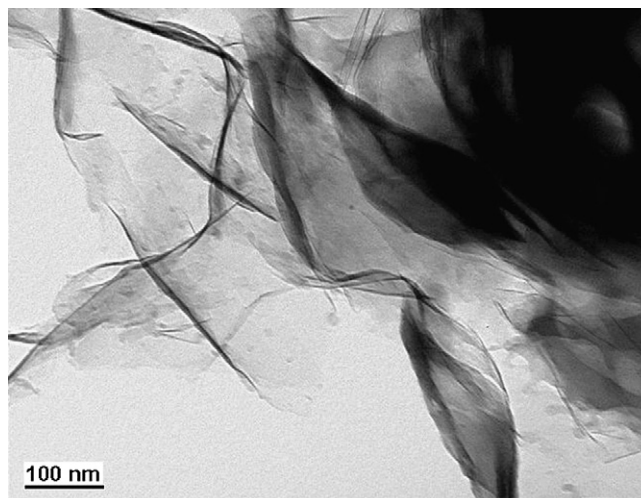


Fig. 58. Plasma etching at a slow rate leaves some clay sheets attached to the surface of a fiber after the removal of most of the surrounding polyimide. The size, shape, and flexibility of clay sheets were revealed. Electron diffraction patterns of the clay were obtained from such exposed sheets.

exfoliated clay sheets in the radial direction, but the sheets were less crumpled in the axial direction. This indicates that the relatively large clay sheets can be expected to provide improvements in the tensile properties of the nanofibers.

The topographical images of the clay sheets remaining after plasma etching not only show the dispersion of inorganic fillers but can also provide stereographic images and diffraction patterns of individual filler particles.

Electrospun nanofibers were used as the support for exfoliated sheets of clay minerals such as montmorillonite and  $\text{Li}^+$ -fluorohectorite [68]. A suspension of exfoliated clay sheets was filtered through a thin layer of electrospun nanofibers. An impervious layer on the fiber network formed because the clay sheets had transverse dimensions larger than the diameter of the interstices between the nanofibers.

## 8. Summary

This paper describes the generation of an electrically charged jet of polymer solution, and some characteristic features that determine the path of the jet, as it becomes very long, solidifies, and is collected in the form of a polymer fiber with a diameter that can often be conveniently stated in nanometers. Many features of the path are understood and predictable. The length is indefinite, typically many kilometers, beginning when the jet first appears and ending only when the jet is stopped.

The jet is subject to a number of electrically driven bending instabilities which cause the path to become a series of coiled coils. The perimeter of each successive turn of an individual electrically driven bending coil is significantly larger than that of the following turn, as long as the jet carries excess charge and remains fluid. The electrically driven bending instabilities may start and stop at different locations along the jet path.

The capillary instability that produces beads, and the development of branches, also occur under appropriate conditions. Conglutination at points of contact of a segment of the jet with other segments may generate elongated three-dimensional networks called garlands.

Mechanical winders can often produce multilayer sheets of nearly parallel nanofibers, by catching and stretching the electrical bending coils. The crossovers and folds necessarily created by such a process reduce the average orientation only slightly and therefore can often be tolerated. The possibilities for complete straightening of the coils mechanically are limited since the rate of elongation of the electrospinning jet [26], in many cases, requires a winder with a very high surface velocity.

The jet may be collected at various points before or after solidification is complete. Buckling often occurs when a fluid jet is stopped by the collector. Buckling may produce a series of short straight segments connected by folds, circular coils, zigzags, and other more complicated shapes. The coils created by buckling are regular, with small, slowly varying diameters. Each new turn of a buckling coil in a fluid jet is added in a few microseconds.

Fluid jets of many polymer solutions solidify homogeneously into smooth fibers with circular cross-sections. Others form a skin that creates a rough surface or collapses to form a ribbon.

A number of photographic and laser-aided methods have been developed to observe and measure the path of the jet, and the diameter of a segment at particular locations. The velocity can be determined at the same point as the diameter by a combination of laser Doppler scattering and measurements of interference of a monochromatic laser beam. The information produced is useful for process monitoring and control. Achieving an appropriate level of control of the various phenomena described in this paper will provide the information needed for design and construction of useful structures, devices, and materials that utilize nanofibers.

The thin fibers that are produced have a high surface area per unit mass. Many nanofibers are transparent in ordinary electron microscopes, so detailed study of crystallization behavior and phase separation morphology are possible. Polymer nanofibers can be coated with metals, carbon, and molecular solids by sputtering, evaporation in a vacuum or chemical deposition. Carbon nanofibers made by pyrolysis of nanofibers of polyacrylonitrile can support the growth of small multiwall carbon nanotube branches by a vapor–liquid–solid growth mechanism to achieve unique, useful nanoscale structures. Polymer nanofibers that contain metal atoms can be oxidized to form ceramic nanofibers. Many kinds of colloidal particles, proteins, DNA, biological organelles, cells and chemical reagents can be sequestered and preserved inside nanofibers.

Usefulness of nanofibers, in areas including filtration, biology, energy conversion, agriculture, scaffolds for artificial organs, hygiene, and clinical medicine, is growing. It is hoped that this description of nanofibers and electrospinning will provide an interesting and useful view of the rapidly developing

area of nanofibers in the field of materials science and technology.

## Acknowledgements

This paper is a summary of the efforts of many people, over a period of 15 years, with support from many sources. Early support from the Edison Polymer Innovation Corporation, Ohio Department of Development, enabled us to begin research on electrospinning of nanofibers. The Ohio Board of Regents provided support at critical times. The National Science Foundation has provided several grants. Current Grants are NSF/NIRT Nanofiber Manufacturing for Energy Conversion # DMI-0403835; University of Nebraska/sub of NSF Modeling-Based Control of Electrospinning Process #25-1110-0038-002; the Ohio State University/sub of NSF Center for Affordable Nanoengineering of Polymer Biomedical Devices #60002999. The United States Army Research Office, and the Soldier Systems Command at Natick provided support through a Multi-University Research Initiative. The Coalescence Filtration Nanomaterials Consortium provided continuing support during the past decade. The members of the Consortium are the Donaldson Company, Ahlstrom Turin, Parker Hannifin Corporation, Hollingsworth and Vose, and Cummins Filtration. A.L.Y. was supported in part by the Israel Science Foundation, the Volkswagen Foundation, and by the U.S. National Science Foundation grant NIRT CBET-0609062.

Daniel J. Smith, Professor of Chemistry, George C. Chase, Professor of Chemical Engineering, Miko Cakmak, Professor of Polymer Engineering, Professor Yuris Dzenis, University of Nebraska, Lincoln, Professors Joachim Wendorff and Andreas Greiner, Phillips-University of Marburg Germany, and Professor Eyal Zussman and Dr. S. N. Resnick, The Israel Institute of Technology, are long time collaborators who have established electrospinning laboratories and made many contributions to the development of electrospinning science and technology. Fig. 44 was made in the laboratory of Professor Peter Lavrentyev in the Department of Biology of The University of Akron. Many other colleagues have collaborated on important electrospinning or nanofiber projects.

The following people have earned their Ph.D. degrees for research that involved electrospinning, and their efforts form the framework of this paper: Jayesh Doshi, Iksoo Chun, Hao Fong, Sureporn Koombhongse Tripatanasuwan, Jong Sang Kim, Gokul Srinivasan, Ratthapol Rangkupan, Xiaoyan Fang, Sphurti Doiphode Bargava, Han Xu, Worophon Kataphinan, Wenxia Liu, Zhaohui Sun, Tao Han, Andre Theron, and Wael Salalha.

Connie Hubbard, a high school science teacher, has introduced many bright high school students to electrospinning, with the help of National Science Foundation “research experiences for teachers” supplemental grants. Jacqui Clark prepared the manuscript. Research Associates, Dale Ertley, Steven Roberts, and Dr. Daniel Galehouse, provided steady help and useful guidance.

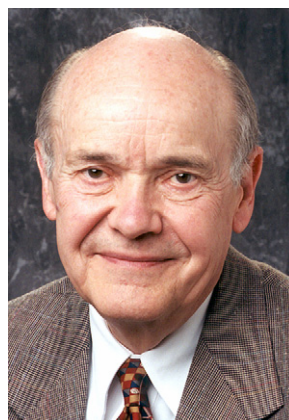
We thank them all, with a special thanks to the many people around the world whose publications and talks have improved

our understanding of electrospinning, as well as to any other contributors, inadvertently not mentioned here.

## References

- [1] Reneker DH, Yarin AL, Zussman E, Xu H. In: Aref H, Van Der Giessen E, editors. *Advances in applied mechanics*, vol. 41. London: Elsevier/Academic Press; 2007. p. 43–195.
- [2] Reneker DH, Fong H, editors. *Polymeric nanofibers*. Washington, DC: American Chemical Society; 2005.
- [3] Reneker DH, Hou H. Electrospinning. In: Bowlin GL, Wnek G, editors. *Encyclopedia of biomaterials and biomedical engineering*, vol. 1. Taylor and Francis Group; 2004. p. 543–50.
- [4] Ramakrishna S, Kazutoshi F, Teo Wee-Eong, Lim Teik-Cheng, Ma Z. An introduction to nanofibers. Singapore: World Scientific Co., 2005.
- [5] Li D, Xia Y. Electrospinning of nanofibers: reinventing the wheel? *Advanced Materials* 2004;16:1151–70.
- [6] Fong H, Reneker DH. Electrospinning and the formation of nanofibers. In: Salem DR, editor. *Structure formation in polymeric fibers*. Munich; Cincinnati, Ohio: Hanser Publishing; 2000. p. 225–46.
- [7] Dai L, Reneker DH. Polymer nanowires and nanofibers. In: Wang ZL, editor. *Nanowires and nanobelts: materials, properties and devices*, vol. 2. Springer Publishing; 2003. p. 269–88.
- [8] Greiner A, Wendorff JH. Electrospinning: a fascinating method for preparation of ultrathin fibers. *Angewandte Chemie International Edition* 2007;46:2–39.
- [9] Frenot A, Chronakis IS. Polymer nanofibers assembled by electrospinning. *Current Opinion in Colloid and Interface Science* 2003;8:64–75.
- [10] Yarin AL, Zussman E, Wendorff JH, Greiner A. Material encapsulation in core–shell micro/nanofibers, polymer and carbon nanotubes and micro/nanochannels. *Journal of Materials Chemistry* 2007;17:2585–99.
- [11] Hille B. *Elementary properties of ions in solution, Ion channels of excitable membranes*. 3rd ed. Sunderland, Mass: Sinauer Associates, Inc.; 2001. p. 309–45.
- [12] Wu H, Zhang R, Liu X, Lin D, Pan W. Electrospinning of Fe, Co, and Ni nanofibers: synthesis, assembly, and magnetic properties. *Chemistry of Materials* 2007;19:3506–11.
- [13] Bogwitzki M, Becker M, Graeser M, Massa W, Wendorff JH, Schaper A, et al. Preparation of sub-micrometer copper fibers via electrospinning. *Advanced Materials* 2006;18:2384–6.
- [14] Sun Z, Zussman E, Yarin AL, Wendorff JH, Greiner A. Compound core/shell polymer nanofibers by co-electrospinning. *Advanced Materials* 2003;15:1929–32.
- [15] Zussman E, Yarin AL, Bazilevsky AV, Avrahami R, Feldman M. Electrospun polyacrylonitrile/poly(methyl methacrylate)-derived carbon micro/nanotubes. *Advanced Materials* 2006;18:348–53.
- [16] Huang PC, Chen S, Lai C, Reneker DH, Qiu H, Yr Y, et al. Electrospun polymer nanofibers with small diameter. *Nanotechnology* 2006;17:1558–63.
- [17] Taylor G. Disintegration of water drops in an electric field. *Proceedings of the Royal Society of London. Series A, Mathematical and Physical Sciences* 1964;280:383–97.
- [18] Taylor G. Electrically driven jets. *Proceedings of the Royal Society of London. Series A, Mathematical and Physical Sciences* 1969;313:453–75.
- [19] Rangkupan R. Electrospinning process of polymer melts. Dissertation. The University of Akron; 2002.
- [20] Spivak AF, Dzenis YA. A condition of the existence of a conductive liquid meniscus in an external electric field. *Journal of Applied Mechanics* 1999;66:1026–8.
- [21] Yarin AL, Koombhongse S, Reneker DH. Taylor cone and jetting from liquid droplets in electrospinning of nanofibers. *Journal of Applied Physics* 2001;90:4836–46.
- [22] Reznik SN, Yarin AL, Theron A, Zussman E. Transient and steady shapes of droplets attached to a surface in a strong electric field. *Journal of Fluid Mechanics* 2004;516:349–77.
- [23] Yarin AL. *Free liquid jets and films: hydrodynamics and rheology*. Harlow, New York: Longman, Wiley; 1993.
- [24] Srinivasan G. Structure and morphology of electrospun polymer fibers. Dissertation. The University of Akron; 1994.
- [25] Baumgarten PK. Electrostatic spinning of acrylic microfibers. *Journal of Colloid and Interface Science* 1971;36:71–9.
- [26] Reneker DH, Yarin AL, Fong H, Koombhongse S. Bending instability of electrically charged jets of polymer solutions in electrospinning. *Journal of Applied Physics* 2000;87:4531–47.
- [27] Yarin AL, Koombhongse S, Reneker DH. Bending instability in electrospinning of nanofibers. *Journal of Applied Physics* 2001;89:3018–26.
- [28] Thompson CJ, Chase GG, Yarin AL, Reneker DH. Effects of parameters on nanofiber diameter determined from electrospinning model. *Polymer* 2007;48:6913–22.
- [29] Tripatanasuwana S, Zhong Z, Reneker DH. Effect of evaporation and solidification of the charged jet in electrospinning of poly(ethylene oxide) aqueous solution. *Polymer* 2007;48:5742–6.
- [30] Yarin AL, Kataphinan W, Reneker DH. Branching in electrospinning nanofibers. *Journal of Applied Physics* 2005;98:064501.
- [31] Liu W. Structure, morphology and applications of high performance electrospun nanofibers. Dissertation. The University of Akron; 2002.
- [32] Guenther AS, Koombhongse S, Liu W, Reneker DH, Kyu T. Dynamics of hollow nanofiber formation during solidification subjected to solvent evaporation. *Macromolecular Theory and Simulations* 2005;15:87–93.
- [33] Huebner AL, Chu HN. Instability and breakup of charged liquid jets. *Journal of Fluid Mechanics* 1971;49:361–72.
- [34] Fong H, Chun I, Reneker DH. Beaded nanofibers formed during electrospinning. *Polymer* 1999;40:4585–92.
- [35] Liu K, Ertley C, Reneker DH. Characterization of an electrospinning jet from videographic observations of glints. *Bulletin of the American Physical Society, March Meeting*, 2008.
- [36] Doshi J, Reneker DH. Electrospinning process and applications of electrospun fibers. *Journal of Electrostatics* 1995;35:151–60.
- [37] Doshi J, Srinivasan G, Reneker DH. A novel electrospinning process. *Polymer News* 1995;20:206–7.
- [38] Han T, Yarin AL, Reneker DH. Viscoelastic electrospinning jets: initial stresses and elongational rheometry. *Polymer* 2008;49:1651–8.
- [39] Boys CV. *Soap bubbles: their colors and the forces which mold them*. Dover; 1959.
- [40] Xu H. Formation and characterization of polymer jets in electrospinning. Dissertation. The University of Akron; 2003.
- [41] Xu H, Reneker DH. Characterization of electrospinning jets using interference color technique. In: Reneker DH, Fong H, editors. *Polymeric nanofibers*. Washington DC: American Chemical Society; 2005. p. 23–35.
- [42] Kim JS, Reneker DH. Polybenzimidazole nanofibers produced by electrospinning. *Polymer Engineering and Science* 1999;39:849–54.
- [43] Theron A, Zussman E, Yarin AL. Electrostatic field-assisted alignment of electrospun nanofibers. *Nanotechnology* 2001;12:384–90.
- [44] Zussman E, Theron A, Yarin AL. Formation of nanofiber crossbars in electrospinning. *Applied Physics Letters* 2003;82:973–5.
- [45] Reneker DH, Kataphinan W, Theron A, Zussman E, Yarin AL. Nanofiber garlands of polycaprolactone by electrospinning. *Polymer* 2002;43:6785–94.
- [46] Koombhongse S, Liu W, Reneker DH. Flat polymer ribbons and other shapes by electrospinning. *Journal of Polymer Science, Part B: Polymer Physics* 2001;39:2598–606.
- [47] Yarin AL, Tchavdarov BM. Onset of folding in plane liquid films. *Journal of Fluid Mechanics* 1996;307:85–99.
- [48] Cruikshank JO, Munson BR. Viscous fluid buckling of plane and axisymmetric jets. *Journal of Fluid Mechanics* 1981;113:221–39.
- [49] Rangkupan R, Reneker DH. Electrospinning process of molten polypropylene in vacuum. *Journal of the Metals, Materials and Minerals* 2003;12:81–7.

- [50] Han T, Reneker DH, Yarin AL. Buckling of jets in electrospinning. *Polymer* 2007;48:6064–79.
- [51] Liu W, Wu Z, Reneker DH. Structure and morphology of poly(metaphenylene isophthalamide) nanofibers produced by electrospinning. *Polymer Preprints* 2000;41:1193–4.
- [52] Hansen LM, Smith DJ, Reneker DH, Kataphinan W. Water absorption and mechanical properties of electrospun structured hydrogels. *Journal of Applied Polymer Science* 2005;95:427–34.
- [53] Smith DJ, Kataphinan W, Reneker DH. Preservation of biological materials using fiber-forming techniques. United States Patent No. US 6,821,479; 2004.
- [54] Greiner A, Wendorff JH, Yarin AL, Zussman E. Biohybrid nanosystems with polymer nanofibers and nanotubes. *Applied Microbiology and Biotechnology* 2006;71:387–93.
- [55] Dror Y, Salalha W, Avrahami R, Zussman E, Yarin AL, Dersch R, et al. One-step production of polymeric micro-tubes via co-electrospinning. *Small* 2007;3:1064–73.
- [56] Fong H, Reneker DH. Elastomeric nanofibers of styrene–butadiene–styrene triblock copolymer. *Journal of Polymer Science, Part B: Polymer Physics* 2000;37:3488–93.
- [57] Liu W, Graham M, Evans EA, Reneker DH. Poly(meta-phenylene isophthalamide) nanofibers; coating and post processing. *Journal of Materials Research* 2002;17:3206–12.
- [58] Hou H, Jun Z, Reuning A, Schaper A, Wendorff JH, Greiner A. Poly-(*p*-xylylene) nanotubes by coating and removal of ultrathin polymer template fibers. *Macromolecules* 2002;35:2429–31.
- [59] Hou H, Reneker DH. Carbon nanotube on carbon nanofiber: a novel structure based on electrospun polymer nanofibers. *Advanced Materials* 2004;16:69–73.
- [60] Sun Z. Design and Engineering of Submicron Structures by Electrospinning. Dissertation. The University of Akron; 2005.
- [61] Ge JJ, Hou H, Graham M, Greiner A, Reneker DH, Harris F, et al. Assembly of well-aligned multiwalled carbon nanotubes in confined polyacrylonitrile environments: electrospun composite nanofiber sheets. *Journal of the American Chemical Society* 2004;126:15754–61.
- [62] Reneker DH, Chun I. Nanometer diameter fibers of polymer produced by electrospinning. *Nanotechnology* 1996;7:216–23.
- [63] MacDiarmid AG. Synthetic metals: a novel role for organic polymers. Nobel Foundation, Aula Magna, Stockholm University; December 8, 2000.
- [64] Zarkoob S, Eby RK, Reneker DH, Hudson SD, Ertley D, Adams WW. Structure and morphology of electrospun silk nanofibers. *Polymer* 2004;45:3973–7.
- [65] Puttanarat S, Eby RK, Kataphinan W, Jones S, Naik R, Reneker DH, et al. Electrospun bombyx mori gland silk. *Polymer* 2006;47:5630–2.
- [66] Teye-Mensah R, Tomer V, Kataphinan W, Tokash JC, Stojilovic N, Chase GG, et al. Erbia modified electrospun titania nanofibers for selective infrared emitters. *Journal of Physics: Condensed Matter* 2004;16:7557–64.
- [67] Tomer V, Teye-Mensah R, Tokash JC, Stojilovic N, Kataphinan W, Evans EA, et al. Selective emitters for thermophotovoltaics: erbia-modified electrospun titania nanofibers. *Solar Energy Materials and Solar Cells* 2005;85:477–88.
- [68] Sun Z, Reneker DH. Thin, flexible and impermeable films made using clay sheets and clay reinforced polymer nanofibers. *Polymer Preprints* 2003;44:166–7.



**Professor Darrell H. Reneker** grew up in Iowa, U.S.A. He holds a Bachelor of Science in Electrical Engineering from Iowa State University and a Ph.D. in solid state physics from the University of Chicago. He began working on electron microscopy of polymers at the DuPont Company in 1959. He is known for the description of the dispiration, a crystallographic defect in the helical symmetry of polymer crystals, and a family of defects that can transport and rotate a long polymer molecule inside a crystal. He was manager of the Center for Materials Science, one of the four major organizational units of the National Institute of Standards and Technology (NIST). He served as Executive

Secretary of the Committee on Materials of the White House Science Office.

Reneker became Professor of Polymer Science and Director of the Institute of Polymer Science of the University of Akron in 1989. He established the first scanning probe microscopy laboratory devoted to the examination of polymer morphology in 1989. Reneker teaches courses on electron microscopy of polymers and electronic properties of polymers. He served on the Board of Directors of the Edison Polymer Innovation Corporation, an Ohio state agency aimed at research and technology transfer. In 1990, he established a laboratory for observing and optimizing the electrospinning process for making polymer nanofibers. His publications re-invigorated work in this field, which, in 2006, produced over 600 publications from laboratories around the world. The productive collaboration between Reneker and Yarin described in this paper began in 1999.



**Dr. Alexander L. Yarin** was the Eduard Pestel Professor of Mechanical Engineering at the Technion – Israel Institute of Technology in 1990–2005. From 2005 he is a Professor of Mechanical Engineering at the University of Illinois at Chicago. He graduated as an applied physicist from St. Petersburg State Polytechnic University in 1977, and has a Ph.D. (1980) and habilitation (1989) in physics and mathematics from the Institute for Problems in Mechanics of the USSR Academy of Sciences in Moscow. His research interests are in hydrodynamics of flows with free surfaces (jets, threads, fibers, films and droplets), rheology and hydrodynamics of non-Newtonian (e.g. polymeric) liquids,

combustion and nanotechnology. Currently his research activities include electrospinning of polymer nanofibers and their applications, suspensions of nanoparticles and coating of nanoparticles in low-pressure plasma. He is a recipient of several awards and fellowships, an author of two research monographs, several review articles, more than 170 technical papers in leading international journals and four patents. He is a member of the editorial advisory boards of two journals, *Experiments in Fluids* and *Bulletin of the Polish Academy of Sciences*, and one of the Editors of the *Springer Handbook of Experimental Fluid Mechanics*.